

---

# Dual-Comb Spectroscopy of Fundamental Vibrational Transitions

Simon Maximilian Holzner

---



München 2015



---

# Dual-Comb Spectroscopy of Fundamental Vibrational Transitions

Simon Maximilian Holzner

---

Dissertation  
an der Fakultät für Physik  
der Ludwig-Maximilians-Universität  
München

vorgelegt von  
Simon Maximilian Holzner  
aus München

München, den 14.10.2015

Erstgutachter: Prof. Dr.Theodor Hänsch  
Zweitgutachter: Prof. Dr. Reinhard Kienberger  
Tag der mündlichen Prüfung: 25.11.2015

# Contents

<b>Abstract</b>	<b>vii</b>
<b>Zusammenfassung</b>	<b>viii</b>
<b>1 Introduction</b>	<b>1</b>
<b>2 Fundamental technical and physical concepts</b>	<b>5</b>
2.1 The Frequency Comb . . . . .	5
2.1.1 A Single Ultra Short Pulse . . . . .	5
2.1.2 The Optical Frequency Comb . . . . .	6
2.2 Fourier Transform Spectroscopy . . . . .	8
2.2.1 Conventional Fourier Transform Spectroscopy . . . . .	8
2.2.2 Dual-Comb Spectroscopy . . . . .	10
2.2.3 Adaptive Sampling . . . . .	18
<b>3 Linear Mid-Infrared Spectroscopy</b>	<b>25</b>
3.1 Mid-Infrared Optical Parametric Oscillator . . . . .	27
3.1.1 Optical Parametric Oscillator Setup . . . . .	28
3.1.2 Spectral and Temporal Characterization of the Parametric Oscillator	31
3.1.3 Summary Mid-Infrared Optical Parametric Oscillator . . . . .	35
3.2 Mid-Infrared Photonics . . . . .	36
3.2.1 Silicon Mid-Infrared Photonics . . . . .	37
3.2.2 Chalcogenide Glass Mid-Infrared Photonics . . . . .	42
3.2.3 Summary Mid-Infrared Photonics . . . . .	45
3.3 Mid-Infrared Dual-Comb Spectroscopy . . . . .	46
<b>4 Coherent Raman Spectroscopy</b>	<b>55</b>
4.1 Coherent Raman Scattering Theory . . . . .	57
4.2 Coherent Anti Stokes Raman Dual-Comb Spectroscopy . . . . .	63
4.3 Concentration and Power Dependence of Dual-Comb Coherent Anti Stokes Raman Spectroscopy And Heterodyne Detection . . . . .	71
4.4 Differential Coherent Raman Spectroscopy . . . . .	77
4.5 Asymmetric Coherent Anti Stokes Raman . . . . .	82

4.6 Coherent anti Stokes Raman Imaging . . . . .	89
<b>5 Conclusion</b>	<b>93</b>
<b>6 Outlook</b>	<b>95</b>
<b>7 Appendix</b>	<b>97</b>

# Abstract

Spectroscopy of fundamental vibrational transitions offers a label-free alternative for high-chemical contrast measurements. These transitions can be interrogated either directly by using mid-infrared light or indirectly through Raman scattering. This thesis aims to advance dual-comb spectroscopy to improve the acquisition speed, resolution and spectral coverage of vibrational spectroscopy. Dual-comb spectroscopy is a time domain technique, which combines optical frequency combs -coherent light sources with a spectrum constituted of discrete evenly spaced lines - and Fourier transform spectroscopy.

For linear spectroscopy, a mid-infrared optical parametric oscillator was developed and characterized. Its idler-pulse duration can be as short as a few cycles ( $\sim 3$  to  $6$  cycles), with a central wavelength tunable from  $2180$  nm to  $3732$  nm ( $2679$   $\text{cm}^{-1}$  -  $4587$   $\text{cm}^{-1}$ ), allowing more than  $2500$  nm ( $2861$   $\text{cm}^{-1}$ ) of total coverage while maintaining an average power of tens of milliwatts. The high peak power of this system was exploited for spectral broadening; generation of phase-coherent supercontinua was achieved in waveguides, made from either silicon or chalcogenide glass, producing octave spanning spectra  $\sim 1500$  nm to  $3300$  nm ( $3030$   $\text{cm}^{-1}$  -  $6666$   $\text{cm}^{-1}$ ) for silicon and from  $\sim 1600$  nm beyond  $3860$  nm ( $2590$   $\text{cm}^{-1}$  -  $6250$   $\text{cm}^{-1}$ ) for chalcogenide glass). Two optical parametric oscillator were constructed, advancing toward a dual-comb mid-infrared spectrometer. Since the optical parametric oscillators are not stabilized, an additional correction scheme was set up and characterized.

Coherent Raman scattering was also investigated, as a means to access optically active and inactive fundamental vibrational transitions. Several spectroscopy setups were developed to measure the Raman blue or red shifted light in forward and backward scattered direction as well as a differential detection between blue and red shifted light. There is a dead time between consecutive interferograms existent, up to a factor of  $1000$  larger than the measurement time. This dead time could be reduced by an order of magnitude using a laser with  $\sim 1$  GHz and a laser with  $100$  MHz repetition rate instead of two lasers with  $\sim 100$  MHz repetition rate. All implementations achieved excellent acquisition times (in the microsecond range), signal-to-noise ratios up to  $1000$  and spectral coverage of about  $\sim 1200$   $\text{cm}^{-1}$ ). These advantages enabled measuring spectrally resolved images, in a first rudimentary microscopy-setup.



# Zusammenfassung

Spektroskopie fundamentaler Schwingungsübergänge erlaubt einen markierungsfreien Zugang zu Messungen mit hohem chemischen Kontrast. Diese Übergänge sind entweder direkt über lineare mittlere Infrarot Spektroskopie oder indirekt durch Raman Streuung zugänglich. Der dieser Arbeit zugrundeliegende Gedanke war Zwei-Kamm-Spektroskopie weiter zu entwickeln um Schwingungsspektroskopie in Hinsicht auf Messzeit, spektraler Bandbreite und Auflösung von zu verbessern. Zwei-Kamm-Spektroskopie ist eine Technik die optische Frequenzkämme - kohärente Lichtquellen mit einem Spektrum aus Linien exakt gleichen Abstands - und Fourier Transformations Spektroskopie vereint.

Zur linearen Spektroskopie fundamentaler Schwingungsübergänge wurde ein optisch parametrischer Oszillator entwickelt und charakterisiert. Idealerweise beträgt die Idler-Pulsdauer nur einige Feld Zyklen (3 - 6 Zyklen). Die Zentralwellenlänge ist von 2180 nm bis 3732 nm ( $2679 \text{ cm}^{-1}$  -  $4587 \text{ cm}^{-1}$ ) durchstimmbare, sodass sich eine Gesamtabdeckung von etwa 2500 nm ( $2861 \text{ cm}^{-1}$ ) bei einer Durchschnittsleistung im zweistelligen Milliwatt Bereich ergibt. Die hohe Spitzenintensität dieses Systems wurde zur spektralen Verbreiterung genutzt. Mit Hilfe zweier verschiedener Wellenleitern konnte ein jeweils oktavenumspannendes, phasen-kohärentes Superkontinuum erzeugt werden, das im Falle des Siliziumwellenleiters einen Bereich von  $\sim 1500 \text{ nm}$  bis  $3300 \text{ nm}$  ( $3030 \text{ cm}^{-1}$  -  $6666 \text{ cm}^{-1}$ ) abdeckt und von etwa  $1600 \text{ nm}$  bis  $3860 \text{ nm}$  ( $2590 \text{ cm}^{-1}$  -  $6250 \text{ cm}^{-1}$ ) für den Chalkogenidglaswellenleiter. Es wurden zwei identische Oszillatoren aufgebaut und ein erster Versuch unternommen, sie in einem Zwei-Kamm-Experiment zu nutzen. Diese Oszillatoren wurden nicht stabilisiert, was die Entwicklung und Charakterisierung eines zusätzlichen Korrektursystems erforderlich machte.

Kohärente Raman-Streuung wurde als weiterer Zugang zu fundamentalen Schwingungsübergängen untersucht. Mehrere Spektroskopie Aufbauten wurden entwickelt, um blau oder rot verschobenes Raman-Licht in vorwärts- und rückwärtsgestreuter Richtung zu messen, sowie eine differentielle Messung zwischen blau und rot verschoben Licht. Zwischen aufeinanderfolgenden Interferogrammen ist eine Totzeit vorhanden, die bis zu einem Faktor 1000 größer sein kann als die Messzeit. In einen Aufbau der einem Laser mit  $\sim 1 \text{ GHz}$  und  $100 \text{ MHz}$  Repetitionsrate anstatt der üblichen zwei Laser mit  $\sim 100 \text{ MHz}$  Repetitionsrate verwendet, konnte diese Totzeit um eine Größenordnung verringert werden. All diese Implementierungen konnten ausgezeichnete Messzeiten (im Mikrosekundenbereich), ein Signal-Rausch Verhältnis von bis zu 1000 und eine spektrale Abdeckung von etwa  $1200 \text{ cm}^{-1}$  erzielen. Damit waren die Voraussetzung erfüllt, spektral aufgelöste Bilder in einem rudiemären Mikroskopieaufbau zu messen.



# Chapter 1

## Introduction

The invention of the laser in the 1960s ([1, 2, 3]) ushered in a new era in natural sciences. It was a previously unimaginable brilliant light source, which allowed investigating and harnessing effects formerly hard to access because of their low cross sections as Raman scattering [4, 5] or impossible to investigate as the nonlinear behaviour of matter under the incident of extremely intense light. Due to its favourable attributes, as e.g. high intensity and a collimated beam, the laser was subjected to rapid development, making it from a lab curiosity to one of the most widespread tools in science and engineering. Shortly after the invention of the laser, it was realized, that the emitted light constitutes an extremely strong electromagnetic field - strong enough to push the response of a material beyond linear into the nonlinear to extreme nonlinear regime. With a field strength of  $10^7$  V/m the early pulsed ruby lasers are relatively weak for today's standards. Nevertheless they enabled the measurement of the nonlinear response from a quartz crystal, generating the second harmonic of the incident radiation [?]. Similarly to the laser technology itself, the nonlinear light-matter interaction was subject to intense investigation. The advent of mode-locked lasers finally made nonlinear optics an integral part of a vast number of devices and techniques. The high peak intensities allow nonlinear frequency conversion and extreme spectral broadening to be achieved routinely. The generated spectra can surpass any gain material in spectral coverage which can be more than an octave and frequencies can be generated in a wavelength region where laser materials are hardly available as, for example, the mid-infrared. The combination of mode-locked lasers and nonlinear optics finally led to the invention of the optical frequency comb. Optical frequency combs - light sources with a spectrum constituted of discrete evenly spaced lines - were originally conceived for frequency metrology [6] in order to measure atomic transitions with unprecedented precision. Soon this new light source sprawled into different fields. Optical Frequency combs have evolved into a tool allowing extraordinarily high precision in measurement and control of light, making them valuable to a multitude of applications, as time-keeping, satellite navigation, telecommunication and even astronomy. It may not be surprising

that optical frequency combs also found their way into molecular spectroscopy, where they formed an appealing combination with Fourier transform spectroscopy: dual-comb spectroscopy.

Fourier transform spectroscopy is a technique which originally relies on a mechanical interferometer to convert optical frequencies down to the audio to lower radio frequency region. It allows recording of broadband spectra spanning at virtually any optical frequency a detector can be manufactured. In contrast to a dispersive spectrometer, it uses a single photodetector harnessing its full sensitivity range. When the interferometer is scanned, incident fields are interfering on the detector and an electrical signal is produced whose Fourier transform yields the optical spectrum. The resolution of this classical spectrometer depends on mechanical parts making it very large and hard to operate at high resolution as they have to be moved a large distance with high precision. The movement speed of these mechanical parts finally limits the recording speed of the instrument.

Dual-comb spectroscopy allows overcoming these mechanical limitations. It preserves the benefits of having a single photodetector and the possibility to harness its full sensitivity range but allows improving the recording speed and facilitates high resolution measurements considerably. The dual-comb technique utilizes that optical frequency combs of slightly different mode spacing will generate a heterodyne beat signal when combined on a photodetector. The theoretical recording speed of this technique is only limited by the linewidth of the sample, which can be as high as 120 GHz for a liquid sample and is far beyond the recording speed of state of the art analog to digital converters. A similar statement can be made for the maximal resolution of this technique: the resolution depends solely on the laser parameters as mode spacing and line width, techniques as interleaving allow pushing these limits further to even higher resolution

By combining these advantages with the fact that a frequency comb is a train of (potentially ultra-short) pulses in the time domain, this technique can be extended beyond linear spectroscopy. Nonlinear spectroscopy, for example, allows highly resolved spectra, recorded with sub-Doppler resolution, to be acquired using two photon excitation. Multi-photon transitions allow entering different wavelength regions which can not or only with immense effort be reached by conventional sources, as for example the ultra violet or the mid-infrared.

Especially the mid-infrared remains one of the most attractive spectral region due to the possibility of accessing fundamental vibrational bands [7, 8, 9, 10, 11]. These transitions allow deducing information about molecular structure or composition of arbitrary substance mixtures. The large cross sections of these fundamental transitions concede highly sensitive detection, which is important if the sample under scrutiny is very dilute as e.g. in biological samples. Conventional Fourier transform spectroscopy is the usual choice for mid-infrared spectroscopy as no detector arrays are available in this region and most common sources provide broadband but incoherent light. The low brilliance of the

---

sources in combination with a mechanical interferometer leads to long acquisition times. Dual-comb spectroscopy promises a significant improvement in terms of measurement time and resolution in this spectral region. Yet the spectra taken in this region, using dual-comb spectroscopy, are limited by poor stability of the available light sources or the spectral span offered by these light sources in the mid-infrared.

Raman scattering is a different approach of to access fundamental vibrational bands, it is an inelastic scattering process in which energy is exchanged between the incident light field and the sample under scrutiny. This exchange of energy shifts the frequencies of the incident field by an amount determined by the transition energy structure of the sample. Evaluating the frequency shifted light, reveals the fundamental transitions based on their specific energies. In its coherent form as Coherent anti-Stokes Raman scattering, it is widely associated as a non-invasive tool in chemical sensing and imaging (see e.g. [12, 13, 14, 15]). Coherent Raman scattering spectroscopy can be very fast and images can be sampled at video rates. Such speeds come at the expense of spectral coverage. The recorded images generally map a single Raman transition or very few transitions simultaneously [16]. If the spectral coverage is chosen large, generally, a low recording speed has to be tolerated [17, 18].

This thesis entwines these two fields: mid-infrared spectroscopy and Raman spectroscopy.

Before going in medias res, an introduction to ultra-short pulses, how they constitute a frequency comb, the principals of dual-comb spectroscopy and adaptive sampling is given in Chapter 2. It is supposed to review fundamental concepts underlying all conducted experiments and also to establish a common ground in terms of notations.

In Chapter ?? the development and characterization of a broadband singly resonant optical parametric oscillator, pumped by a commercially available Titanium Sapphire laser source, as a tool, which potentially can provide few cycle ultra-short pulses tunable over a large spectral span, for broadband dual-comb spectroscopy is documented. As the spectral coverage of dual-comb spectroscopy for a given setup is only limited by the detector sensitivity a broader spectral coverage of the used sources provides a measurement time benefit as the source does not need to be scanned. The spectral coverage of the optical parametric oscillator is limited by the gain and phase matching in the gain medium. A different nonlinear effect termed supercontinuum generation can produce an extremely broadband spectrum from a comparably narrow pump source. As a nonlinear effect it is crucially dependent on the incident power and on the interaction length between pump field and nonlinear medium. A waveguide holds promise to ensure both at the same time. In a waveguide light is guided over a long distance and the modal confinement ensures a high intensity. Supercontinuum generation was demonstrated in the course of this thesis in two different kinds of waveguides, made from silicon as well as chalcogenide glass. Under certain circumstances a supercontinuum generated in such waveguides can lose coherence, hence the coherence properties of the generated light were also taken under scrutiny by beat detection experiments with

narrow band CW lasers. Finally, as the light emitted by the optical parametric oscillator as well as the generated supercontinua are both not stabilized to constitute a frequency comb, a first attempt of mid-infrared dual-comb spectroscopy has been made using a special correction scheme termed adaptive sampling.

The experiments presented in Chapter 4 try to combine the two seemingly contradictory parameters speed and spectral coverage in a Raman measurement. The combination of Dual-comb spectroscopy with Raman scattering promises recording speeds similar to a single line Raman measurement while, at the same time, a spectral coverage comparable to the most broadband coherent Raman techniques. Starting from a basic CARS - coherent anti-Stokes Raman spectroscopy - setup, different variants have been developed and tested. Among them are the detection of the red shifted light and the detection of the backward scattered light. The favourable recording parameters as potentially very fast recording speeds and spectral coverage, suggested its use in an imaging setup. Still this technique suffers from a dead time between consecutive measurements which is much larger than the actual measurement time (it can be more than a factor 1000 larger). To reduce this dead time, a new scheme is presented, which uses two laser systems with highly different repetition rates and a heterodyne measurement technique to prevent deterioration of signal quality. The heterodyne measurement implications were analysed in detail. A differential detection scheme was furthermore set up to improve the signal to noise ratio and effectively cancel noise.

# Chapter 2

## Fundamental technical and physical concepts

### 2.1 The Frequency Comb

Being one of the central tools of the experiments conducted in the course of this thesis, light sources generating ultra-short pulses, as the mode-locked laser, should be reviewed here short. A passively mode-locked laser can emit a train of ultra-short pulses, with repetition frequencies in the range from some Megahertz, for long-cavity systems [19], of up to several Gigahertz for systems operating with a very short cavity [20, 21, 22, 23, 24]. The produced pulses can have durations from picoseconds down to only a few femtoseconds (e.g. [25, 26, 27, 28]). This chapter reviews the very basic concepts of ultra-short pulses. It treats a single pulse as well as a train of pulses constituting an optical frequency comb (see appendix for more detailed information). It also reviews the principles of Fourier transform spectroscopy, dual-comb spectroscopy and adaptive sampling.

#### 2.1.1 A Single Ultra Short Pulse

##### Pulse Electric Field

A single pulse, for example from a mode-locked laser, can be described as a pulse envelope  $\sqrt{I(t)}$  with an underlying electric field (e.g. [29]). The pulse envelope  $\sqrt{I(t)}$ , determines the shape of the pulse. The underlying field, oscillating at the carrier frequency  $f_0$ , introduces an important parameter: the carrier envelope phase  $\Delta\varphi$  i.e. the relative position of the field oscillations to the envelope. This common way of describing an ultra short pulse is valid down to pulse durations of only some field cycles and

even then it can be refined to give valid results [30]. Commonly a time dependent phase term  $\varphi(t)$  is added, to account for different phase effects caused ,for example, by the interaction with a medium, a time delay or the above mentioned carrier envelope phase:

$$\tilde{E}(t) = \sqrt{I(t)}\cos(2\pi f_0 t + \varphi(t)) \quad (2.1)$$

As an observable, the electric field  $\tilde{E}(t)$  is always a real quantity but it is often more convenient to write the field as an (complex) analytic signal  $E(t)$ , which is done through out this work. It can be obtained from a measured signal by combining it with its Hilbert transform:

$$E(t) = \tilde{E}(t) + i\mathcal{H}(\tilde{E}(t)) = A(t)e^{i2\pi f_0 t} e^{i\varphi(t)} \quad (2.2)$$

with the complex envelope function  $A(t) \neq \sqrt{I(t)}$ , an exponential containing an oscillating term at  $f_0$  and a phase term  $e^{i\varphi(t)}$ . Loss or gain in a material influences  $A(t)$  and potentially the phase term. A gain and loss-less material does not change  $A(t)$  but the phase term  $e^{i\varphi(t)}$ .

### 2.1.2 The Optical Frequency Comb

At the output of a mode-locked laser a pulse exits the cavity every round trip time, which is called the pulse repetition period  $T_{rep}$ . It is defined by demanding that the pulse (envelope) reproduces itself after the time  $T_{rep}$  i.e.  $\sqrt{I(t + T_{rep})} = \sqrt{I(t)}$ .

This periodicity of pulses appearing at the output of a mode-locked laser can be mathematically expressed, in the time domain, as the convolution of a Shah-distribution  $\text{III}$ , with a spacing of  $T_{rep}$ , and the field of a single pulse  $E(t)$  or, in the Frequency domain, as the multiplication of a Shah-distribution and the Fourier transform of the electric field in the time domain  $\mathcal{F}(E(t)) = E(\omega)$ :

$$\begin{aligned} E(t) \otimes \text{III} &= \sum_{n=-\infty}^{\infty} E(t - nT_{rep}) \\ \mathcal{F}(E(t))\mathcal{F}(\text{III}) &= \frac{2\pi}{T_{rep}} E(2\pi f) \sum_{m=-\infty}^{\infty} \delta\left(2\pi f - \frac{2\pi m}{T_{rep}} - \frac{\Delta\varphi}{2\pi T_{rep}}\right) \end{aligned} \quad (2.3)$$

In Equation 2.3 the two degrees of freedom of an optical frequency comb can be read of, the repetition frequency  $f_{rep} = 1/T_{rep}$  and a shift from zero frequency, the carrier

envelope offset frequency  $f_{ceo} = \Delta\varphi/2\pi T_{rep}$ . The frequency of every comb mode  $f(m)$ , with mode number  $m$ , can then be expressed as the carrier offset frequency  $f_{ceo}$  and a multiple of the repetition frequency  $f_{rep}$ [31, 32]:

$$f(m) = mf_{rep} + f_{ceo} = \frac{m}{T_{rep}} + \frac{\Delta\varphi}{2\pi T_{rep}} \quad (2.4)$$

using this equation allows to express the electric field of an optical frequency comb in the well known frequency comb equation (e.g.[33]):

$$E(t) = \sum_{m=-\infty}^{\infty} A(mf_{rep} + f_{ceo}) e^{i2\pi\varphi(t)} e^{i2\pi(mf_{rep} + f_{ceo})t} = \sum A_m e^{i2\pi\varphi(t)} e^{i2\pi(mf_{rep} + f_{ceo})t} \quad (2.5)$$

thus relating optical frequencies to two accurately measurable radio frequencies  $f_{rep}$  and  $f_{ceo}$ . This ability to link an optical frequency via mixing with the frequency comb to these two radio frequencies allows to determine the optical frequency under scrutiny to a very high precision. This fact made the optical frequency comb to one of the major tools of frequency metrology. On the other hand, controlling  $f_{rep}$  and  $f_{ceo}$  allows to generate light of precisely known frequencies, which made the optical frequency comb a tool used in various other fields beyond metrology - one of them being spectroscopy.

## 2.2 Fourier Transform Spectroscopy

Infrared spectroscopy is one of the most commonly used analytic techniques nowadays. Not only is it applicable to nearly all kinds of samples from liquids to gases to powders or pastes (for example by attenuated total reflection [34, 35]), it also offers good selectivity and high sensitivity. It is based on the interrogation of molecular rotational and vibrational transitions, which are highly specific for a certain functional group inside a molecule. In the early days of infrared spectroscopy, the measurement devices have been based on dispersive spectrometers working as a monochromator. This kind of spectrometers have been too slow for various measurements, there was no possibility to e.g. analyze the eluate from a chromatographic column, time resolved spectroscopy or hyper spectral imaging. A CCD based dispersive spectrometer does not face the problem of scanning but since the frequency bins are generally read out serially, the acquisition of a single spectrum takes considerable time (milliseconds). CMOS detector arrays, which in principle allow a parallel read out, on the other hand face the problem of a lower sensitivity, a part of the active area is covered by an amplifying transistor for every frequency bin. An additional problem is the lack of possibilities to produce CCD or CMOS detectors in various wavelength regions.

The introduction of the Fourier transform technique solved several of these problems at the same time. Offering a couple of advantages over the dispersive spectrometers in various wavelength regions, it became the standard. A Fourier transform spectrometer is not based on dispersive elements to gain a wavelength resolved spectrum but on interference in the time domain yielding the interferogram. All the spectral elements are measured at the same time. The frequency resolved spectrum is gained from the time domain signal by Fourier transform, giving the name to this technique. It is a well know technique which produced impressive results over the last five decades, nevertheless it shall be discussed briefly in the following to recall the principles.

### 2.2.1 Conventional Fourier Transform Spectroscopy

A traditional Fourier transform spectrometer is based on an interferometric system, which allows measuring the auto-correlation of the incident field. A very common interferometer type is the Michelson interferometer (in the form of a Twyman-Green interferometer) but several other interferometers with different setups exist. To illustrate the process in more detail it shall be reviewed on the example of a Mach-Zehnder type interferometer: light, of an arbitrary source, enters the interferometer hits a first beam splitter and is separated into two paths. In one path an inserted stage is generating a relative time delay  $\tau$  between the light fields in the two different pathways of the interferometer. Finally the two paths are combined again in a second beam splitter and the light intensity of the recombined beams is measured on a photodetector as a function

of the relative time delay  $\tau$ .

The detector measures an intensity proportional to the absolute square of the combined electric fields. As the detector bandwidth is much smaller than the optical frequencies, the measured signal  $s(\tau)$  is low pass filtered, i.e. time integrated [29, 36, 37]:

$$s(\tau) \propto \int_{-\infty}^{\infty} dt |E(t + \tau) + E(t)|^2 = \int_{-\infty}^{\infty} dt |E(t)|^2 + |E(t + \tau)|^2 + 2\text{Re} [E^*(t)E(t + \tau)] \quad (2.6)$$

The first two terms on the right side of the equation,  $|E(t)|^2$  and  $|E(t + \tau)|^2$  are proportional to the incident energy of the individual fields and do not change as a function of the relative delay  $\tau$ , in fact, as the integration is carried out they contribute only a dc term. The mixing or interferometric term contains the spectral information encoded as the auto-correlation of the incident field:

$$s(\tau)_{interferometric} \propto \int_{-\infty}^{\infty} dt \text{Re} [E(t)^* E(t + \tau)] \quad (2.7)$$

The spectrum  $I(f)$  can be obtained from the interferometric term  $s(\tau)_{interferometric}$  via Fourier transform, using the cross-correlation theorem:

$$\begin{aligned} I(f) &\propto \mathcal{F}(s(\tau)_{interferometric}) \propto \int_{-\infty}^{\infty} d\tau e^{2\pi i f \tau} s(\tau)_{interferometric} \\ &\propto \mathcal{F}(E^*(-t)) \mathcal{F}(E(t)) = E^*(f) E(f) \end{aligned} \quad (2.8)$$

A problem Fourier transform spectrometers have to face is the dependency of their resolution on the maximal value the time delay  $\tau$  between the interferometer arms can attain. In a real world experiment the delay  $\tau$  can not take values from  $-\infty$  to  $+\infty$  as demanded in the integral (see Formula 2.8). A limitation of  $\tau$  corresponds to a multiplication of the signal  $s(\tau)_{interferometric}$  with a boxcar function. In the Fourier-domain this leads to a convolution with a sinc-function. Its width is proportional to  $1/\tau_{max}$  and sets the instrumental resolution. To gain a high resolution the path difference between the two interferometer arms has to get very large ([38]), for example, a resolution of 100 MHz requires a path difference of  $\sim 1,5$  m.

When carrying out the integral in Equation 2.6, it can be written as:

$$s(\tau) \propto \text{Re} \left( |A(\tau)|^2 e^{i2\pi f \tau} \right) \quad (2.9)$$

The delay  $\tau$  is commonly introduced by a moving stage and can be parametrised as  $\tau = t2v/c$ , with the stage speed  $v$ . Alternatively, a scaled frequency  $\hat{f} = f * 2v/c$  can be

defined, where  $\hat{f}$  is relocated to a different frequency band, much lower in frequency than  $f$ . This down conversion depends on the moving speed of the mechanical stage and usually down converts the optical frequencies into the audio range. Nevertheless, a small down conversion factor  $d = 2v/c$ , defined as the ratio between the original optical frequencies and the down converted frequencies, is desired as mixing to a low frequency means long acquisition times.

The resolution in the optical domain  $\Delta f_{opt}$  is given by the resolution in the down converted frequency domain  $1/T_{acquisition}$  times the inverse of the downconversion factor  $d = 2v/c$ :

$$\Delta f_{opt} = \frac{1}{T_{acquisition}} \frac{1}{d} \Rightarrow T_{acquisition} = \frac{1}{\Delta f_{opt}} \frac{1}{d} \quad (2.10)$$

A large down conversion factor  $d$  hence leads to a longer measurement time for a given optical resolution compared to a smaller down conversion factor. Since the stage in the interferometer can not move arbitrarily fast, the minimal down conversion factor is (most if the time) limited by the maximal speed of the stage used and, in most of all cases, this leads to a downconversion to the audio frequency range.

Summing up above said: Fourier transform spectroscopy has some quite distinct advantages e.g. being a naturally multiplexed measurement combined with a high geometric throughput, giving it an edge over dispersive techniques in a lot of the frequency bands. Nevertheless it also has to face some problems, of which some have been pointed out above and are mainly connected to mechanical components. A mechanical stage is not able to move at arbitrarily high speeds as well as not able to travel an arbitrary long distance, limiting acquisition speed as well as resolution.

### 2.2.2 Dual-Comb Spectroscopy

Realizing that the mechanical part of the interferometer is, most of the time, the bottleneck of this instrument allowed to develop new approaches, trying to improve the traditional technique in aspects of acquisition time and resolution. One of this approaches is the dual-comb technique. Two pulsed lasers, constituting two optical frequency combs, are used in such a setup.

It takes advantage of the fact that the delay stage in a classical interferometer can be replaced by a second laser system as indicated in Figure 2.1. To introduce a varying time delay  $\tau$  between the pulse pairs leaving the two lasers, the repetition rates of the two lasers have a small frequency difference  $\Delta f$ . In this way, the delay between the pulses in the pulse pairs emitted increases from pulse pair to pulse pair linearly by the difference

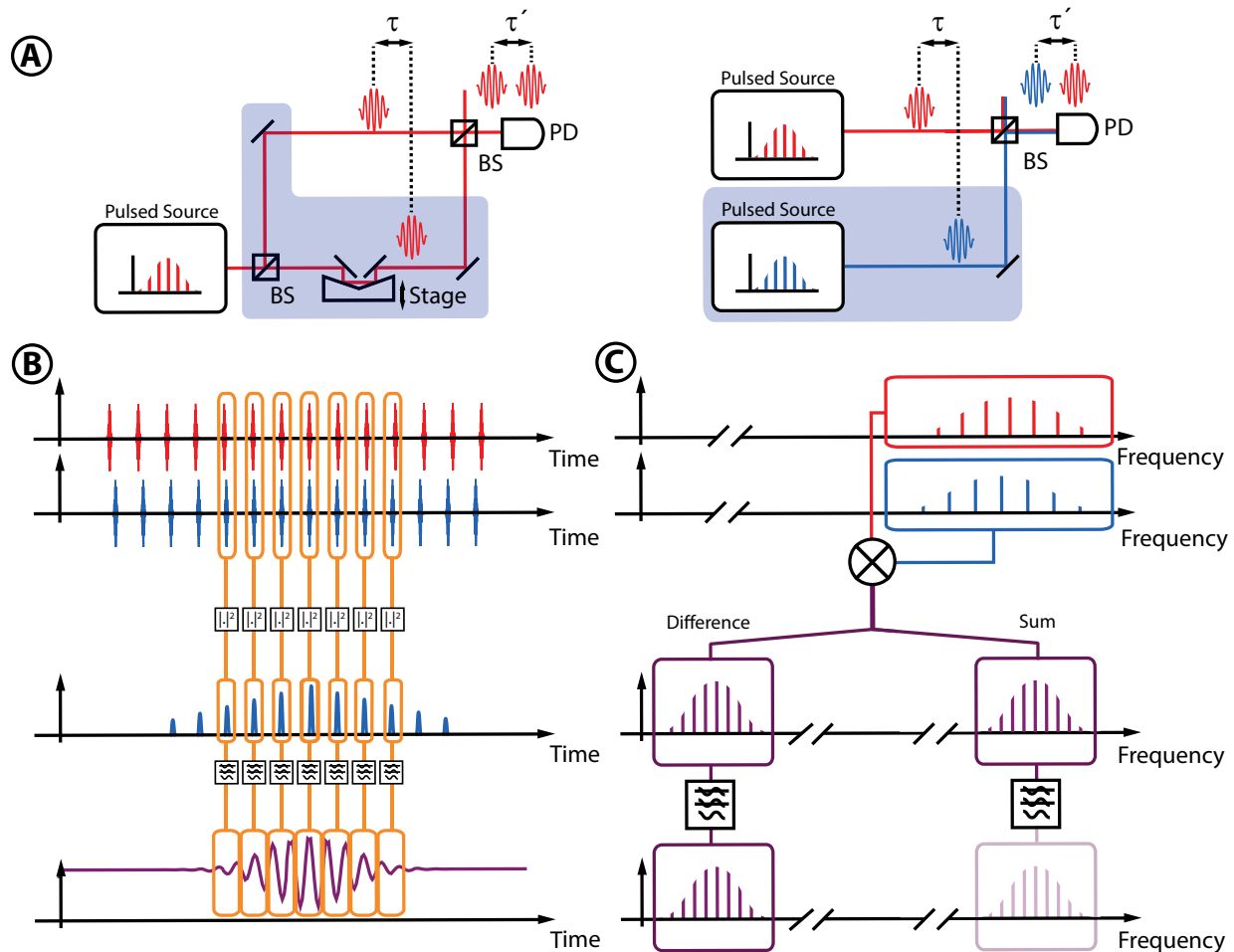


**Figure 2.1:** **A** Mach Zehnder interferometer with a mechanical stage, introducing a varying time delay  $\tau$  between pulse pairs. The mechanical stage can be replaced by a second comb with a slightly different repetition rate. This ensures a varying time delay  $\tau$  between the pulse pairs emitted by both sources. **B** Time domain representation of **A**. The sources generate two pulse trains, slowly sliding over each other, resulting in a beating signal on the detector, which will detect the absolute square of the incident fields. Due to its limited bandwidth the signals are low pass filtered. **C** Frequency domain representation of **A**. The sources have different repetition rates, leading to a different comb mode spacing. Mixing of the two fields generates sum and difference frequency terms, of which only the difference term is measured due to the low pass characteristic of the photodetector

in the cavity round trip times:

$$\tau = \frac{1}{f} - \frac{1}{f + \Delta f} = \frac{\Delta f}{f^2 + \Delta f f} \approx \frac{\Delta f}{f^2} \quad (2.11)$$

Two pulsed lasers, for example, operating at 100 MHz and 100 MHz + 10 Hz have a time delay increase from pulse pair to pulse pair of around one femtosecond. Equation 2.11 can be used to parametrize  $\tau$  in Equation 2.9 as  $\tau = \Delta f / f^2 \sum \sigma(t - nT)$ , but it would oversimplify the actual situation, as the two lasers can, for example, have a different spectrum and different carrier envelope offset frequencies.

### The Interferometric Signal

To accurately account for different laser operating parameters, the intensity on the detector shall be considered again. The fields of the two lasers are called  $E_1(t)$  and  $E_2(t)$ , the respective slowly varying amplitudes  $A(t)$  and  $B(t)$  and the repetition periods  $T_{rep1}$  and  $T_{rep2}$ :

$$I(t) = |E_1(t) + E_2(t)|^2 \propto Re (A(t) \otimes \text{III}(t - nT_{rep1})B(t) \otimes \text{III}(t - nT_{rep2})) \quad (2.12)$$

resolving the absolute square generates mixing terms between the two fields. Using Equation 2.3 and Equation 2.5, isolating only the slowly oscillating term (i.e. the difference term) and dropping the fast oscillating terms (i.e. the sum frequency and the second harmonic terms) leads to:

$$\begin{aligned} I(t) &\propto \sum_n A_n^* e^{-i2\pi(f_{ceo_n} + n f_{rep})t} \sum_m B_m e^{i2\pi(f_{ceo_m} + m(f_{rep} + \Delta f))t} \\ &\propto \sum_n \sum_l A_n^* B_{n-l} e^{i2\pi(f_{ceo_m} - f_{ceo_n} + (l f_{rep} + (n-l)\Delta f))t} \\ &\propto \sum_l e^{-i2\pi l(f_{rep} + \Delta f)t} \sum_n A_n^* B_{n-l} e^{i2\pi(f_{ceo_m} - f_{ceo_n} + n\Delta f)t} \end{aligned} \quad (2.13)$$

with  $l = n - m$  and the approximation that  $B(n - l) \approx B(n)$ , which is true if  $n$  and  $m$  are identical and gets worse with increasing difference between  $n$  and  $m$ . If now only case  $m = n$  is taken into account and the carrier envelope frequency difference is defined as  $\Delta f_{ceo} = f_{ceo_m} - f_{ceo_n}$  Equation 2.13 simplifies to:

$$I(t) \propto \sum_n A_n B_n^* e^{i2\pi(\Delta f_{ceo} + n\Delta f)t} \quad (2.14)$$

The carrier of the product  $\sum_n A_n B_n^*$  is located in the radio frequency domain ( $\propto e^{(n\Delta f)}$ ), whereas, the carriers of  $A_n$  and  $B_n$  are located in the optical domain ( $\propto e^{(nf_{rep})}$  and  $\propto e^{(m(f_{rep}+\Delta f))}$ ). The carrier of the (mixing-)product is therefore down converted from the optical to the radio frequency range. The down conversion factor  $d = \Delta f / f$  (radio frequency to optical frequency) is solely determined by the difference in repetition rate  $\Delta f$  between the two laser systems. Furthermore, the frequency coverage of the product  $\sum_n A_n B_n^*$  is compressed by  $d = \Delta f / f$  as well as offset from zero by  $\Delta f_{ceo}$ .

The down converted signal is located in half of the frequency band, spanning from zero to the repetition rate of the laser  $f_{rep}$ , which is referred to as the free spectral range, while the frequency band from zero to the repetition rate of the laser  $f_{rep}$  is referred to as the base band in the following. The signal repeats itself, in the frequency domain, with a spacing of the laser repetition rate  $f_{rep}$  (in fact, it is shifted by  $f_{rep} + \Delta f$  but  $f_{rep} + \Delta f \approx f_{rep}$ ). The shifted copies of the base band signal arise from the summation over  $l$  in Equation 2.13, i.e. the case when  $m \neq n$  (following the definition of  $l$  as  $l = n - m$ , if  $n > m$  copies covering from  $f_{rep}$  to  $\infty$  are generated and from zero to  $-\infty$  if  $n < m$ ).

In an intuitive picture of the calculus made above, the difference  $\Delta f$  causes one of the pulse trains to slowly slide over the other. Pulse pairs are generated with a varying time delay  $\tau$ . These pulse pairs interfere on the photodetector and generate beating signals as indicated in Figure 2.1C. Pulse pairs arrive with nanosecond period compared to the femtosecond time-scale of the optical signals, allowing the signal to be detected using common electronics. The low pass filtering effect of the detector converts this time-discrete signal in a time-continuous signal by filtering out harmonics beyond the base band (i.e. above mentioned copies if  $n \neq m$ ).

In the frequency domain, the down conversion can be understood by realizing that the difference in repetition rate leads to a different comb mode spacing of the two combs. The modes of the comb with the additional frequency  $\Delta f$ , which can be positive or negative, have a linearly increasing frequency difference to the comb without  $\Delta f$ . This situation is plotted in Figure 2.1D, the upper optical frequency comb is supposed to have a slightly higher repetition rate than the optical frequency comb below; by frequency mixing these two combs a difference and sum frequency spectrum is generated. The fundamental and the up converted frequencies are, by far, beyond the response times of detectors and contribute a DC term. Only the down converted spectrum is measurable. If not the nearest neighbouring comb lines ( $m = n$ ) are mixed but the next but one comb lines the mixed signals are shifted in frequency (in this case  $m - n = \pm 1$ ).

## Resolution

The achievable resolution, in a dual-comb experiment, can be deduced from Equation 2.14. Assuming delta pulses i.e.  $A_n = B_n = 1$  for all frequencies and taking into account that an actual measurement will only last a given time interval  $T_{measurement}$ ,

which can be taken into account by multiplication with a boxcar function  $\Pi_{T_{\text{measurement}}}$  of width  $T_{\text{measurement}}$ , leads to the intensity dependence:

$$I(t) \propto \text{III}(t - n(1/\Delta f)) \Pi_{T_{\text{measurement}}} \quad (2.15)$$

Multiplication with a boxcar function in the time domain is equivalent to a convolution with a sinc-function in the frequency domain. This gives the otherwise infinitesimally wide spectral features of the shah-distribution a width determined by the width of the sinc.

The resolution in the optical domain  $\Delta f_{\text{opt}}$  is computed as the resolution of the down converted spectrum  $\Delta f_{\text{RF}}$  times the inverse of the down conversion factor:

$$\Delta f_{\text{opt}} = \Delta f_{\text{RF}} \frac{1}{d} \quad (2.16)$$

It can be obtained intuitively by realizing that during the measurement time  $T_{\text{measurement}} = 1/\Delta f_{\text{RF}}$ , a certain number  $N$  of pulse pairs have been produced in the optical domain:

$$N \approx [T_{\text{RF}} f_{\text{rep}}] \quad (2.17)$$

[...] stands, in this case, for round to next integer. The maximal time delay is calculated as the number of pulse pairs times the increase in delay from pulse pair to pulse pair. Finally the resolution calculates as the inverse of it:

$$\frac{1}{T_{\text{opt}}} = \frac{1}{N \tau} = \frac{1}{T_{\text{RF}} f (\Delta f / f^2)} = \frac{1}{T_{\text{RF}}} * \frac{1}{d} \quad (2.18)$$

The resolution in the optical  $\Delta f_{\text{opt}}$  in principle depends only on the measurement time and the downconversion factor  $d$ . The (maximal) resolution is limited by the mode spacing of the frequency combs and their line width. A spectral feature can not be resolved when it is smaller than the mode spacing, e.g. if it falls between two comb modes it is metaphorically speaking not seen. The comb line width limits the resolution due to the fact that the frequency coverage of the product  $\sum_n A_n B_n^*$  is indeed compressed by  $d = \Delta f / f$  but not the width of the individual coefficients  $A_n$  and  $B_n^*$ . A comb line with a width of 10 Hz in the optical domain will also have a width of 10 Hz in the radio frequency domain.

### Minimal Downconversion

To have the shortest acquisition time for a given optical resolution, the downconversion factor supposedly should be as small as possible. However, the maximal signal bandwidth appearing in the recorded signal should not surpass half of the sampling rate to avoid aliasing [39, 40]. If the sampling rate of the digitization system used to record the signal is supposed to be arbitrarily high, the maximal signal bandwidth is limited by the optical sampling of the two pulse trains. Assuming that in Equation 2.12 at least one of the pulse trains consists of delta pulses (in this case  $B = 1$  for all frequencies) allows rewriting it to:

$$I(t) \propto A(t) \otimes \text{III}(t - nT_{rep1})\text{III}(t - nT_{rep2}) \propto f(t) \text{III}(t - nT_{rep2}) \quad (2.19)$$

A multiplication of an arbitrary function  $f(t)$  with a Shah-distribution leads to an evenly sampled function, with a sampling frequency inversely proportional to the spacing of the III. This sampling frequency is the repetition rate of the laser systems (assuming  $f_{rep} \approx f_{rep} + \Delta f$ ), which implies that the down converted signal can maximally fill out a frequency band of half of the repetition rate without being aliased. If the signal has a larger bandwidth, a part of it leaks into another free spectral range and is folded back. Under these circumstances the folded comb lines can not be assigned unambiguously anymore, except the comb lines are resolved and do not overlap with unfolded comb lines, which allows to assign them using their known spacing  $f_{rep}$ . The down converted optical bandwidth  $F_{opt} * d$ , has to be smaller or equal to half of the repetition rate  $f_{rep}/2$ :

$$f_{rep}/2 = F_{opt} * d_{min} \Rightarrow d_{min} = \frac{f_{rep}}{2 F_{opt}} \quad (2.20)$$

with the minimal downconversion factor  $d_{min}$ . For example, a spectrum spanning from 600 nm to 800 nm, corresponding to  $F_{opt} \sim 122,5$  THz of bandwidth, is supposed to be down converted into a radio frequency bandwidth of 50 MHz (i.e. for a system with 100 MHz repetition rate), which would allow a minimal downconversion factor of approximately  $4 * 10^{-7}$ .

### Dead Time

A small downconversion factor  $d$  is also advisable due to a problem particular to dual-comb spectroscopy. Equation 2.14 reveals this problem, the interferometric signal repeats itself periodically with a frequency equal to the difference in repetition rate  $\Delta f$ :

$$I(t) \propto \text{III}(t - n(1/\Delta f)) \quad (2.21)$$



**Figure 2.2:** Two interferograms in time, separated by the refresh time  $1/\Delta f$ . If information can only be gained in  $T_{\text{sampling}}$  a significant dead time is introduced between consecutive measurements.

If not the full time span from perfect overlap to perfect overlap is used for Fourier transform, a dead time is introduced between consecutive measurements, which is the refresh time ( $T_{\text{refresh}} = 1/\Delta f$ ) minus the measurement time, often also called sampling time  $T_{\text{sampling}}$ . The interferogram lasts a certain amount of time, which is (approximately) proportional to the coherence time of the sample times the downconversion factor:  $\tau_{\text{coherence}} * d$ . If the sample linewidth is large i.e. the coherence time short, then the interferogram intensity falls off rapidly and fills only a minor part of the time between perfect overlap to perfect overlap, such a case is depicted in Figure 2.2, the interferogram vanishes into the baseline after the sampling time  $T_{\text{sampling}}$ , covering a minor part of the time span between two consecutive interferograms introducing a dead time. For a typical linewidth of a liquid sample of 120 GHz and a downconversion factor of  $10^{-6}$  the interferogram lasts  $\sim 8,33 \mu\text{s}$ , whereas the time span from perfect overlap to perfect overlap, for a system operating at 100 MHz and a downconversion factor of  $10^{-6}$ , is 10 ms. A small downconversion factor aids in reducing the unwanted dead time, by reducing the refresh time and pushing the ratio measurement time to refresh time into a more favourable range.

### Sample Interaction

So far, no effects due to interaction of the fields with a sample are taken into account. As long as the interaction with the sample is linear it can be treated with the methods well known from signal analysis (e.g. [41]). The interaction in the time domain can be treated as a convolution with a suitable impulse response function of the sample or in the frequency domain as a simple multiplication with the corresponding transfer function of the sample. From Figure 2.3 it becomes clear that there are two possibilities to probe a sample in a dual-comb setup. The sample can be placed in a single arm of the interferometer or it can be probed by the combined beam.

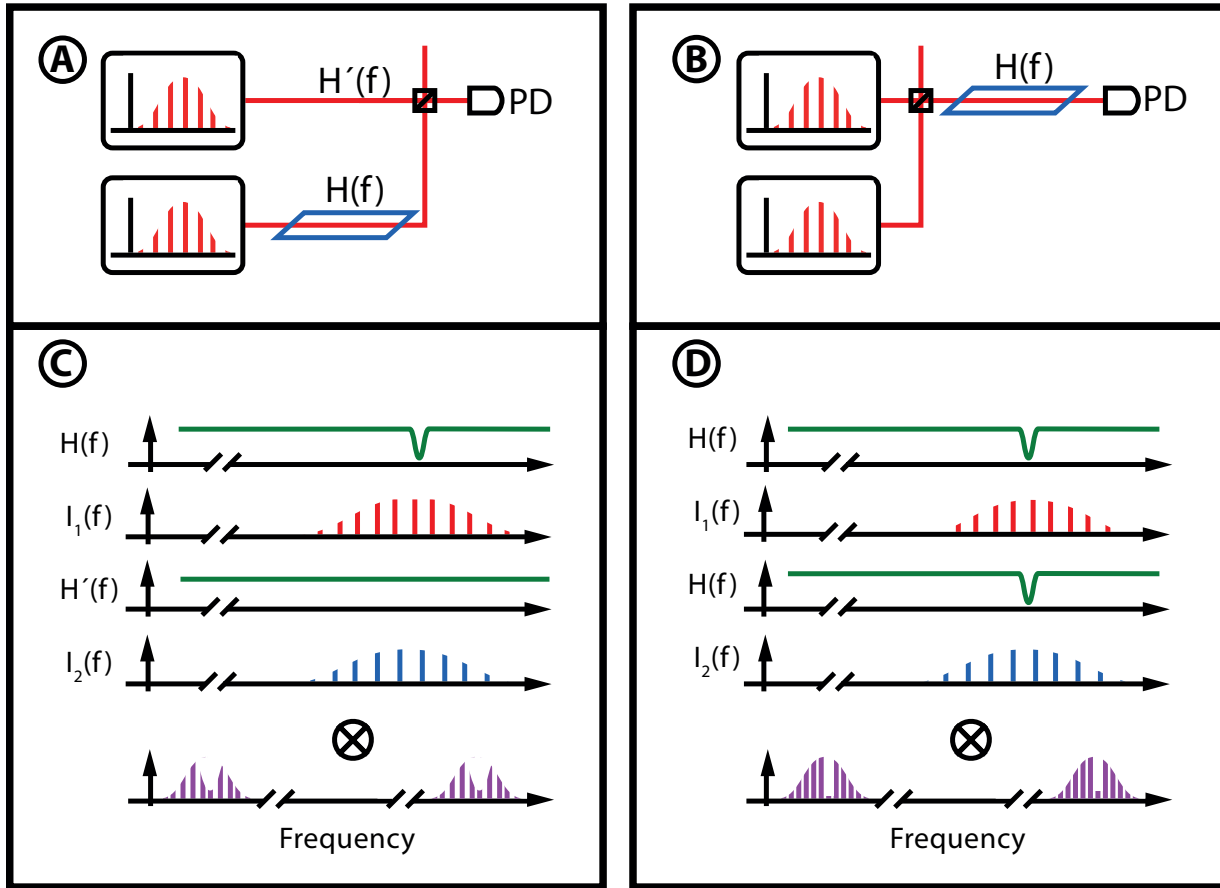


**Figure 2.3:** **A** and **B** possible placements of a sample in dual-comb spectroscopy. **A** a single beam, **B** both beams transit the sample. **C** Frequency domain description of case **A**. One beam experiences a transfer function different from unity. The other beam acts as a local oscillator only. **D** Frequency domain description of case **B**. Both beams experience a transfer function different from unity. The effect of the sample is more pronounced but the shape of the transfer function, imprinted on the spectrum, is changed.

Either of the two possibilities has its own appeals. If the sample is probed by one beam only as shown in Figure 2.3A the data analysis is rather straight forward. If the sample is probed by both beams as indicated in Figure 2.3B on the other hand the sensitivity is increased but the data analysis is more sophisticated.

For the first case, only a single beam transits the sample and experiences the transfer function  $H(f)$  of the sample system which can be e.g. an absorption cell. The other arm of the interferometer remains unperturbed. The intensity on the detector therefore is proportional to:

$$I(f) \propto E_1(f)H(f)E_2^*(f) \quad (2.22)$$

The second beam acts solely as a local oscillator down converting the field which probed the sample. If now e.g. a comb line has been absorbed, no downconversion can take place and hence no comb line appears at this point in the base band spectrum as indicated in Figure 2.3C.

If the second possibility is chosen and both beams transit the sample as depicted in Figure 2.3D, both fields need to be multiplied by the transfer function  $H(f)$  of the sample. Then the intensity on the detector is:

$$I(f) \propto E_1(f)H(f)E_2^*(f)H^*(f) \quad (2.23)$$

When both fields transit the sample, the interferometric signal on the detector has a quadratic dependence on the transferfunction  $H(f)$ , strongly enhancing the signal changes due to the effects imprinted by the sample on the light fields. On the other hand, data analysis is more difficult as the shape of the transfer function can be changed, e.g. a Gaussian shaped transfer function is a factor of square root of two narrower as seen by comparing Figure 2.3C (linear dependence) and Figure 2.3D (quadratic dependence)

### 2.2.3 Adaptive Sampling

A real world frequency comb does not possess perfectly stability, comb lines are not infinitely narrow, the frequency of the carrier is not infinitely precise defined etc. . To account for fluctuations in the comb mode frequencies, the comb Equation 2.5 can be modified by adding terms accounting for fluctuations. The analysis of noise in mode-locked lasers and its effects on the laser behaviour in the time and frequency domain is a wide field which has been explored carefully e.g. [42, 43, 44, 45, 46, 47, 48, 49], in the following a heuristic way is chosen showing the noise contributions leading to distortions in the recorded signals. Readers interested in a in depth treatment of noise in mode-locked lasers, will find in the before mentioned references a good starting point. In our Group, the development of the adaptive sampling scheme was pioneered by A. Poisson, whos thesis provides detailed information about adaptive sampling[50].

#### Comb Fluctuations

To account for fluctuations in the carrier envelope phase slip the term  $\delta\varphi(t)$  is introduced in Equation 2.5, which can be e.g. caused by small fluctuations of the intra-cavity dispersion e.g. by some air flow. To account for fluctuations in the repetition rate, the term  $\delta T(t)$  is introduced, which can be caused e.g. by small changes in the cavity length e.g. by small vibrations of the cavity mirrors.  $\delta\varphi(t)$  and  $\delta T(t)$  are both time dependent

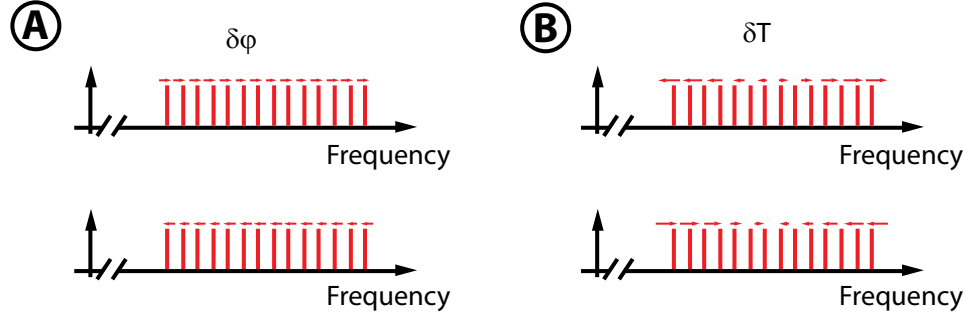


**Figure 2.4:** **A** Flow in the frequency domain. All modes move in the same direction by the same amount. **B** Breathing in the frequency domain. Modes move to or away from a certain frequency. The amount of movement is determined by the distance to this point.

for clarity the time dependence will not be written out in the following i.e.  $\delta\varphi(t) = \delta\varphi$ . Including these terms will modify Equation 2.5:

$$\begin{aligned}
 E(t) &= A(t) \sum_n e^{i2\pi\left(\frac{\Delta\varphi+\delta\varphi}{T_{rep}+\delta T} + \frac{n}{T_{rep}+\delta T}\right)t} \\
 &= A(t) \sum_n e^{i2\pi\left((\Delta\varphi+\delta\varphi)(f_{rep}+\delta f_{rep})+n(f_{rep}+\delta f_{rep})\right)t} \quad (2.24)
 \end{aligned}$$

Expanding and sorting the terms in the exponent, motivates the following approximation:

$$\begin{aligned}
 \Delta\varphi f_{rep} + n f_{rep} + \delta\varphi f_{rep} + n\delta f_{rep} + \Delta\varphi\delta f_{rep} + \delta\varphi\delta f_{rep} \\
 \approx \Delta\varphi f_{rep} + n f_{rep} + \delta\varphi f_{rep} + n\delta f_{rep} \quad (2.25)
 \end{aligned}$$

The first terms are the carrier envelope frequency  $\Delta\varphi f_{rep} = f_{ceo}$  and the repetition rate  $f_{rep}$ . The following two terms are related to fluctuations in the carrier envelope phase slip and to fluctuations in the repetition frequency. The last two terms are small compared to the first four terms and can be ignored without introducing a significant error. The effects of  $\delta\varphi$  and  $\delta f_{rep}$  are quite different. Both move the comb lines but in a different manner. Fluctuations of the carrier envelope phase  $\delta\varphi$  move the whole comb up and down in frequency as indicated in Figure 2.4A. An up and down moving of the entire comb without change of comb line spacing is referred to as flowing. On the other hand the fluctuations in the repetition rate  $\delta f_{rep}$  do not induce this flow but the comb mode spacing changes, depending on the mode number  $n$ . The whole comb is moving away

from or to some specific frequency, which can but does not need to be zero as indicated in Figure 2.4B, this kind of behaviour is referred to as breathing. It is important to keep in mind that this very intuitive picture is mathematically not correct, to observe a movement of the comb lines, small windowed portions of a long time trace would have to be Fourier transformed, in the sense of a short-time-Fourier-transform or a wavelet-transform. This leads to a poor resolution in the frequency domain, masking the movement of the comb lines or, if the time window is taken small, the comb lines themselves. Applying these simplifications to Equation 2.24 and taking the mixing term between the two fields in the usual way, however with this modifications included yields a result very similar to Equation 2.14, but additional terms accounting for laser fluctuations appear, the indices mark each laser i.e.  $E_1(t)$  corresponds to the electric field of the first laser and  $E_2(t)$  corresponds to the electric field of the second laser:

$$I(t) \propto A_1(t)A_2^*(t) \sum_n e^{i2\pi(\Delta f_{ceo} + n\Delta f)t} e^{i2\pi(\delta f_{ceo} + n\delta f)t} \quad (2.26)$$

with  $\delta f_{ceo} = \delta\varphi_1 f_{rep1} - \delta\varphi_2 f_{rep2}$  and  $\delta f = \delta f_{rep1} - \delta f_{rep2}$ . Equation 2.26 implies that only relative fluctuations between the two optical frequency combs lead to distortions.

There are two possible paths to deal with this distortions. One way is to stabilize the laser systems in a very stringent way pushing these fluctuations beneath a tolerable amount. What sounds straight forwards proves to be a demanding challenge e.g. for a highly resolved spectrum the timing jitter introduced by the laser fluctuations has to be lower than the atomic unit of time. This kind of stability is very hard to reach and only recently development in this direction has been made [51, 52].

### Error signals

The other path to follow is letting the lasers run freely and record all fluctuations simultaneously to the measurement and then employ a software based correction scheme to compensate for the fluctuations [53, 54, 55, 56, 57]. To record the fluctuations between the two laser frequency combs each of them is combined separately with a CW laser operating at a wavelength covered by the laser frequency comb spectrum. The beats between the laser frequency combs and the CW laser are detected on a photodetector. If only the nearest neighbour to the CW mode is taken into account i.e. the comb mode with mode number  $n_{CW}$ , the beat has a frequency appearing in half of the base band. The mixing term between CW laser, with the envelope of the CW laser  $A_{cw}(t)$ , and optical frequency comb can then be written as:

$$I(t)_{1,2} \propto A_{1,2} A_{cw}^*(t) e^{i2\pi(\Delta f_{ceo} + n_{CW} f_{rep} + \delta f_{ceo} + n_{CW} \delta f - f_{cw})t} \quad (2.27)$$

This mixing term contains information about fluctuations of a single frequency comb mode. If the CW laser is not perfectly stable as assumed in the calculus above, the fluctuations of the CW laser also flow into this signal. As perfectly stable lasers do not exist in this world, this poses a major problem. The demands on the CW laser stability would be at least as high as the demands concerning the stability of the frequency comb itself. Thereby the stability problem has only been shifted from the optical frequency comb to the CW laser.

Examining Equation 2.26 nevertheless reveals that only relative fluctuations between the two optical frequency combs lead to distortions. To retrieve the relative fluctuations between the two optical frequency combs, the beat notes of the two laser frequency combs and the CW laser, are mixed in a radio frequency mixer. By doing so the contribution of the CW laser is cancelled out and only the relative fluctuations of the two optical frequency combs are gained, elegantly circumventing the need for an ultra stable CW laser. The signal after the mixer  $\tilde{s}(t)_{CW1}$  contains a up and a down mixed term of which only the down mix  $s(t)_{CW1}$  should be considered in the following:

$$s(t)_{CW1} \propto A_1(t)A_2^*(t)A_{cw}^* e^{i2\pi(\Delta f_{ceo} + (n_{CW}f_{rep1} - m_{CW}f_{rep2}))t} e^{i2\pi(\delta f_{ceo} + (n_{CW}\delta f_{rep1} - m_{CW}\delta f_{rep2}))t} \quad (2.28)$$

with  $n_{CW}$  and  $m_{CW}$  as the mode numbers of the nearest neighbouring modes of the two optical frequency combs to the CW laser. Recording the beat frequencies of the individual optical frequency combs against the CW laser and mixing them to cancel contributions of the CW laser, additionally acted as a very narrow band filter isolating only one comb mode from each optical frequency comb. Technically it is indeed possible to replace the detection of the beat signal between a CW laser and the optical frequency comb with some very narrow band filters (e.g. [55]). For a common optical frequency comb a pass band of some hundred megahertz at best is needed, usually it is supposed to be even smaller. This proves to be quite challenging in the optical domain, taking the tremendous bandwidth of an optical signal into consideration.

To achieve a perfect correction of the recorded interferogram a correction not only at one point i.e. one CW laser wavelength is sufficient but a second point has to be used. Intuitively, after correcting at one point, the comb in the radio frequency domain does not flow in frequency but it still can exhibit a breathing behaviour. The second correction signal is gained in the same way as the first one, as a beat against a CW laser followed by radio frequency mixing. The wavelength of the second laser obviously has to be different yielding a second correction signal which shall be called  $s_2(t)$  whereas the first correction signal shall be called  $s_1(t) = s(t)_{CW1}$ . The only difference between  $s_1(t)$  and  $s_2(t)$  following Equation 2.28 are the mode numbers  $n_{CW1,2}$  and  $m_{CW1,2}$ .

### Adaptive Correction

The actual correction can be done using a soft or hardware based scheme. In the course of this thesis only software based correction is used. In the first step of the software based correction scheme the interferogram signal, i.e. the dual-comb signal  $s(t)_{int}$ , is corrected by multiplication with the complex conjugated normalized correction signal:

$$\acute{s}(t)_{int} \propto s(t)_{int} \frac{s_1^*(t)}{|s_1(t)|} \propto \sum_n e^{i2\pi(n\Delta f_{rep} - \Delta f_{CW})t} e^{i2\pi(n\delta f_{rep} - \delta f_{CW})t} \quad (2.29)$$

condensing  $n_{CW1}f_{rep1} - m_{CW1}f_{rep2}$  to  $\Delta f_{CW}$  and  $n_{CW1}\delta f_{rep1} - m_{CW1}\delta f_{rep2}$  to  $\delta f_{CW}$ . Examining Equation 2.29 reveals that there is no dependence anymore which causes a flowing of the radio frequency comb. The fluctuation terms remaining are the ones, which cause a breathing of the comb. To remove the contributions of  $\delta f_{rep}$ , the second correction signal  $s_2(t)$  it is corrected by the first correction signal  $s_1(t)$ :

$$\acute{s}(t)_2 \propto \frac{s_2(t)}{|s_2(t)|} \frac{s_1^*(t)}{|s_1(t)|} \propto e^{i2\pi(\Delta f_{CW1} - \Delta f_{CW2})t} e^{i2\pi(\delta f_{CW1} - \delta f_{CW2})t} \propto e^{i2\pi(\Delta f_{CW1} - \Delta f_{CW2})t} e^{i2\pi\Phi(t)} \quad (2.30)$$

The first frequency term of  $\Delta f_{CW1} - \Delta f_{CW2}$  is constant over time, it is the beat of the CW lasers with the nearest comb modes of the unperturbed comb. Therefore any deviation from the constant frequency  $\Delta f_{CW1} - \Delta f_{CW2}$  is caused by the second term  $\delta f_{CW1} - \delta f_{CW2}$ , which describes the phase noise  $\Phi(t)$  introduced to the signal by fluctuations of the repetition rates.

The second step in the correction of the interferogram makes use of the fact that this phase noise term can also be expressed as a timing jitter. Intuitively this can be seen by considering a harmonic signal with a single frequency. Without any phase noise or timing jitter the signal has a certain value  $a(t)$  at a certain point in time  $t_0$ . Phase noise  $\Phi(t)$  shifts the instantaneous frequency of this signal. The, now frequency shifted, harmonic signal has a different value  $a_{phasenoise}(t)$ , if probed at the same instant of time  $t_0$ . On the other hand if the original harmonic signal is not shifted by a phase noise term in instantaneous frequency but the signal is sampled at a slightly different instant in time  $t_0 + \delta t$  again a value  $a_{timingjitter}(t)$  different from the unperturbed signal is found. It is now possible to find a timing deviation  $\delta t$  for every  $\Phi(t)$  in a way that  $a_{phasenoise}(t) = a_{timingjitter}(t)$  is true for every point in time. This changing between phase noise and timing jitter allows to rewrite Equation 2.30 to:

$$\acute{s}(t)_2 \propto \frac{s_2(t)}{|s_2(t)|} \frac{s_1^*(t)}{|s_1(t)|} \propto e^{i2\pi((\Delta f_{CW1} - \Delta f_{CW2})(t + \delta t))} \quad (2.31)$$

Assuming that this signal  $\acute{s}(t)_2$  is sampled in evenly spaced time intervals, for example, in a way that always the zero crossings of  $\acute{s}(t)_2$  are sampled, if the timing jitter  $\delta t$  is zero for all times. A non zero timing jitter causes  $\acute{s}(t)_2$  to have a non zero value when sampled. In this case it is also possible to think of an unperturbed signal and a disturbed sampling, sampling the signal not at evenly spaced time intervals but at time intervals modulated by the timing jitter. Coming from this unevenly sampled signal to an evenly sampled signal corrects for the timing jitter. To do so the timing jitter is extracted from the second correction signal making use of Equation 2.31. With this information the interferogram is interpolated on an evenly spaced timing grid compensating for the timing jitter  $\delta t$ . After applying the two correction steps a perfectly corrected signal free from distortions caused by either of  $\delta\varphi$  or  $\delta t$  is obtained.



## Chapter 3

# Linear Mid-Infrared Spectroscopy

Fundamental vibrational molecular transitions are located in the spectral band from about 2 to 20  $\mu\text{m}$ , the spectral region of the mid-infrared to far infrared. Mid-infrared radiation covers the spectral band from about 2 to about 10  $\mu\text{m}$ . It is a region of very high interest as nearly all molecules have strong fundamental vibrational transitions in this frequency band. Linear spectroscopy in this band promises a high sensitivity as fundamental transitions offer cross-sections much larger than their overtones in the near infrared or visible range. This fact makes mid-infrared spectroscopy a good candidate when only very small quantities of the sample under scrutiny are present. This can be, for example, trace gas sensing or medical/biochemical applications where huge quantities of e.g. protein sample are hardly available. The transitions in the mid-infrared are highly specific for a given functional group (e.g. [58]) as indicated in Figure 3.1. Different functional groups have different transitions, especially the low wavenumber region from about 1200 to 200  $\text{cm}^{-1}$  is highly characteristic which gave rise to its name: the fingerprint region. Another band of special interest is the wavelength band around 3  $\mu\text{m}$  corresponding to 3333  $\text{cm}^{-1}$ . Strong transitions of carbon hydrogen, hydrogen nitrogen, hydrogen sulphur and oxygen hydrogen bonds are located in this region. These are characteristic bonds for biological molecules like lipids, peptides and carbon hydrates, making it a very interesting region for biochemical or medical applications. Taking spectra in a linear manner allows for easy quantitative analysis of the spectrogram which is a problem for nonlinear techniques as for example coherent Raman scattering.

The mid-infrared spectral band is a spectral region which is hard to enter because light sources and photonic tools are much less evolved than in the visible or near infrared. Nevertheless, in the recent years a huge effort was taken to approach this wavelength region. For a long time only low brilliance light sources were available for spectroscopy in this wavelength region as for example Nernst glowers or the Globar glower. Light sources made from ceramic material, heated by electric current, radiating black body radiation rich in mid-infrared light. These sources are very broadband but neither is the brilliance of this sources high nor is the emitted radiation coherent. The development of

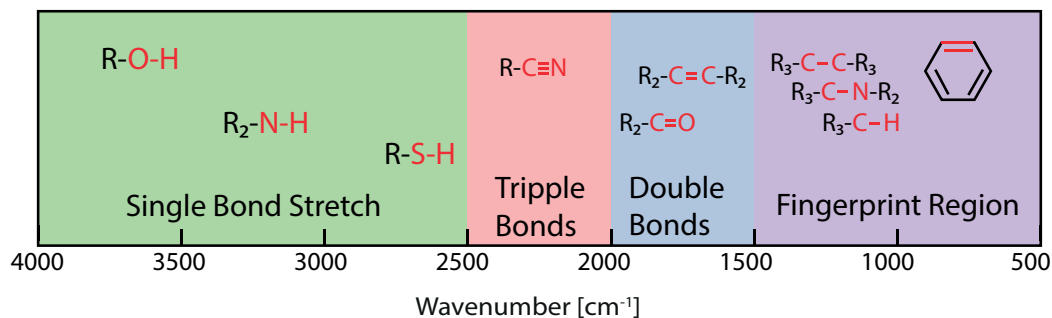


**Figure 3.1:** Transitions of selected functional groups in the mid-infrared. Especially the region from  $1500\text{ cm}^{-1}$  to  $500\text{ cm}^{-1}$  is highly specific.

sources emitting high brilliance coherent light in the mid-infrared allowed transferring coherent measurement techniques developed in the visible and near infrared to the mid-infrared frequency band.

The new sources are multifaceted ranging from lasers producing radiation directly in the mid-infrared, which are based on transition metal doped chalcogenide glass, as for example  $\text{Cr}^{+2}$  doped ZnSe ([59, 60, 61, 62]) or rare earths ions as Thulium and Holmium ([63, 64, 65, 66, 67]), over semiconductor quantum cascade lasers ([68, 69, 70]) to techniques using nonlinear optical conversion processes to downconvert visible or near infrared radiation into the mid-infrared wavelength regime either using difference frequency generation ([71, 72, 73]) or optical parametric oscillation ([74, 75, 76, 77]).

All of these techniques have their own charms. In our case nonlinear optical downconversion using an optical parametric oscillator was chosen as the most suitable light source. The reasons leading to this decision are the need for as broad as possible spectral coverage, a wide tuning range of the source and the possibility of generating ultra-short, ideally chirp free, pulses. Ultra-short pulses emitted from an optical parametric oscillator allow to harness nonlinear processes in the mid-infrared, for example broadening the spectrum generated in the optical parametric oscillator to achieve an octave spanning spectrum, which can be used to e.g. build a self-referenced optical frequency comb in the mid-infrared using common techniques.

## 3.1 Mid-Infrared Optical Parametric Oscillator

*Related Article[78]:*

*Few-cycle, Broadband, Mid-infrared Optical Parametric Oscillator Pumped by a 20-fs Ti:sapphire Laser*

*S. Chaitanya Kumar, A. Esteban-Martin, T. Ideguchi, M. Yan, S. Holzner, T. W. Hänsch, N. Picqué, and M. Ebrahim-Zadeh*

*The optical parametric oscillator system described in this section was developed in cooperation with the ICFO-Institut de Ciencies Fotoniques in Spain. In charge of the development of the system were Suddapalli Chaitanya Kumar and Adolfo Esteban-Martin in the group of Majid Ebrahim-Zadeh. The calculations as well as the setup of the systems was done in Spain then the characterization and testing of the system was done at the Max-Planck Institut fuer Quantenoptik, in Germany. My own contributions are: re-Setup of the optical parametric oscillator at MPQ together with S. Chaitanya Kumar, A. Esteban-Martin, T. Ideguchi and M. Yan. Setup of the required experimental apparatus for the temporal and spectral characterization of light generated by the optical parametric oscillator together with S. Chaitanya Kumar, A. Esteban-Martin, T. Ideguchi and M. Yan. Edited and discussed the manuscript.*

The key idea behind the optical parametric oscillator is nonlinear frequency conversion, e.g. of visible or near infrared light to mid-infrared light, with the aid of a parametric process. The, most commonly used, parametric process is the second order nonlinear response of a medium to the electric field of the incident light. This medium typically is a nonlinear crystal of which lithium niobate is a common material. It can be doped with up to ten percent magnesium oxide to prevent photorefractive damage, which can occur at the high intensity achieved by ultra-short laser pulses and/or due to cavity enhancement [79, 80]. A nonlinear crystal in a type one or type two phase matching configuration only allows for a broadband phase matching and hence an effective broadband down conversion when it is very thin. The problem of a very thin (short) gain medium is a low gain for a given pump intensity. To overcome this problem, the fact is harnessed that lithium niobate can be poled and by this a periodically poled crystal of lithium niobate (PPLN) can be manufactured [81, 82]. This allows efficient nonlinear conversion over a wide bandwidth [83, 84, 85].

For an optical parametric oscillator different configurations of the cavity are possible, a triply resonant, a doubly resonant or a singly resonant system. The triply resonant system is resonant for pump, signal and idler. In the doubly resonant system, both signal and idler light generated in the nonlinear downconversion process are resonant in the optical parametric oscillator cavity. In the singly resonant case only one of them is resonant in the optical parametric oscillator cavity. Under the prospect of an as broad as possible output spectrum in the mid-infrared having a doubly resonant optical parametric oscillator cavity is appealing. The doubly resonant system can offer a very large gain bandwidth

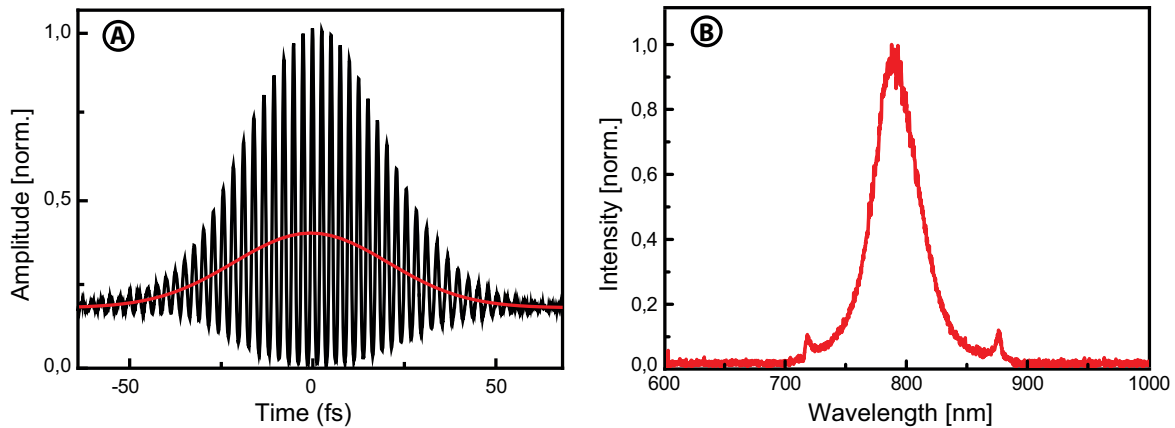


**Figure 3.2:** **A** Autocorrelation of the pump source (Synergy from Femtolasers) **B** Spectrum of the pump source (Synergy from Femtolasers).

in the vicinity of degeneracy [86, 87, 88]. The drawback of this approach is that the system has to be degenerate or near degeneracy, meaning that it can not be tuned easily i.e. for tuning the pump wavelength has to be changed. A singly resonant optical parametric oscillator cavity does not face this problem. It can be tuned continuously over the gain bandwidth of the system gain. Depending on the gain medium and the cavity design the system can have a considerable tuning range. Without the need of a tunable pump source, common pump sources can be employed. To gain an as broad as possible output spectrum a broadband pump source is used, in this case a broadband Titanium Sapphire oscillator. Such a pump source provides broadband ultra-short pulses which, if dispersion is compensated properly, allows for the generation of ultra-short broadband pulses in the near to mid-infrared in an optical parametric oscillator [74, 75].

### 3.1.1 Optical Parametric Oscillator Setup

The setup of the optical parametric oscillator is outlined in Figure 3.3. It is a singly resonant system with a linear, standing wave cavity. As nonlinear gain medium a periodically poled lithium niobate crystal is used and as pump source an ultra-short pulse Titanium Sapphire laser. A detailed description is given in the following sections.

#### Pump Source

As already mentioned the optical parametric oscillator is pumped by a Titanium Sapphire ultra-short pulse oscillator (Synergy from Femtolasers) delivering pulses of sub-twenty femtoseconds pulse duration with an average power of 1 W at a repetition frequency of 100 MHz, corresponding to a pulse energy of 10 nJ. Dispersion acquired on the pump beam path is precompensated by a pair of chirped mirrors (Layertec). To find the

right amount of precompensation, different values were tried and for every value an interferometric autocorrelation was taken at the position of the crystal. As best value  $-160 \text{ fs}^2$  was found, yielding the interferometric autocorrelation plotted in Figure 3.2A. It does not show any indication of distortions caused by higher order dispersion, the baseline is flat and no ripples in front and back of the interferometric signal are present. Figure 3.2B depicts the spectrum of the pump source, it is smooth with no indication of any pedestal or ripples. The two side-bands left and right of the main peak are Kelly side-bands [89, 90], which are parasitically generated and usually appear at the zero dispersion transit or close to the zero dispersion transit of the intra-cavity dispersion of the laser system. Being a problem as they limit the maximal spectral bandwidth of a laser system in the first place, their appearance indicates that the laser system produces the shortest possible output pulses or broadest spectrum, making a good observable for the health of the laser system. The spectrum spans about 40 nm (FWHM) at a central wavelength of  $\sim 790 \text{ nm}$  corresponding to more than  $640 \text{ cm}^{-1}$  spectral coverage (FWHM).

### Nonlinear Crystal

After dispersion compensation the Titanium Sapphire light is focused, with a 75 mm lens through cavity mirror  $M1$ , in the gain medium, with a beam-waist of  $50 \mu\text{m}$ . The gain medium is a one millimeter thick magnesium oxide doped periodically poled Lithium niobate chip. As indicated in the inset of Figure 3.3 the poling is not isotrop, the chip has four different poling zones corresponding to interaction lengths of  $250 \mu\text{m}$  to  $1000 \mu\text{m}$  increasing in  $250 \mu\text{m}$  steps. The crystal can be moved vertically to chose the desired interaction length. Inside of the different interaction zones, the poling is also not isotrop but has a fan out structure continuously increasing the poling period from 19 to  $23,3 \mu\text{m}$ . The fan out structure allows to optimize the gain bandwidth of the optical parametric oscillator.

### Cavity Mirrors

The cavity by itself is a standing wave cavity built from two concave mirrors  $M1$  and  $M2$  and four plane mirrors  $M3$  to  $M6$ . The mirror coating is designed to have high transmission at the pump and the idler wavelength, 90 and 80 percent respectively but a high reflectance of more than 99 percent at the signal wavelength. All mirrors have a chirp for dispersion control of the signal light. The intra-cavity dispersion is tuned close to zero for the wavelength region from 1000 to 1200 nm and from minus 600 to plus  $200 \text{ fs}^2$  from 1200 to 1600 nm.

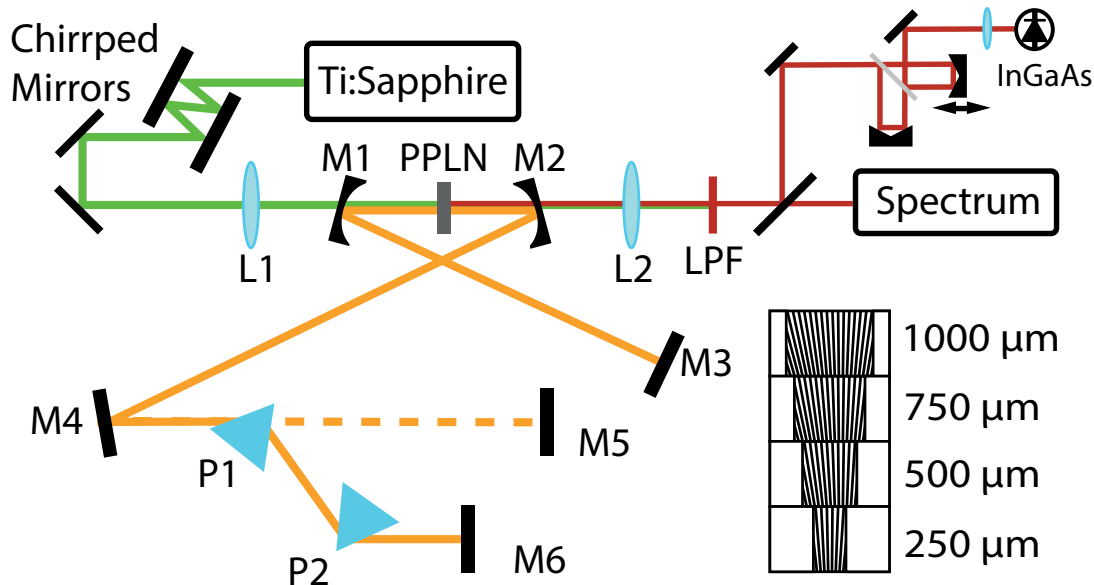


**Figure 3.3:** Schematic of the femtosecond optical parametric oscillator. L1 and L2 lenses; M1 and M2 curved cavity mirrors; M3 to M6 flat cavity mirrors; LPF low pass filter; PPLN periodically poled Lithium niobate.

### Optical Parametric Oscillator Cavity

The optical parametric oscillator supports two different beam paths inside of the cavity. If the prism  $P1$  is moved out of the beam, mirror  $M5$  acts as the end mirror of an axillary cavity used for alignment. When running in the axillary cavity alignment is simplified but dispersion control and wavelength selection is reduced. This becomes noticeable as the optical parametric oscillator tends to run on more than one spatial mode and has several peaks in the output spectrum. The high gain due to  $GW/cm^2$  level intensities involved in the pump focus of a femtosecond optical parametric oscillator allows higher order modes to cross the threshold relatively quick. Even more important, while pumping at the Titanium Sapphire wavelengths, the large parametric gain bandwidth of the periodically poled lithium niobate crystal allows oscillation at two or more different central signal wavelengths simultaneously and hence associated spatial mode issues can arise. Finally, non-phase-matched processes generate all kind of different wavelength contributions.

When moving prism  $P1$  into the beam the optical parametric oscillator operates in the normal mode, with prisms  $P1$  and  $P2$ , both made from SF11, in the beam path and mirror  $M6$  as end mirror. When the prisms  $P1$  and  $P2$  are inserted into the beam path the output spectrum of the optical parametric oscillator is cleaned up and a well defined smooth output spectrum is generated. The prisms select the centre wavelength of choice by introducing losses to other oscillating wavelengths and higher order modes while compensating for dispersion at the same time. Finally, as the optical parametric oscillator

becomes more sensitive to alignment by introducing the prisms into the beam path, careful alignment allows to sustain a TEM<sub>00</sub>-mode, which is free of higher order mode contributions. The idler light leaves the cavity through mirror *M2* and is collimated with the lens *L2*. The following long pass filter *LPF* finally removes all remaining pump light and the tiny amount of signal light leaking through the mirror *M2*

### Characterization Setup

Characterization of the output, the generated idler light, of the optical parametric oscillator is done using either a commercial Fourier transform spectrometer (VERTEX70 from Bruker) or a self-built interferometric autocorrelator. The Fourier transform spectrometer is used to verify the tuning capabilities and the spectral span of the optical parametric oscillator. Temporal characterization of the optical parametric oscillator is done with a self-built interferometric autocorrelator, employing hollow-cube-corner retro-reflectors, a broadband Pellicle beam splitter and an Indium Gallium Arsenide photo diode operating as a two-photon-detector.

### 3.1.2 Spectral and Temporal Characterization of the Parametric Oscillator

#### Spectral Characteristics and Tunability

In Figure 3.4A spectra taken with an interaction length of 500  $\mu\text{m}$  and 250  $\mu\text{m}$  are depicted. Spectral distortions are caused by absorption of the mid-infrared light in the laboratory atmosphere. Clearly, the supported bandwidth of the 250  $\mu\text{m}$  interaction zone is significantly larger than for 500  $\mu\text{m}$  interaction length, as an example: 225 nm ( $407\text{ cm}^{-1}$ ) bandwidth for 250  $\mu\text{m}$  interaction length as compared to 113 nm ( $114\text{ cm}^{-1}$ ) bandwidth for the 500  $\mu\text{m}$  interaction length (measured for an Idler spectrum centered around 2350 nm ( $4255\text{ cm}^{-1}$ )). Better phase matching in the shorter interaction length is the reason for the broader nonlinear gain bandwidth.

The drawback of having an interaction length of as short as 250  $\mu\text{m}$  is a considerably reduced tuning range of the optical parametric oscillator (approximately a factor of two compared to the 500  $\mu\text{m}$  interaction length), Figure 3.4B shows the tuning capabilities of the optical parametric oscillator as the power at different wavelengths. The central wavelength using the 500  $\mu\text{m}$  interaction length can be tuned over a range of more than 1550 nm ( $1467\text{ cm}^{-1}$ ), generating spectra, which can cover a band from 2000 to 4500 nm ( $2222\text{ cm}^{-1}$  to  $5000\text{ cm}^{-1}$ ).

At zero detuning wavelength, corresponding to approx. 2300 nm ( $4347\text{ cm}^{-1}$ ), the output power exceeds 50 mW. At the edges of the tuning range the output power still is above 30 and 20 mW for the high and low frequency cut off respectively, falling of rapidly for

central wavelengths smaller than  $\sim 2000$  nm ( $5000$   $\text{cm}^{-1}$ ) and wavelengths larger than  $3725$  nm ( $2684$   $\text{cm}^{-1}$ ).

### Temporal Characteristics

The  $500$   $\mu\text{m}$  interaction length offers the best trade-off between tuning ability and spectral bandwidth of the generated output spectra. When the broadest bandwidth is needed i.e. the shortest pulses, the  $250$   $\mu\text{m}$  interaction length prevails within its limited tuning range. To characterize the output pulses in the time domain, an interferometric autocorrelator is used, utilizing a Pellice as broad band low dispersion beam splitter. The autocorrelation is measured as the two photon absorption current in an Indium Gallium Arsenide photodetector [91, 92, 93]. The pulse duration of the output pulses employing the  $250$   $\mu\text{m}$  interaction length is approximately half of the pulse duration employing the  $500$   $\mu\text{m}$  interaction length. On the short wavelength side at  $2626$  nm ( $3808$   $\text{cm}^{-1}$ ), the optical parametric oscillator, using  $500$   $\mu\text{m}$  interaction length, produces pulses with  $64$  femtoseconds or  $7,4$  cycles (see Figure 3.5 right). When using the  $250$   $\mu\text{m}$  interaction length the pulse duration drops to  $32$  femtoseconds corresponding to  $3,7$  cycles (see Figure 3.5 left). A  $\text{sech}^2$  shape of the pulses is assumed and the standard parameter of  $1,897$  is used for deconvolution in order to calculate the pulse duration  $\tau_{pulse}$ :

$$\tau_{pulse} = \frac{Nt_0}{1,897} \quad (3.1)$$

with  $N$  as the number of fringes larger in (normalized) amplitude than  $0,5$  and  $t_0 = \lambda/c$  as the temporal distance between two consecutive fringes at the central wavelength  $\lambda$ . The short pulse duration at  $2626$  nm ( $3808$   $\text{cm}^{-1}$ ) indicates a very good dispersion compensation of the optical parametric oscillator at this wavelength. Adjusting the two prisms inside of the optical parametric oscillator cavity to optimize the dispersion compensation might lead to even shorter pulses at these wavelengths. As displayed in Figure 3.5C the pulse duration slightly increases for different central wavelengths of the optical parametric oscillator. The very short pulse durations in the wavelength range at  $2240$  nm ( $4464$   $\text{cm}^{-1}$ ) should be considered carefully as the laboratory atmosphere partially absorbs at this wavelength (the absorption is mainly attributed to water vapour). The strong wings of the autocorrelation shown in Figure 3.5B already indicate this when being compared to the autocorrelations taken at  $2626$  nm ( $3808$   $\text{cm}^{-1}$ ) (Figure 3.5A), which shows no wings for the  $500$   $\mu\text{m}$  interaction and only very minor wings, caused presumably by third order dispersion, for the  $250$   $\mu\text{m}$  interaction length.

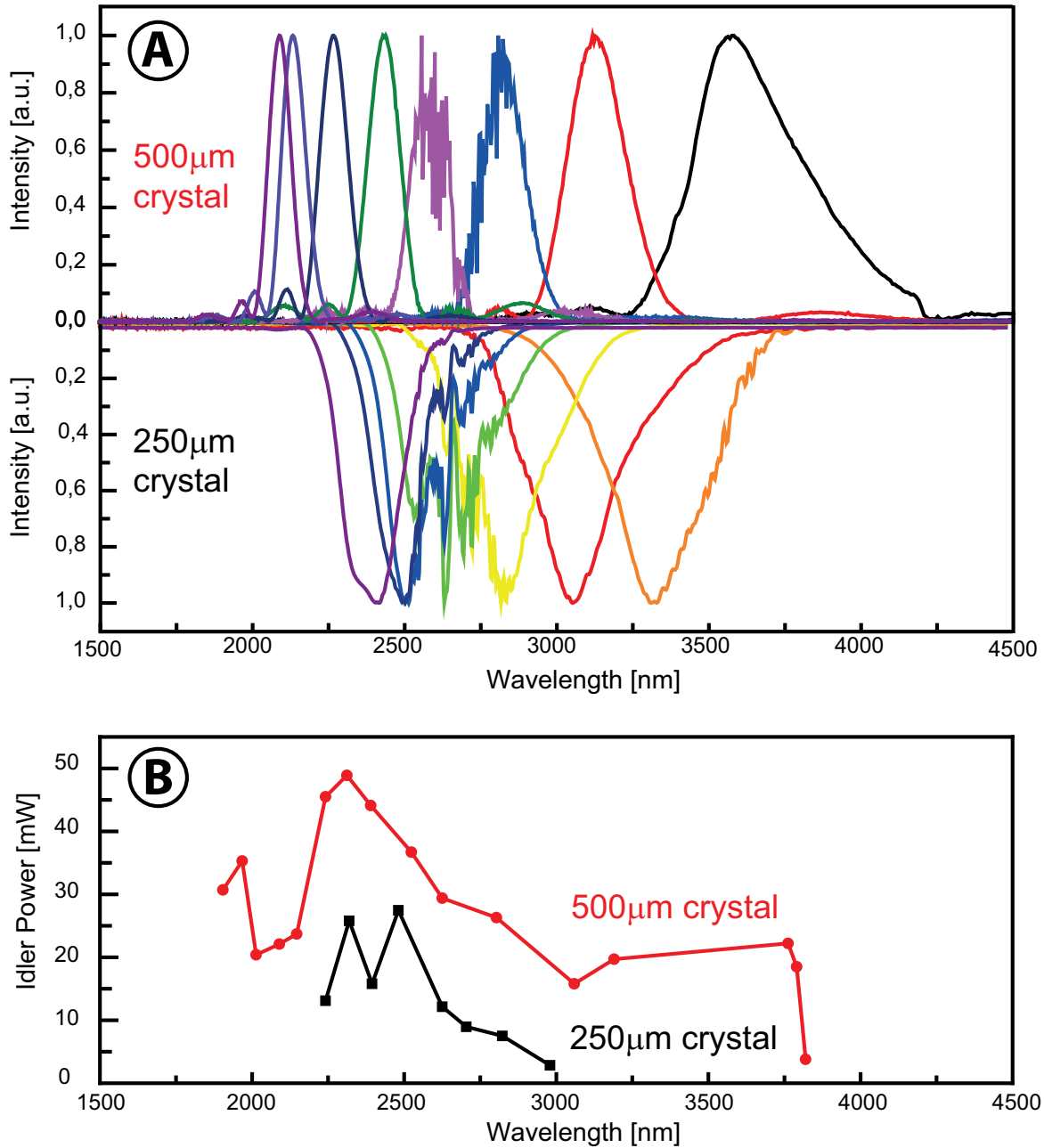


**Figure 3.4:** **A** spectra taken with 500  $\mu\text{m}$  interaction length (facing up) and 250  $\mu\text{m}$  interaction length (facing down). **B** Tunability of the optical parametric oscillator for 500  $\mu\text{m}$  and 250  $\mu\text{m}$  interaction length.

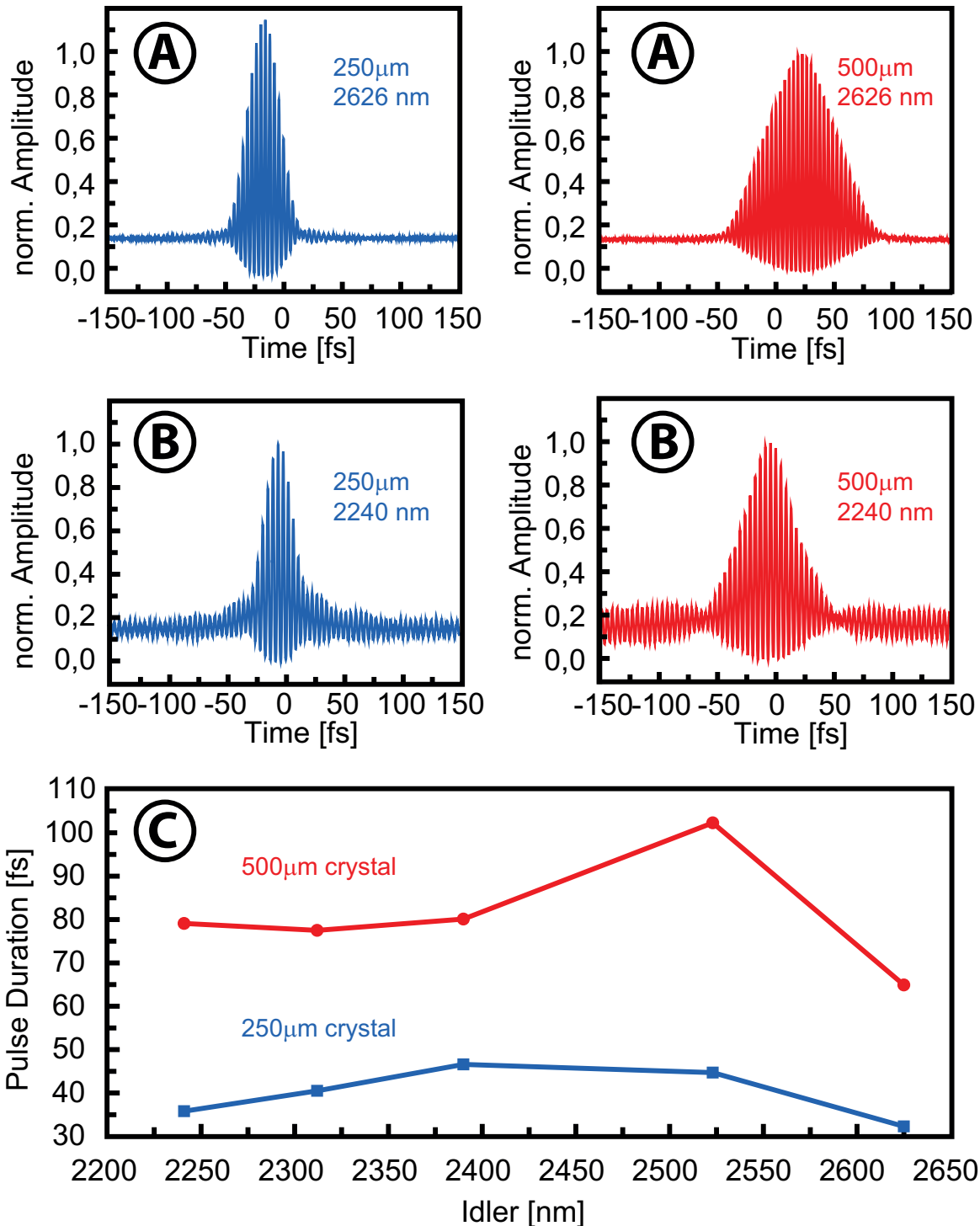


**Figure 3.5:** **A** Autocorrelation of the idler at 2626 nm for 250 μm and 500 μm interaction length. **B** Autocorrelation of the idler at 2240 nm for 250 μm and 500 μm interaction length. **C** Pulse duration of the optical parametric oscillator as a function of idler wavelength for 250 μm and 500 μm interaction length.

### 3.1.3 Summary Mid-Infrared Optical Parametric Oscillator

For dual-comb experiments two optical parametric oscillators have been constructed with matching parameters. Both are tunable from 2180 nm to 3730 nm central wavelength ( $(2680\text{ cm}^{-1})$  to  $(4587\text{ cm}^{-1})$ ), spanning more than 1550 nm ( $1467\text{ cm}^{-1}$ ) tuning range and covering a wavelength band from about 2000 to 4500 nm ( $2222\text{ cm}^{-1}$  to  $5000\text{ cm}^{-1}$ ). Their spectra are virtually identical in shape and span. This is also true for the generated output pulses concerning their duration. The output power is similar for both systems over the tuning range as well as the pump threshold of about 700 mW pump power.

## 3.2 Mid-Infrared Photonics

Despite of the broad spectral coverage of the optical parametric oscillator described in Section 3.1, most of the time an even broader spectral coverage is desired. To gain more bandwidth, the gain medium in the optical parametric oscillator would have to be even shorter. Shortening the crystal improves phase matching but at the expense of gain, which sets a lower limit to the crystal thickness. Similarly laser systems operating directly in the mid-infrared are limited in spectral coverage by the gain bandwidth of their corresponding gain medium. One possibility to attain a broader spectral coverage is harnessing supercontinuum generation, which holds promise for the most extreme spectral broadening in the low-field regime.

Supercontinuum generation was first reported in bulk material [94, 95]. Only high power laser sources delivering short pulses in the millijoule range could be used, as the peak intensity needed to be above the threshold of self trapping. Efficient broadening could only take place during a longer nonlinear interaction of the pump beam and the material. It was ensured by the self trapping, which provides the needed guiding of the beam. This changed with the advent of optical waveguides, especially fibers and thereof photonic crystal fibers, which did not only provide guiding but also allowed, for the first time, a precise engineering of the waveguide dispersion. Using these fibers made it possible to generate high brightness supercontinua [96, 97, 98]. Since then supercontinuum generation using these fibers found widespread interest as well as broad application in numerous fields e.g. in spectroscopy, pulse compression and frequency metrology, where it became one of the key ingredients in the development of the optical frequency comb. The advantage of photonic crystal fibers over other fiber types is the precise control of the modal confinement and the waveguide contributions to the dispersion, through the geometrical shape of core and cladding.

Usually, such fibers are made of silica, which prohibits their use in the mid-infrared as it does not transmit well in this wavelength range. Several non oxide based materials offer good transmission together with other beneficial attributes. One of these materials is silicon, it has a wide transmission range, up to  $7\mu\text{m}$  ( $1428\text{ cm}^{-1}$ ), and a high nonlinear refractive index (see e.g. [99]). An additional benefit of silicon are the already existing, well developed techniques from chip production in CMOS. Finally, silicon is stable under ambient conditions, a waveguide made from silicon will stay as is, if not damaged mechanically. Another very interesting set of material are chalcogenide glasses. In chalcogenide glasses oxygen is replaced by one of the other chalcogenides sulphur, selenium or tellurium. Due to their lower phonon energies these materials offer a very broad transmission range in the mid-infrared, surpassing the transmission range of silicon. Their nonlinear refractive indices are also high (e.g. [100]) but their linear refractive indices are lower (around two for the chalcogenide glasses compared to  $\sim 3,4$  of silicon). The lower refractive index contrast does not allow an as strong modal confinement as in silicon. In the course of this thesis supercontinuum generation has

been done in waveguides made from silicon and in waveguides made from chalcogenide glass. The results as well as the used methods are discussed in the following sections, first for silicon and then for chalcogenide waveguides.

### 3.2.1 Silicon Mid-Infrared Photonics

*Related Article[101]:*

*An octave spanning mid-infrared frequency comb generated in a silicon nanophotonic wire waveguide*

*B. Kuyken, T. Ideguchi, S. Holzner, M. Yan, T. W. Hänsch, J. Van Campenhout, P. Verheyen, F. Leo, R. Baets, G. Roelkens, and N. Picqué*

*Contribution: The waveguide described in this section was developed in cooperation with the Ghent University. In charge of the development of the waveguide was Bart Kuyken in the group of Roel Baets and Gunther Roelkens. The calculations as well as the fabrication of the waveguide was done in Ghent. The experiments concerning supercontinuum generation as well as the investigations concerning the coherence of the generated supercontinuum was done at the Max Planck Institut fuer Quantenoptik in Germany. My own contributions are: Setup of the required experimental apparatus for supercontinuum generation and it's characterization as well as the actual generation and characterization of the supercontinuum together with B. Kuyken, T. Ideguchi and M. Yan. Discussion of the manuscript.*

#### Silicon Waveguide Parameters

The used waveguide consists of a rectangular silicon photonic wire sitting on an  $2\ \mu\text{m}$  thick silicon dioxide layer on top of a thick supporting silicon waver as illustrated in Figure 3.6A. Thereby three sides of the silicon wire are cladded by air and one by silicon dioxide. The wire measures 390 times 1600 nanometers in cross section and is 10 mm long. In order to ease in- and out-coupling into the waveguide, it has an adiabatic taper towards the facets, widening the waveguide from 1600 nm to 3000 nm.

Due to the high refractive index contrast between cladding and core material the modal confinement is very strong as indicated for the quasi TE mode shown in Figure 3.6B, where the modal distribution for an in-coupled wavelength of 2400 nm ( $4166\ \text{cm}^{-1}$ ) is shown (calculated using Mode solutions from Lumerical Solutions, Inc.). The strong confinement leads to a strong contribution of the waveguide to the overall dispersive properties of the system and can be engineered by changing the geometry of the waveguide. The dispersion of the system is shown in Figure 3.6C (calculated by Bart Kuyken). The dispersion is crossing zero at a wavelength of 2180 nm ( $4587\ \text{cm}^{-1}$ ). Strong modal

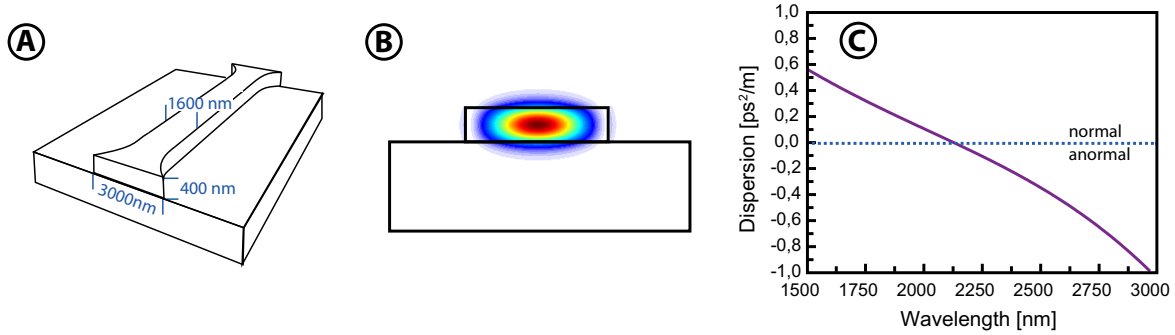


**Figure 3.6:** **A** Sketch of the silicon on insulator ( $\text{SiO}_2$ ) waveguide. **B** Modal distribution in the waveguide for an incoupled wavelength of 2400 nm. **C** Dispersion of the waveguide as a function of the incoupled wavelength.

confinement in combination with the high nonlinear refractive index of silicon lead to a high nonlinear parameter defined as (see e.g. [102]) :

$$\gamma = \frac{2\pi f_0 n_2(f_0)}{c A_{eff}(f_0)} \quad (3.2)$$

with  $f_0$  as the central pump frequency,  $n_2$  as the nonlinear refractive index of the waveguide material and  $A_{eff}$  as the effective mode area. In the case of the very strongly confined mode at 2300 nm ( $4347 \text{ cm}^{-1}$ ) this parameter  $\gamma$  can be as high as  $38(\text{Wm})^{-1}$  as compared to e.g. a highly nonlinear photonic crystal fiber having a nonlinear parameter of  $\gamma \approx 1(\text{Wm})^{-1}$ .

### Silicon Waveguide Supercontinuum Generation Setup

The waveguide is pumped by the optical parametric oscillator described in Section 3.1, tuned to a centre wavelength of 2290 nm ( $4366 \text{ cm}^{-1}$ ), close to the zero dispersion wavelength of the waveguide, delivering pulses of about 70 fs with an average power of 35 mW. The setup used to couple these pulses into the waveguide is depicted in Figure 3.7. For in-coupling and out-coupling to the waveguide short focal length chalcogenide lenses (Thorlabs C037TME, focal length 1,87 mm, numerical aperture  $\text{NA} = 0,85$ ) were used. Because of the bad mode match between free space and waveguide the alignment of the lenses for in- and out-coupling is crucial and thus two picomotor actuated  $x,y,z$  translation stages (Newport 562 Ultralign) were used for the positioning of the lenses in the front and back of the waveguide. Nevertheless, the coupling loss was around -12 dB for each lens which is caused by the already mentioned mode mismatch between the quasi TE mode in the waveguide and the TEM<sub>00</sub> mode in free space. The peak power in the waveguide under this conditions was 225 W. The spectral broadened light can be either sent into a commercial Fourier transform spectrometer (VERTEX70 from Bruker)

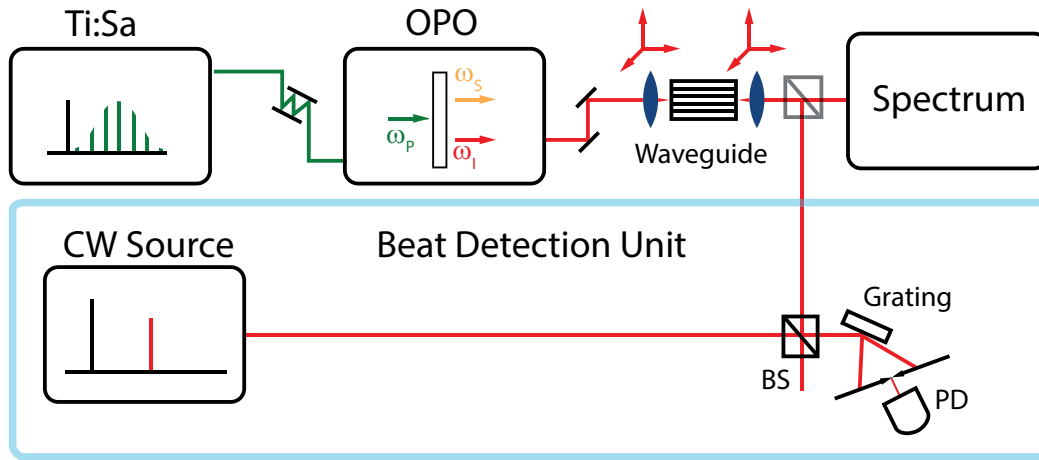


**Figure 3.7:** Experimental setup for supercontinuum generation and characterization. Mid-infrared light generated in the optical parametric oscillator is coupled into the waveguide with high NA chalcogenide lenses. The lenses are mounted on stepper motor actuated  $x,y,z$  stages. Light exiting the waveguide can either be sent into a commercial Fourier transform spectrometer or into a home built beat detection unit. The beat detection unit is comprised of a CW source which is combined with the light under scrutiny on a beam splitter ( $\sim 90$  to  $10$ ). The combined beams are dispersed with a grating, spatially filtered with a slit and finally shined onto a photodetector. The grating in combination with an aperture acts as a spectral filter limiting the incident radiation on the detector to the region of interest.

or into a self built beat detection unit, to measure the coherence properties of the generated supercontinuum. The beat detection unit allows to measure the beat between the broadened light from the waveguide and a CW source which can be either a CW optical parametric oscillator (Argos from Aculight) in combination with an InGaAsSb detector or a free running Er-doped Fiber laser (Koheras from NKT Photonics) in combination with an extended-InGaAs detector.

### Supercontinuum Spectral Characterization

As the main purpose of the experiment was to gain more spectral bandwidth, spectral investigations were done first and, if the generated spectrum was found to be sufficiently broad, the coherence of the spectrum was probed by taking beat notes of the supercontinuum against CW lasers. A supercontinuum generated in the waveguide is shown in Figure 3.8E. The input spectrum, located around  $2290\text{ nm}$  ( $4366\text{ cm}^{-1}$ ) is plotted in blue whereas the generated supercontinuum is shown in red. The light blue bar at the bottom of the graph indicates the  $-30\text{ dB}$  limit measured from the spectral maximum. The supercontinuum spans from  $1540\text{ nm}$  ( $6493\text{ cm}^{-1}$ ) down to  $3200\text{ nm}$  ( $3125\text{ cm}^{-1}$ ), covering 1,055 octaves in the mid-infrared. Between  $3440$  and  $3580\text{ nm}$

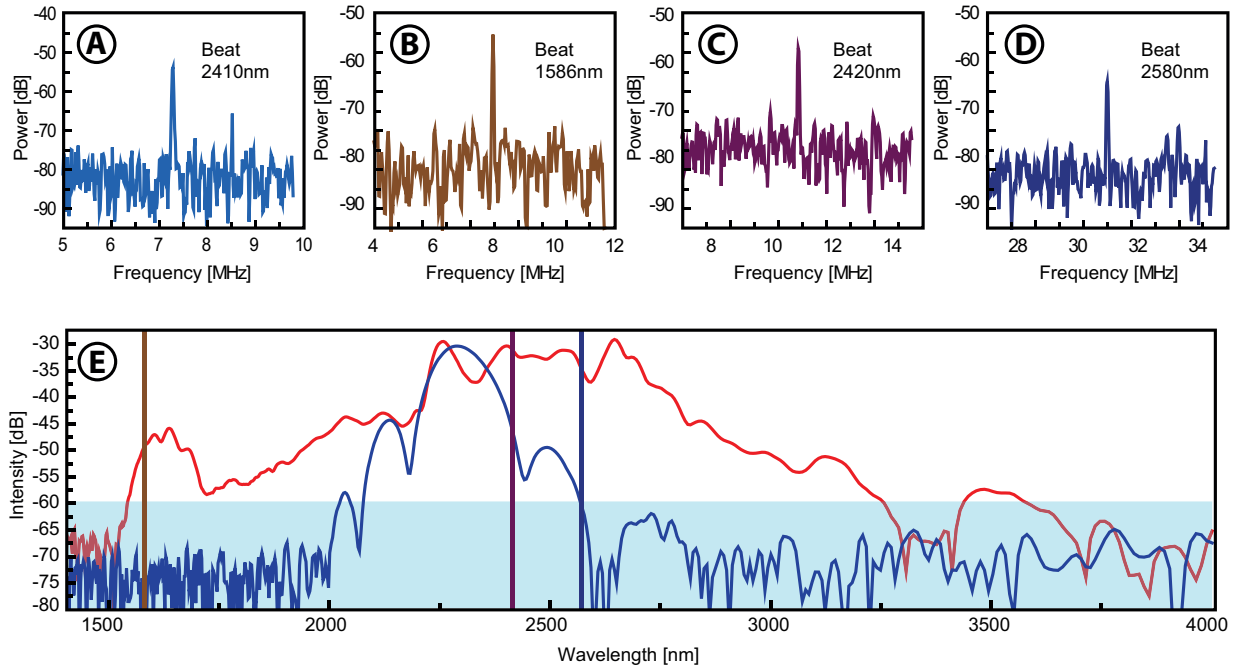


**Figure 3.8:** A to D Beat notes between optical parametric oscillator and supercontinuum with two different CW sources (a CW optical parametric oscillator and a CW fiber laser) E Supercontinuum generated in the waveguide (red) and fundamental light (blue); the light blue bar marks -30 dB from the maximum, the vertical colored lines the position of the corresponding beat notes.

(( $2906\text{ cm}^{-1}$ ) and ( $2793\text{ cm}^{-1}$ )) another peak rises above the -30 dB limit. The peak on the short wavelength end of the spectrum at 1600 nm ( $6250\text{ cm}^{-1}$ ), in the normal dispersive regime of the waveguide, indicates dispersive wave generation which also explains the very sharp cutoff at short wavelength. The main contribution to the central part of the supercontinuum, between -30 and -40 dBm in Figure 3.8E, is assumed to be self phase modulation.

### Supercontinuum Coherence

After gaining such a broadband spectrum the coherence of the spectrum was taken under scrutiny. Soliton dynamics can, under certain circumstances, be very sensitive to noise and thereby the generated spectrum can lose coherence. Generally the faster the higher order soliton evolves the lower the influence of background noise and the better the coherence of the generated spectra. As Figure 3.6 indicates the pump wavelength is in the anomalous dispersive regime of the waveguide, in vicinity to the zero dispersion wavelength. Therefore the in-coupled short pulse forms a higher order soliton in the waveguide. The order can be estimated to be  $\sim 6,3$  and the fission distance to  $\sim 0,74\text{ mm}$  ([103]). Thus indicating a rather fast evolution of the soliton, holding promise for good

coherence properties of the output spectrum.

To investigate the coherence properties of the generated spectra, beat notes are taken between narrow band CW lasers and the supercontinuum generated in the waveguide. To exclude that the coherence of the pump light is already corrupted in the downconversion process of the femtosecond optical parametric oscillator (see Section 3.1), light directly from the femtosecond optical parametric oscillator is guided in a beat detection unit and the beating against a CW optical parametric oscillator (Argos from Aculight) is recorded using a radio frequency spectrum analyzer (FSL 9 kHz to 3 GHz from Rohde und Schwarz). The resolution and video bandwidth of the spectrum analyzer are set to 10 kHz for all beat notes shown. The CW optical parametric oscillator itself has a linewidth of 60 kHz (in 10  $\mu$ s measurement time; from datasheet). Figure 3.8A depicts the recorded beat note of the CW and femtosecond optical parametric oscillator, it shows a beat note having a width of around 80 kHz at -3 dB. The beat note is slightly wider than the line width of the CW optical parametric oscillator, indicating that the linewidth of the femtosecond optical parametric oscillator is on the same order as the CW optical parametric oscillator as the beat note is the convolution of the line-shapes of both lasers. The result is in congruence with other free running laser systems in terms of the linewidth [104]. With the knowledge of the coherence of the input spectrum, the supercontinuum could be characterized. To do so beat notes of the broadened light from the waveguide and the CW optical parametric oscillator are taken at 2420 nm ( $4132 \text{ cm}^{-1}$ ), rather close to the pump wavelength of the waveguide and at 2580 nm ( $3875 \text{ cm}^{-1}$ ), further apart but still comparably close to the pump wavelength of the waveguide. The outcome of those two beat note experiments is plotted in Figure 3.8D and Figure 3.8C in dark blue and purple. Both lines have a width comparable to that of the femtosecond optical parametric oscillator measured before the waveguide, indicating no or only very minor degradation of coherence in the supercontinuum generation process at these wavelengths. Close to the seed wavelength self phase modulation is the dominant broadening effect, which is always coherent and can mask coherence loss due to other effects taking place simultaneously. However, coherence degradation is more severe further away from the pump wavelength. A beat note experiment at a wavelength far away from the pump is hence more sensitive to coherence degradation. Changing to a different CW laser a beat note is recorded at a wavelength not present in the input spectrum, far away from the pump source. This beat note is taken at 1586 nm ( $6305 \text{ cm}^{-1}$ ) using a narrow band CW fiber laser (0,1 kHz linewidth in 100  $\mu$ s measurement time) and is plotted in Figure 3.8B. It also shows a width comparable to the width of the femtosecond optical parametric oscillator itself, indicating no or only very minor coherence degradation even at this wavelength very far away from the pump wavelength of the waveguide.

### 3.2.2 Chalcogenide Glass Mid-Infrared Photonics

*Contribution:* The waveguide described in this section was developed and manufactured in the Australian National University by the group of Barry Luther-Davies. It was brought to the Max Planck Institut fuer Quantenoptik by Bart Kuyken. My own contributions are: Setup of the required experimental apparatus for supercontinuum generation and its characterization as well as the actual generation and characterization of the supercontinuum together with B. Kuyken and M. Yan.

Despite of all the positive aspects of silicon photonics, mid-infrared photonics done in chalcogenide glass has found a huge interest recently, owed to the promises of chalcogenide glass to provide even broader spectra than silicon photonic waveguides. In chalcogenide glasses oxygen is replaced by one of the three other chalcogenides, sulphur, selenium or tellurium. Due to their high atomic mass the corresponding vibrational energies are low and the long wavelength transmission range is significantly extended into the mid-infrared, up to  $11\ \mu\text{m}$  ( $909\ \text{cm}^{-1}$ ) for sulphur, around  $16\ \mu\text{m}$  ( $625\ \text{cm}^{-1}$ ) for selenium and even beyond  $20\ \mu\text{m}$  ( $500\ \text{cm}^{-1}$ ) for tellurium [105, 106, 107, 108]. The chalcogenide elements are covalently bound to network formers such as e.g. Arsenic, Germanium, Gallium or Phosphorus. The relative mixing ratio of these elements can vary within certain borders, allowing to tune the optical properties of the material [109, 110]. This allows for production of waveguides and hence the use of this materials for e.g. supercontinuum generation [111, 112, 113]. The nonlinear refractive index of this material is of the same order as silicon (e.g. [100]) but the linear refractive index ( $\sim 3,4$  for silicon and around 2 for chalcogenide glasses) does not allow a modal confinement as strong as in silicon. Hence the nonlinear parameter  $\gamma$  (see Equation 3.2) is lower for chalcogenide glasses [114, 115, 116]. On the other hand the different linear refractive index of the material demands for a different waveguide geometry which does not allow an as high modal confinement as in silicon. The benefit of a larger mode in the waveguide is easier in- and out-coupling due to a better mode match between the free space and the waveguide mode.

#### Chalcogenide Glass Waveguide Parameters

The waveguide used in this experiment is a ridge waveguide, fabricated out of a  $\text{Ge}_{11,5}\text{As}_{24}\text{Se}_{64,5}$  using a top down process. The waveguide measures  $4\ \mu\text{m}$  in width in the centre and  $46\ \text{mm}$  length, 50 percent of the  $2,5\ \mu\text{m}$  thick  $\text{Ge}_{11,5}\text{As}_{24}\text{S}_{64,5}$  was etched away, to form a  $1,25\ \mu\text{m}$  high ridge on a  $1,25\ \mu\text{m}$  thick  $\text{Ge}_{11,5}\text{As}_{24}\text{S}_{64,5}$  layer (Figure 3.9A). The waveguide has a  $10\ \text{nm}$  overcoat of fluoropolymer, to protect it from the laboratory atmosphere to avoid degradation.

For in and out-coupling of the chalcogenide waveguide the same setup is used as for the silicon waveguide (see Figure 3.7). The femtosecond optical parametric oscillator from Section 3.1 is used to pump the waveguide and chalcogenide lenses mounted on

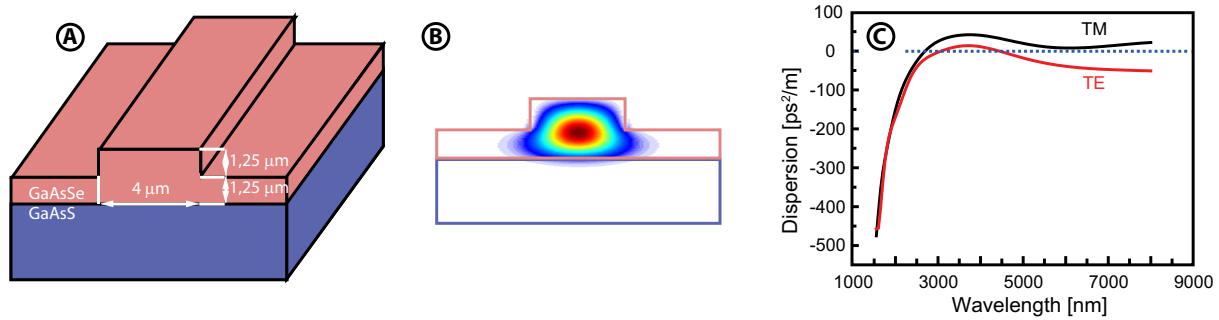


**Figure 3.9:** **A** Sketch of the chalcogenide waveguide. **B** Modal distribution in the waveguide for an incoupled wavelength of 2290 nm **C** Dispersion of the waveguide as a function of incoupled wavelength for TE and TM mode.

picomotor actuated stages for precise alignment are used. One difference to the silicon waveguide experiment is the addition of a half-wave plate into the beam path before the waveguide. As depicted in Figure 3.9B the polarization is tilted by 90 degrees compared to the mode field of the silicon waveguide in Figure 3.6. The field distribution shown in Figure 3.9B is calculated for a centre wavelength of 2290 nm ( $4366 \text{ cm}^{-1}$ ) as used in the experiments.

Figure 3.9C is a plot of the waveguide dispersion for a quasi TE and a quasi TM mode (calculated by the group of Barry Luther-Davies). The fact that quasi TE and quasi TM mode have a slightly different dispersion inside of the waveguide allows to tune the dispersion by rotating the polarization of the incident light and thereby changing the TE and TM contributions to the propagating mode in the waveguide. Figure 3.9C also indicates that the pump wavelength is in the negative dispersive regime of the waveguide. Therefore, a short pulse injected into the waveguide forms a, possibly higher order, soliton and experiences the evolution of this soliton e.g. soliton fission and dispersive wave generation just like in the silicon waveguide. Similarly to the silicon waveguide spectra were taken and the coherence of the outgoing light of the waveguide was tested. The chalcogenide waveguide is longer than the silicon waveguide to account for lower nonlinearity. The soliton evolution inside of the chalcogenide waveguide is slower than in the silicon waveguide due to the lower nonlinearity and therefore the possibility of coherence degradation in the chalcogenide waveguide is higher than in the silicon waveguide.

### Supercontinuum Spectral Characterization

To generate the broadest spectra utilizing the chalcogenide waveguide, the half wave plate is rotated slightly to get a mixture of the TE and TM mode in the waveguide. A spectrum generated in this way is plotted in Figure 3.10A. The central pump wavelength is 2290 nm ( $4366 \text{ cm}^{-1}$ ) and the power delivered by the femtosecond optical parametric

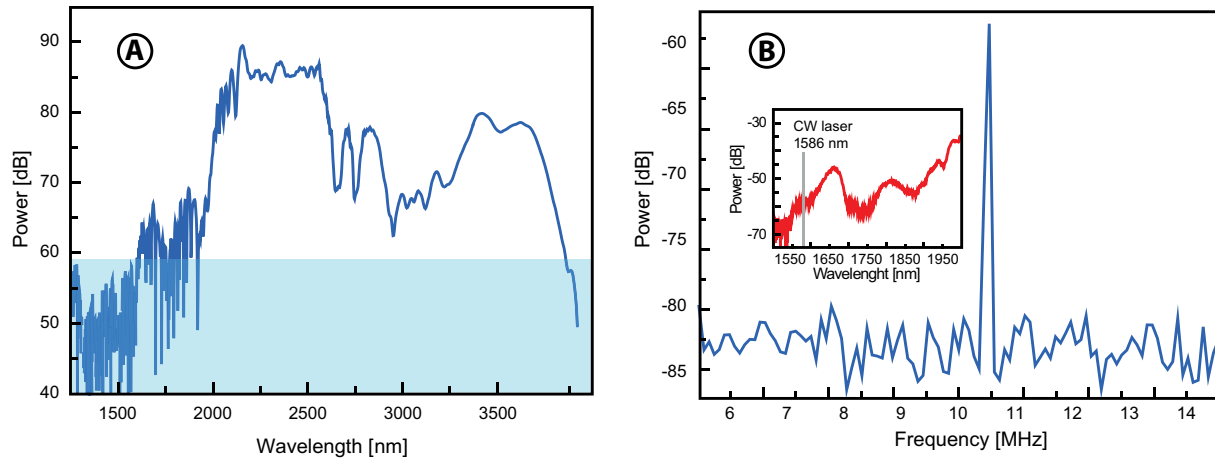


**Figure 3.10:** **A** Supercontinuum generated in the chalcogenide waveguide. The light blue bar marks -30 dB from the maximum. **B** Beat note between the supercontinuum and a CW laser at 1586 nm.

oscillator is 51 mW. The coupling losses for in and out-coupling are about -10 dB in total i.e. -5 dB for each coupling step (in- and out-coupling are assumed to have the same efficiency). The generated spectrum spans from around 1600 nm to 3860 nm ( $(6250\text{ cm}^{-1})$  to  $(2590\text{ cm}^{-1})$ ), which corresponds to 1,27 octaves at a -30 dB level indicated by a light blue bar in figure 3.10. The spectral span is very sensitive to the polarization of the incident light. Therefore, turning the half wave plate has a strong influence on the shape and the spectral coverage of the output spectra.

The long wavelength side of the supercontinuum is moderately modulated which can indicate soliton fission and subsequent soliton self frequency shifting. The short wavelength part of the supercontinuum first falls off sharply in power at around two micrometers which is a sign for dispersive wave generation. After a power decrease of about 20 dB a pedestal forms from 1,6 to 2  $\mu\text{m}$  ( $(6250\text{ cm}^{-1})$  to  $(5000\text{ cm}^{-1})$ ) which is heavily modulated. One possible explanation for this strong modulation can be optical wave breaking, which can generate fine, strongly modulated structures in the spectrum [117, 118, 119].

### Supercontinuum Coherence

Because of the already pointed out fact, that the chances for coherence degradation in the chalcogenide waveguide are higher than in the silicon waveguide, the coherence of the generated supercontinuum was probed by beat detection between the supercontinuum and a free running Er-doped CW Fiber laser (Koheras from NKT Photonics).

Therefore, the generated supercontinuum was coupled into a fiber and overlapped with the CW laser using a fused fiber beamsplitter. The beat of the two fields was detected in a differential detection scheme, using a balanced InGaAs photo detector with fiber

coupled ports to which the output ports of the fused fiber beamsplitter are connected directly. The wavelength of the CW laser is 1586 nm ( $6305\text{ cm}^{-1}$ ), a value where at a centre wavelength of 2290 nm ( $4366\text{ cm}^{-1}$ ) no light is produced in the femtosecond optical parametric oscillator.

As mentioned before using a CW laser with a wavelength far away from the pump wavelength eases detection of coherence degradation, as it tends to be more severe further away from the pump. To improve the signal to noise ratio of the measurement the wave plate in the setup is rotated slightly to increase the signal power in the short wavelength region (see inset of Figure 3.10B, it is recorded with an optical spectrum analyzer (AQ6375 Yokogawa 1200-2400 nm) as it offers much faster refresh times and a larger dynamic range than the Fourier transform spectrometer from Bruker facilitating alignment significantly). The outcome of such a beat detection experiment is depicted in Figure 3.10B, video and resolution bandwidth of the radio frequency spectrum analyzer (FSL 9 kHz to 3 GHz from Rohde und Schwarz) are set to 10 kHz. The plot in Figure 3.10B shows a clearly visible beat note with a width comparable to the beat note measured before coupling into the waveguide (see Figure 3.8A), indicating no or only very minor coherence degradation occurring in the waveguide.

### 3.2.3 Summary Mid-Infrared Photonics

The experiments conducted in order to broaden the spectrum of the femtosecond optical parametric oscillator are summed up here. With both waveguides, made from silicon and from chalcogenide glass, a supercontinuum was generated spanning more than one octave. The supercontinua did not suffer from coherence degradation for the silicon as well as for the chalcogenide waveguide proven by beat detection experiments between narrow band CW lasers and the generated supercontinua. Such supercontinua can therefore be used to conduct coherent spectroscopy in the mid-infrared, such as e.g. dual-comb spectroscopy, covering a huge spectral band despite the limited spectral coverage of the optical parametric oscillator used as pump source for the waveguides. Moreover since the spectra generated span more than one octave, such supercontinua can potentially be used to measure the carrier envelope drift of the supercontinuum itself. Using the right feedback or feed forward technique, this would allow to make a self referenced optical frequency comb out of the supercontinua which is located in the mid-infrared, where such sources can be rarely found.

### 3.3 Mid-Infrared Dual-Comb Spectroscopy

Contribution: Layout and setup of the system as well as experimental work and data analysis.

To employ the femtosecond optical parametric oscillator or the supercontinuum generated in a waveguide for (linear) dual-comb spectroscopy the source has to be, as the name already indicates, a frequency comb. A demand not fulfilled by neither the supercontinuum nor the femtosecond optical parametric oscillator.

One problem encountered is that the carrier envelope frequency of the femtosecond optical parametric oscillator is not determined by the carrier envelope frequency of the pump source solely. The femtosecond optical parametric oscillator is locked tightly to the repetition rate of the Titanium Sapphire laser used as pump source, due to the fact that a parametric process is harnessed and no energy is stored inside of the femtosecond optical parametric oscillators gain medium. However the carrier envelope frequencies of the fields  $E_{signal}$  and  $E_{idler}$  generated in the femtosecond optical parametric oscillator are not determined unambiguously by the carrier envelope frequency of the pump.

Energy conservation demands the sum of the signal frequency  $f_{signal}$  and the idler frequency  $f_{idler}$  to be equal to the pump frequency  $f_{pump}$ :

$$f_{pump} = f_{signal} + f_{idler} \quad (3.3)$$

However, Equation 3.3 does not determine the carrier envelope frequencies of the signal  $f_{ceo\ signal}$  and idler  $f_{ceo\ idler}$ . Using the frequency comb equation (Equation 2.5) and the fact that all fields are generated at the same repetition rate  $f_{rep}$  allows resolving  $f_{pump}$ ,  $f_{signal}$  and  $f_{idler}$ :

$$\begin{aligned} n f_{rep} + f_{ceo\ pump} &= k f_{rep} + f_{ceo\ signal} + l f_{rep} + f_{ceo\ idler} \\ (k + l - n) f_{rep} &= f_{ceo\ pump} - f_{ceo\ signal} - f_{ceo\ idler} \end{aligned} \quad (3.4)$$

Equation 3.4 shows that even for a fully stabilized pump source another degree of freedom is needed to be measured and controlled which can be either the carrier envelope frequency of the signal or idler.

It is possible to avoid the need for stabilization of the pump source - optical parametric oscillator system by using an adaptive sampling scheme (see Section 2.2.3). This approach faces the problem, that in the mid-infrared narrow band lasers, needed to generate a reference signal for adaptive sampling, are hardly available. The fact that the femtosecond optical parametric oscillator is a singly resonant system offers the possibility

to take the reference signal at the pump source wavelength, making use of the fact how fluctuations of the pump source are transferred to the signal and idler.

The line width of signal  $\Delta f_s$  and idler  $\Delta f_i$  is given by [120, 121, 122]:

$$\Delta f_{s,i} = \frac{\kappa_{s,i}^2}{(\kappa_s + \kappa_i)^2} \Delta f_{pump} + \frac{\hbar\omega_{s,i}}{P_{s,i}} \frac{(\kappa_s \kappa_i)^2}{(\kappa_s + \kappa_i)^2} (\bar{n}_s + \bar{n}_i + 1) \quad (3.5)$$

with the line width of the pump source  $\Delta f_{pump}$ , the (cold) cavity round trip dissipation constants for signal and idler  $\kappa_{s,i}$ , the average thermal photon number  $\bar{n}_{s,i}$  and the output power of signal and idler  $P_{s,i}$ . The first term on the right side of Equation 3.5 is the contribution of the pump source to the line width of the optical parametric oscillator, the second term is a line broadening effect due to a quantum mechanical phase diffusion between signal and idler. The second term is usually small compared to the first term, especially when the pump source is free running, and Equation 3.5 can be approximated:

$$\Delta f_{s,i} \approx \frac{\kappa_{s,i}^2}{(\kappa_s + \kappa_i)^2} \Delta f_{pump} \quad (3.6)$$

The system described in Section 3.1 is singly resonant for the signal, which means that the cavity round trip dissipation constant of the signal  $\kappa_s$  is very small and the cavity round trip dissipation constant of the idler  $\kappa_i$  is very large as the mirrors of the optical parametric oscillator are highly reflecting for the signal (more than 99 percent reflectivity) and are highly transparent for the idler (more than 80 percent transmittance). This gives rise to the assumption that pump fluctuations are nearly entirely passed to the idler.

### Experimental Implementation

The reference signals for adaptive sampling are generated by beat note detection between pump light and a narrow band CW laser. In order to generate these signals, pump light is guided out of the optical parametric oscillator cavity after it passed through the gain medium and the out-coupling mirror of the optical parametric oscillator. The experimental setup is outlined in Figure 3.11. The remaining pump light is guided out of the optical parametric oscillator cavity and sent into two different beat detection units for both optical parametric oscillators. In one of the beat detection units an Erbium doped fiber laser (Koheras from NKT Photonics) lasing at 1586 nm which is frequency doubled to 793 nm in a frequency doubling waveguide (from NTT electronics) serves as reference. In the other, a home built ultra stable CW diode laser locked to an optical cavity, lasing at 830 nm (developed by D.C. Yost) is used.

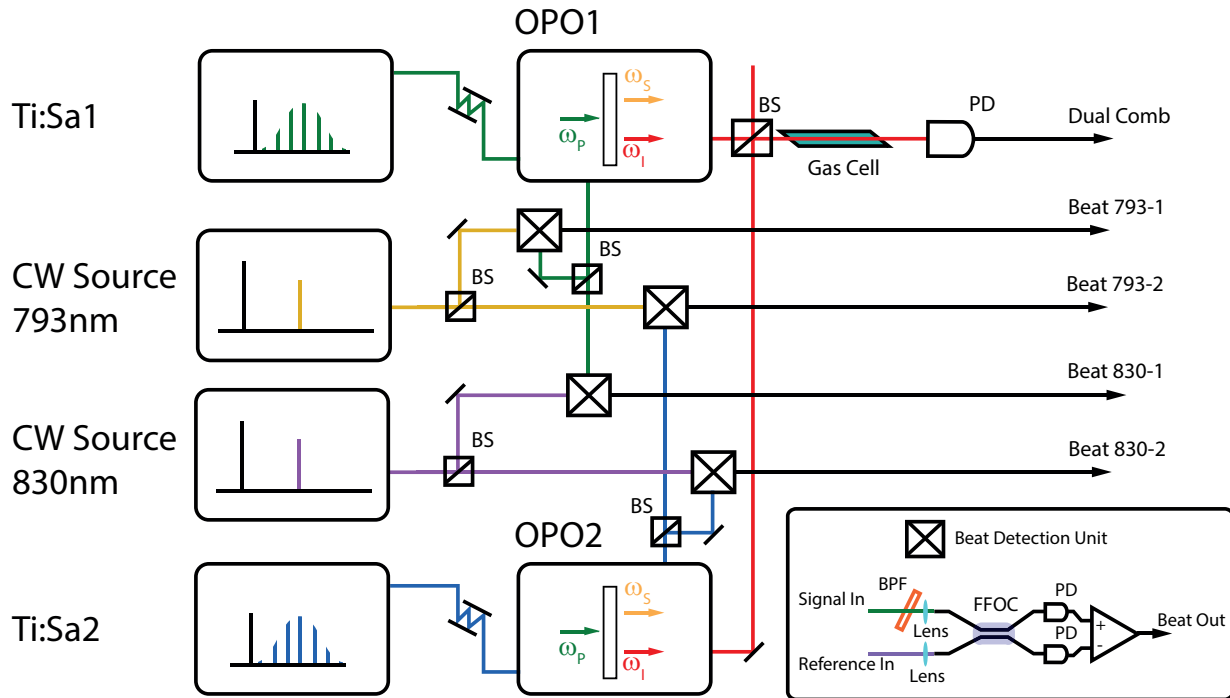


**Figure 3.11:** Experimental setup of a dual-comb mid-infrared absorption experiment with adaptive sampling. The output of the two optical parametric oscillators is combined on a beam splitter (BS) and send through a gas cell filled with acetylene. Remaining pump light is guided out of the optical parametric oscillators and send into beat detection units to generate correction signals for adaptive sampling. For each optical parametric oscillator, two correction signals are generated against two different CW sources. The inset depicts the beat detection units in detail. Remaining pump light and the reference light are coupled into a fused fiber optic coupler (FFOC) using a lens. The pump light is band pass filtered (BPF) before in-coupling to minimize generated noise. The output of the FFOC is send into a fiber coupled differential detector.

The actual dual-comb experiment is an absorption experiment using a 700 mm long gas cell filled with acetylene at  $\sim 1,6$  Torr. To record spectra, the optical parametric oscillator is tuned to a central idler wavelength of 2350 nm ( $4255 \text{ cm}^{-1}$ ).

The signal of the photodetector after the gas cell and the signals of the beat detection units are all sent into an electrical signal path which provides filtering and, when necessary, amplification and mixing of the signals. After being manipulated accordingly the signals are digitized with a commercial digitizer card (AlazarTech). The signal path for the beat note signals as well as the dual-comb signal is depicted in Figure 3.12.

The signals from the beat detection units (Beat 793-1,2 and Beat 830-1,2 in Figure 3.11 and Figure 3.12) are fed in a chain of low pass and notch filters in order to isolate a beat signal between CW laser and the closest comb mode of a pulsed laser. It is located in

the band from 0 to 50 MHz. At certain points a part of the signal is tapped off, either for signal monitoring (using a -10 dB coupler and a spectrum analyser) or to feed it into a stabilization scheme (using a -3 dB splitter) for the pump laser. Due to the fact that stabilizing a frequency comb against two optical references is problematic ([123, 124, 125], only one of the beat note signals of a Titanium Sapphire lasers is stabilized against a radio frequency reference. The stabilized beat note, is the beat note against the frequency doubled CW fiber laser at 793 nm (Beat 793-1,2 in Figure 3.12). The signal is tapped off with a -3 dB splitter and fed into a digital phase comparator, a frequency divider and finally into a proportional integral controller to control a piezo actuator inside of the Titanium Sapphire lasers cavity.

Two beat notes against the same CW laser but from different Titanium Sapphire lasers are mixed (Beat 793-1,2 and Beat 830-1,2 are receptively mixed) to reveal the relative fluctuations between the respective comb modes of the two different lasers (see Section 2.2.3). In order to bring the signals to the right level for the mixer one of them has to be amplified to 7 dBm before mixing.

Group delay variation(s) in the signal path leads to incorrect results when the adaptive correction is carried out. Therefore the signal path is designed to have a group delay similar for all signals. To assure a flat group delay over the frequency range from 1 to 50 MHz, bandpass filters are avoided when possible, as bandpass filters introduce high group delay which can be strongly modulated depending on the filter function (e.g. elliptic or Chebyshev etc.). To examine the group delay of the signal paths as a function of frequency, a simulation is set up using Genesys (Keysight). The group delay is simulated from the input port to the mixer. The path with and without an amplifier is calculated and overlaid in the inset of Figure 3.12. The group delay variation is optimized for maximal flatness over the band from 1 to 30 MHz by choice of components. For the range from 1 to 30 MHz, the minimal group delay is around 33 ns and the maximal is around 46 ns, comparably close for a coverage of nearly one and a half decades. A better group delay match can be achieved if custom designed filtering or an equalization network is employed. Nevertheless, the group delay mismatch is usually only some nanoseconds for an input frequency in the range of 1 MHz to 30 MHz and maximal 13 ns. In this range of group delay mismatch the effects of an adaptive correction should be clearly visible.

To verify the results of the simulation, the group delay is measured at 20 MHz for a signal path with and at 30 MHz for a signal path without an amplifier, using an aperture of 0,1 MHz. The group delay is determined to be 44,4 ns for the 20 MHz signal path and 42,4 ns for the 30 MHz signal path, which fits the calculated values of 44 ns and 43,5 ns for the 20 MHz and 30 MHz paths respectively very well.

The signal path of the beat notes against the 793 nm CW laser (Beat 793-1,2 in Figure 3.12) has very defined frequencies appearing, since Beat 793-1 and Beat 793-2 are stabilized against a radio frequency reference at  $\sim 20$  MHz and  $\sim 30$  MHz. Therefore a bandpass filter can be used after the mixer to isolate the mixed reference signal for adaptive

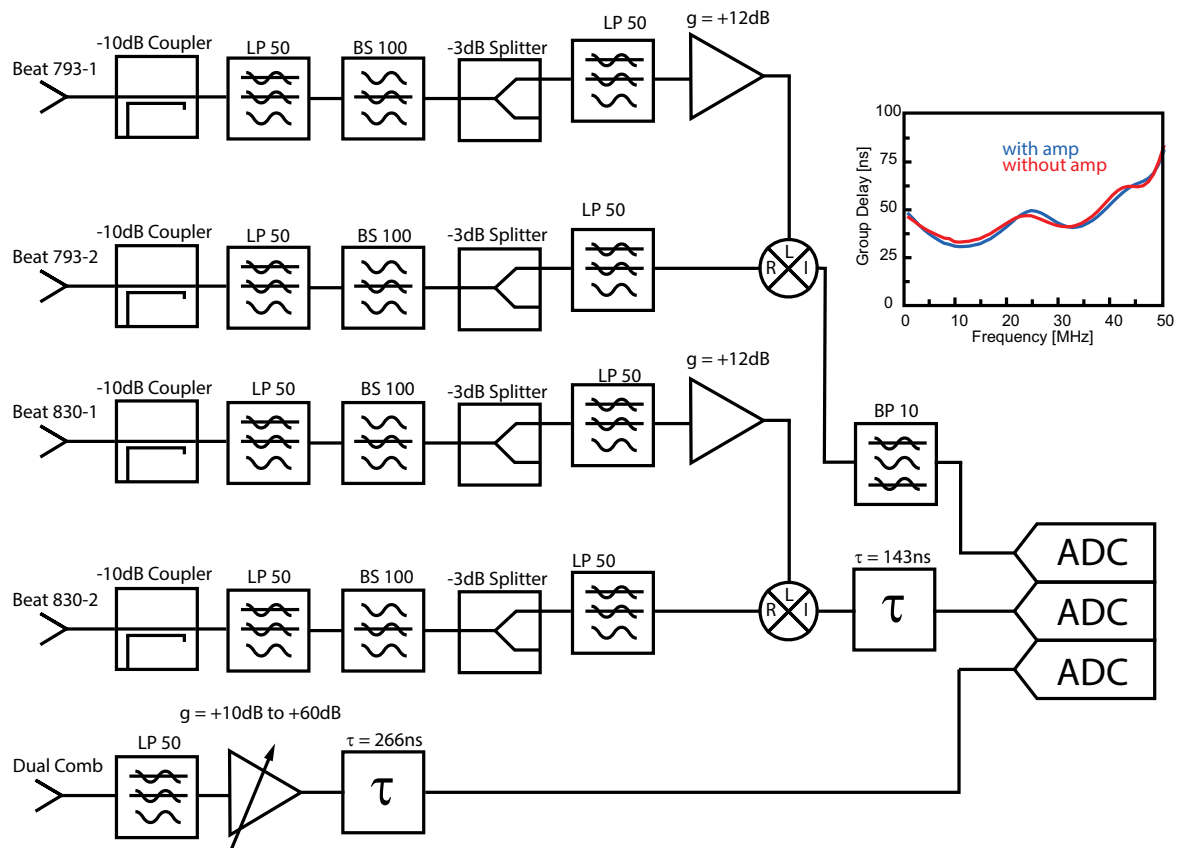


**Figure 3.12:** Adaptive sampling electric signal paths for the dual-comb as well as the adaptive signals. The correction signals are sent through a low pass (LP) and band stop filter (BS) to isolate a single beat note. At certain points signals can be tapped off via -10 dB couplers or -3 dB Splitters for signal monitoring and/or stabilization. Finally two signal paths of two different sources (e.g. 793-1 and 793-2) are combined in a mixer. One of the signals has to be amplified before mixing to ensure proper operation of the mixer. Care is taken adjusting the group delay of all signal paths to the same value, which is done by choice of components and time delay elements. The inset shows the group delay of the adaptive paths with and without amplifier as a function of frequency.

sampling.

In the signal path for the beat notes against the 830 nm CW laser (Beat 830-1,2 in Figure 3.12) this is not the case. The frequencies appearing after the mixer are not stable and drift in frequency over time. As all signal paths must have the same group delay, a frequency independent time delay is introduced after the mixer and signal filtering is done using software. For the 830 nm signal path, all appearing signals have to be lower in frequency than 30 MHz in order to avoid too strong group delay differences between the signal paths and attenuation due to the delay generator (Allen Avionics Pulse and Video delay line V255Z050).

The signal path of the dual-comb signal contains only a low pass filter, a variable gain amplifier and a frequency independent time delay for group delay matching. After mixing, the adaptive signals and the dual-comb signal are digitized.

### Adaptive Corrected Results

The adaptive correction is done entirely in software. The software follows the outline given in Section 2.2.3. Before correction or Fourier transformation of any of the recorded signals, all of them are converted into analytical signals by combining the recorded signal with its Hilbert transformed as explained in Equation 2.2. The analytical dual-comb signal is, in the first step, multiplied with the normalized complex conjugated reference signal gained from the 793 nm CW laser. In a second step, the dual-comb signal is interpolated on a new time axis using the phase information extracted from the 830 nm reference signal. After correction, the dual-comb signal is Fourier transformed without application of a windowing function.

To verify that the adaptive correction scheme is set up properly, light of the Titanium Sapphire lasers is tapped out of the setup, before sending it into the beat detection units. Using this light, an absorption experiment is done with Rubidium. Therefore the tapped out light is sent through a 100 mm long Rubidium cell at 55 degrees Celsius. Figure 3.13A depicts the uncorrected and Figure 3.13B the corrected spectrum, both show the whole spectrum and a zoom into the D1 lines of Rubidium with a resolution of 795 MHz. In the uncorrected spectrum no absorption lines are visible, on the other hand, in the corrected spectrum clear strong absorption lines are visible. Indicating that the adaptive sampling scheme is set up properly and that the instrumental error is small enough to see a clear effect of the adaptive correction.

The Fourier transformed corrected signal, of the acetylene absorption experiment is shown in Figure 3.14 at a resolution of 795 MHz. Despite the adaptive correction the spectrum shows clear indications of phase errors. Several reasons seem possible why the adaptive sampling does not provide good correction under these conditions. One of them is that assumptions about noise, so far, did not include the fact that the optical parametric oscillator itself introduces noise. As an instrumental error as main source of spectral

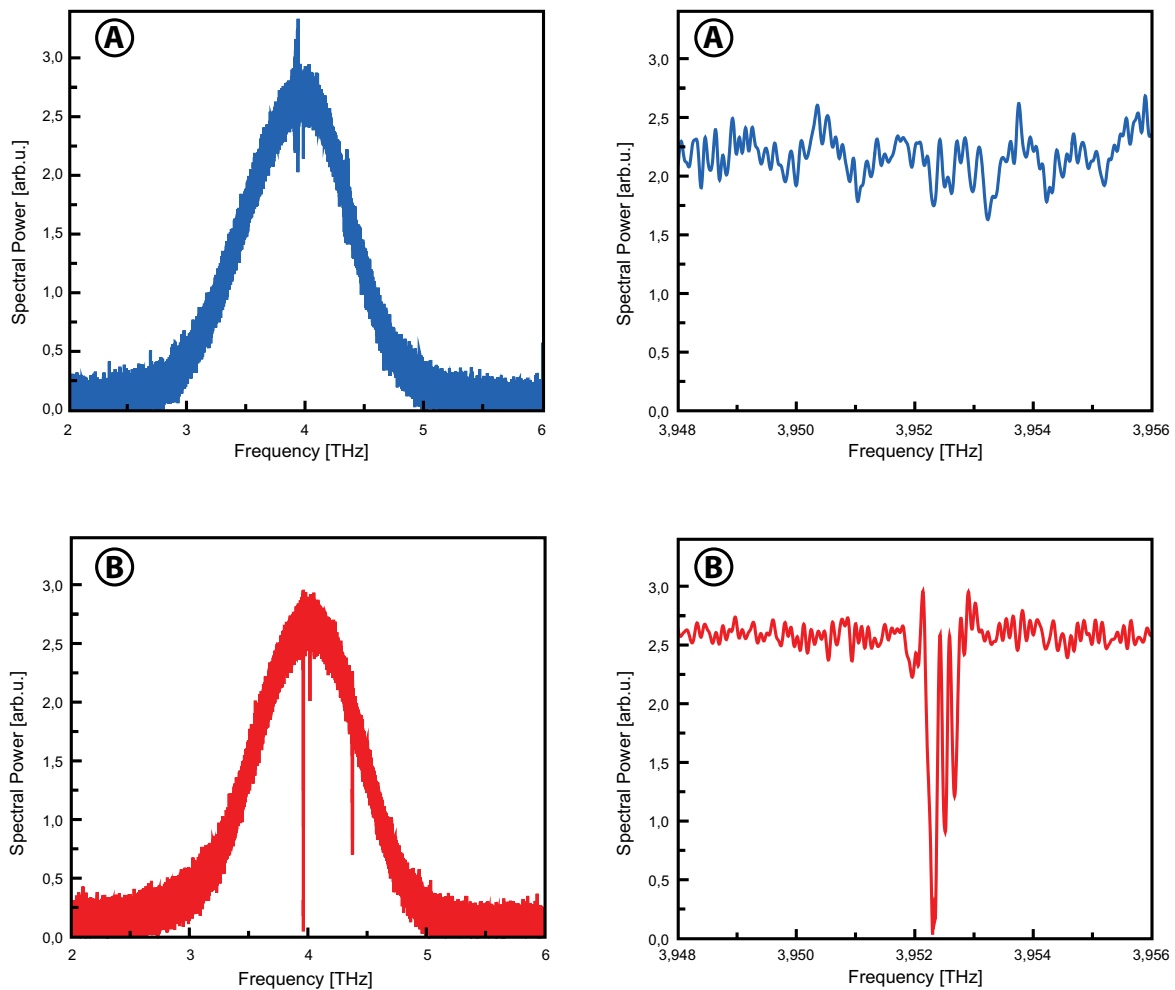


**Figure 3.13:** Uncorrected (A) and corrected (B) Rubidium absorption spectra and a zoom in the D1 lines of Rubidium. As the carrier envelope frequency difference between the two optical parametric oscillators is unknown an absolute frequency scale can not be assigned. The frequency scale corresponds to the radio frequency scale times the inverse of the downconversion factor.

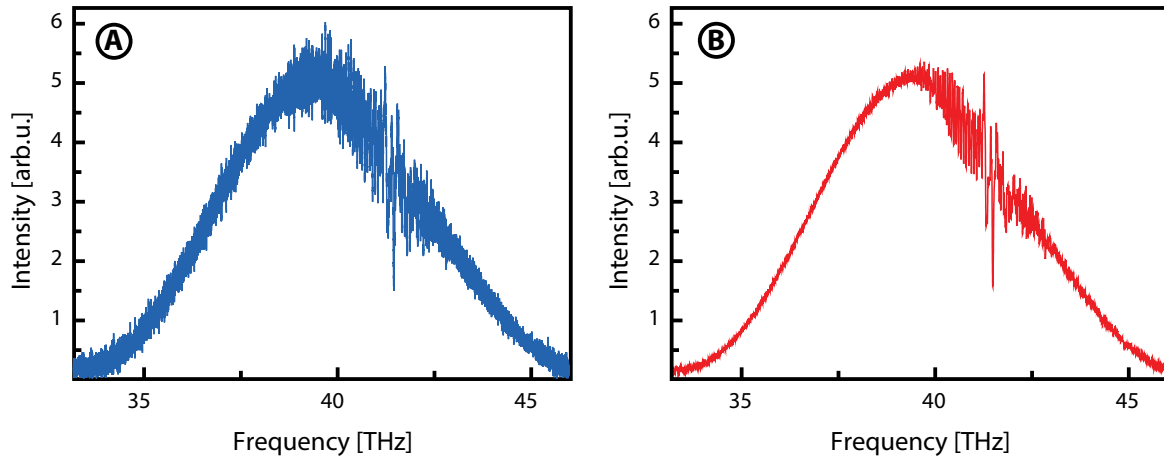


**Figure 3.14:** Dual-comb spectrum of acetylene with adaptive correction at a resolution of 795 MHz. As the carrier envelope frequency difference between the two optical parametric oscillators is unknown an absolute frequency scale can not be assigned. The frequency scale corresponds to the radio frequency scale times the inverse of the downconversion factor. **A** the spectrum after correction. **B** the spectrum after correction smoothed with a Savitzky-Golay filter to suppress excessive noise (3rd order polynomial and 40 side points have been used for filtering).

distortions is ruled out by the Rubidium absorption experiment, fluctuations of the mid-infrared optical parametric oscillator seem to be the most appropriate explanation for spectral errors. Hence an adaptive correction based on the fluctuations of the pump source is not sufficient.

### Summary Mid-Infrared Dual-Comb Spectroscopy

Summarizing what has been achieved so far: an adaptive correction scheme is implemented for a mid-infrared absorption experiment and the correction is employed. The adaptive correction scheme is designed to monitor fluctuations of the pump source and correct them accordingly. No sufficient correction of the mid-infrared spectra can be achieved. To rule out mistakes in the design of the adaptive scheme as primary source of spectral distortions, absorption spectra are measured directly at the pump wavelength and the adaptive correction is employed, improving the spectra significantly. This suggests that the optical parametric oscillator itself introduces additional fluctuations which can not be corrected with this setup. To solve this problem, several ways seem possible. The most straight forward is improving the passive stability of the optical parametric oscillator. Another possibility is to use a supercontinuum similar to the ones generated in the silicon and chalcogenide waveguides in Section 3.2 and employ a common technique to stabilize the drift of the optical parametric oscillator. This could be, for example, a carrier envelope frequency measurement in a  $f$  to  $2f$  or  $f$  to zero scheme in combination

with a stabilized pump source. So far the power of the generated supercontinuum is low, especially for the silicon waveguide, making it difficult to be used in such a stabilization scheme. The high losses of the waveguides are mainly attributed to the low coupling efficiency, which could be increased using mode-matching optics or a specially structured waveguide facet [126, 127]. Finally by reducing the resolution the amount of spectral distortion is reduced, this suggests experiments in the liquid phase as for example total attenuated reflection or vibrational circular dichroism.

## Chapter 4

# Coherent Raman Spectroscopy

The advent of optical microscopy opened the gate to the world on the cellular level. It unveiled fundamental processes and concepts underlying every living being. The discovery of cells, bacteria etc. allowed gaining a solid understanding of vital functions, diseases and their cures. Intense effort has been devoted, pushing further the limits of this technique. Today superresolution, resolution beyond the Abbe diffraction limit, and single molecule sensitivity can be achieved [128, 129, 130, 131]. Nevertheless a lot of microscopy techniques suffer from a common problem: the taken images provide information about absorption or refractive index contrast but generally do not provide information about chemical composition of the sample under scrutiny. This problem can be circumvented by certain techniques as, for example, vibrational spectro-microscopy or staining of the sample with a dye, responding to the effect under scrutiny. Membrane intercalating dyes indicate potential changes in the membrane of different cells or even cell organelles [132, 133] whereas certain dyes react to concentration changes of specific entities in the the cytosol (e.g. dyes chelating certain ions and thereby changing their fluorescent properties as used in calcium imaging [134, 135, 136]). The most prominent example are most likely Sulfonamide dyes, used to stain cells or bacteria for microscopy. They proved to be the first chemotherapeutic substances against bacterial infection, exhibiting a bacteriostatic effect by inhibiting folic acid synthesis in bacteria. This discovery lead to the awarding of a Nobel prize[137] but also illustrates impressively the problems associated with staining. The dyes in use interact with the sample, changing the processes in the sample and, in the most extreme case, lead to cellular necrosis. Additionally these dyes are highly specific to certain effects (v.s.) which is generally considered a very positive property of these dyes. However on the other hand new dyes have to be laboriously developed for new investigations.

Vibrational spectro-microscopy offers a solution to gain chemical information without the need for external staining. It harnesses the intrinsic chemical specificity of vibrational transitions. Different molecular building blocks have different vibrational transitions, which are highly specific in transition energy. The direct way of using infrared light to

examine the sample under scrutiny seems to be straightforward at first but proves to be complicated on closer examination. Infrared light can not be focused down to a small focal spot due to the large wavelength, limiting the spatial resolution. However, a high spatial resolution is one of the key parameters of a microscope. Cell organelles are of micrometer scale, too small to be imaged with long wavelength light using conventional techniques. Another encountered problem are the strong absorption bands of water in the infrared, making microscopy in this region not feasible, since, ordinarily, samples are suspended in either water or a buffered solution containing water as the major component.

A way to enter the field of molecular vibrations, circumventing the need for infrared light, is Raman scattering. Despite the striking key points of Raman scattering - access to fundamental vibrational bands without mid-infrared light - it has the problem of being a notoriously weak effect [138]. The low cross-sections demand either a high power or a long measurement time. Both are quite undesirable parameters for a microscope, because either way the sample is turned into charcoal or has to hold still for a long time. Changing from spontaneous Raman scattering to a stimulated and/or coherent Raman process can solve this problem: coherent Raman scattering is orders of magnitude more efficient than spontaneous Raman scattering, yields a collimated laser like beam, can be used in 3D sectioning due to the nonlinear nature of the effect and, finally, the anti-Stokes light generated is blue shifted compared to the pump wavelength eliminating problems of a sample fluorescence background. Often applied techniques however, suffer from the problem of broad coverage of Raman transitions and fast measurement being mutually exclusive. Generally if the measurement is fast, which can be as fast as image acquisition at video rate, it only allows for a very small coverage of Raman transitions, often only a single transition [139, 140, 141]. Broad spectral coverage on the other hand comes at the price of long measurement times [142]. The techniques presented in the following sections overcome this hurdle and provide fast broadband measurements of Raman transitions.

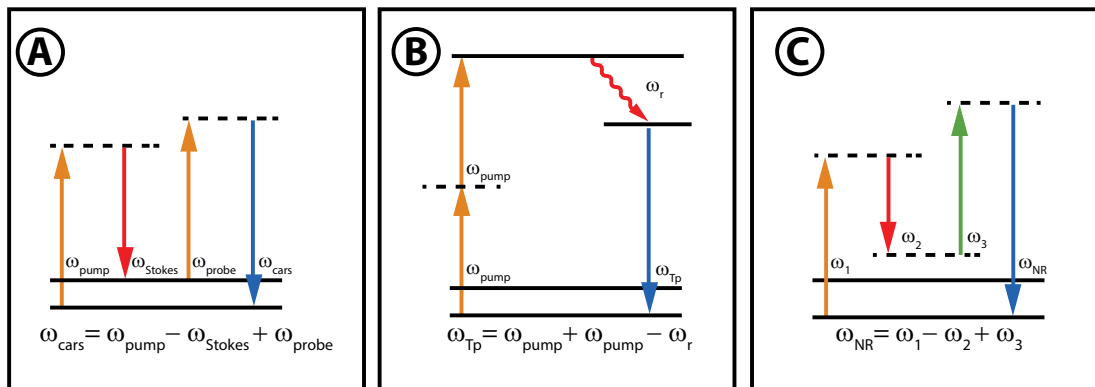


**Figure 4.1:** Possible energy schemes for resonant and non resonant four wave mixing. **A** Resonant CARS **B** Resonant two photon absorption **C** One possible non resonant four wave mixing process.

## 4.1 Coherent Raman Scattering Theory

Raman scattering can generate red or blue shifted light called Stokes and anti-Stokes shifted light respectively. Stokes and anti-Stokes light can be generated by a coherent process, termed Coherent anti-Stokes Raman scattering CARS and Coherent Stokes Raman scattering CSRS. Generally CARS is preferred as it is blue shifted compared to the pump light avoiding (one photon) fluorescence. The following statements focus on CARS but can generally be applied to CSRS with only minor changes. Subsequently a short introduction into the theory of CARS is given. It follows the usual nonlinear polarization approach adapted to a dual-comb experiment.

Coherent Raman scattering is a special light matter interaction. The response of the irradiated matter includes, but is not limited to, information about fundamental vibrational transitions. CARS is a four wave mixing process (third order intermodulation). In this process three ingoing fields, oscillating at  $\omega_{\text{pump}}$ ,  $\omega_{\text{Stokes}}$  and  $\omega_{\text{probe}}$ , are coupled and generate a new field at a different frequency, oscillating at  $\omega_{\text{cars}} = \omega_{\text{pump}} - \omega_{\text{Stokes}} + \omega_{\text{probe}}$  (see Figure 4.1A). If the difference in energy between two incident fields ( $\omega_{\text{pump}}$ ,  $\omega_{\text{Stokes}}$ ) matches a fundamental vibrational transition, a coherent resonant excitation of this vibrational transition is possible. The phase of the (individual) molecular oscillations is correlated by virtue of the coherent excitation. The interaction of the third field oscillating at  $\omega_{\text{probe}}$  with this coherently excited molecules probes the molecular oscillations and yields a laser like beam of light which has been up converted in frequency by the energy of the molecular oscillation. The energy scheme is plotted in Figure 4.1A. The two steps, generation of a coherent population in a vibrational level and production of blue shifted light do not need to happen at the same time. They can be separated by a time  $\tau$  as long as  $\tau$  is shorter than the states decay time.

When matter is subjected to a light field a polarization in the material is induced. If the

light intensity is small enough, it can be modelled by an expansion of the polarization in a power series of the incident field(s) (e.g.[143]):

$$P = \epsilon_0(\chi^{(1)}E_1 + \chi^{(2)}E_1E_2 + \chi^{(3)}E_1E_2E_3 \dots) \quad (4.1)$$

In CARS, three incident light fields are coupled by the third order non linear tensor  $\chi^{(3)}$ , which is the suitable response function of the material to the incident light:

$$P \propto \chi^{(3)}E_{pump}E_{Stokes}E_{probe} = \chi^{(3)}E_{pump}E_{pump}E_{probe} \quad (4.2)$$

The very right of Equation 4.2 corresponds to the case that pump and Stokes are part of the same ingoing field, as it can be the case when a broad band pulse is used. This polarization acts as the source term of the CARS radiation. The nonlinear tensor  $\chi^{(3)}$  not only contains elements responsible for CARS generation, but also all other third order processes, such as two photon absorption or third harmonic generation. It contains resonant and nonresonant contributions and can be expressed as [144]:

$$\begin{aligned} \chi^{(3)}(\omega_{pump}, \omega_{Stokes}) = & \frac{A_{Raman}}{\Omega - (\omega_{pump} - \omega_{Stokes} - i\Gamma_{Raman})} \\ & + \frac{A_{Tp}}{\omega_{Tp} - 2\omega_{pump} - i\Gamma_{Tp}} \\ & + \chi_{NR} \end{aligned} \quad (4.3)$$

$\Omega$  represents the Raman transition frequency,  $\omega_{Tp}$  the two photon absorption transition frequency, the  $\Gamma_i$  are the damping parameters and  $A_i$  the transition strengths. The first term describes the resonant Raman scattering, the second the resonant two photon absorption, both can be subsumed as the resonant contributions of  $\chi^{(3)}$  and are termed  $\chi_R^{(3)}$  in the following. The last term  $\chi_{NR}$  accounts for all non resonant contributions (corresponding energy schemes are plotted in Figure 4.1). For the nonresonant contributions multiple combinations and outcomes are possible, in Figure 4.1C one possibility is picked. In the following two photon absorption is not further considered. Then,  $\chi_R^{(3)}$  contains only the coherent Raman scattering tensor elements. Nonresonant contributions  $\chi_{NR}^{(3)}$  of  $\chi^{(3)}$  are generally a problem when detecting CARS, as they cover a wide spectral bandwidth but do not contain desired information. Considerable effort has been devoted in developing schemes eliminating the influence of  $\chi_{NR}^{(3)}$  on the Raman spectra [145, 146, 147, 148, 149]. The nonresonant contribution is spectrally very broadband and, as no real levels are involved, instantaneous on the time-scales experienced in the course of this thesis. The resonant contributions on the other hand are fixed to given Raman resonances and have a significant lifetime (picoseconds in the case of a liquid for

example). This allows to separate Raman and nonresonant signal temporally (e.g. [150]), which is also harnessed in the experiments conducted in this thesis.

As the conversion efficiency is low and the interaction length is generally short in the case of tightly focused beams (i.e. no depletion of the incident beams), the induced polarization can be separated into a nonresonant and a resonant part and treated perturbatively (see e.g. [151, 152, 153]):

$$\begin{aligned}
 P &= P_R + P_{NR} \\
 P_R &\propto \int_0^\infty d\Omega \chi_R(\Omega) E_{probe}(\omega - \Omega) A(\Omega) \\
 P_{NR} &\propto \int_0^\infty d\Omega \chi_{NR}(\Omega) E_{probe}(\omega - \Omega) A(\Omega) \\
 A(\Omega) &= \int_0^\infty d\omega E_{pump}^*(\omega) E_{Stokes}(\Omega + \omega) \tag{4.4}
 \end{aligned}$$

$A(\Omega)$  is the probability to coherently generate excitation of the level with energy spacing  $\hbar\Omega$  from ground state, which is the sum of all possible two photon combinations between pump and Stokes field ending up in this level. It is the correlation function between the pump field and the Stokes field.

It indicates that, either the difference between pump and Stokes has to match exactly the transition energy or that at least one of them has to be broadband, as otherwise no overlap is given and the correlation yields zero values. An additional effect which has to be taken into account in a real experiment is spectral filtering, which is necessary to isolate the CARS radiation from the fundamental light. It is shortly discussed in Section 4.2.

Equation 4.4 also indicates that a given pulse envelope with given bandwidth favours some Raman transitions more than others, namely transitions with a small transition frequency  $\Omega$  are preferred and transitions with a large transition frequency  $\Omega$  are attenuated. The larger  $\Omega$  gets the smaller the overlap is, limiting the maximally covered band of Raman transitions in the experiment. Therefore the bandwidth of the pump and Stokes fields limit the spectral coverage of the Raman transitions. It also has a strong influence on the signal intensity for a given Raman transition. Figure 4.2 illustrates this fact, it plots  $A(\Omega)$  for Gaussian pulses of different spectral bandwidths normalized to unity and also  $|\chi_{Raman}|^2$  for toluene overlaid with  $A(\Omega)$ .  $A(\Omega)$ , corresponding to a pulse with the smallest spectral span (10 nm), is effectively zero at the wave numbers of the Raman transitions (from approx.  $500 \text{ cm}^{-1}$  to  $1000 \text{ cm}^{-1}$ ). Therefore, no excitation can occur with such a pulse. For a bandwidth of 30 nm,  $A(\Omega)$  is non zero and an excitation of the line at  $\sim 1000 \text{ cm}^{-1}$  can occur. A broader bandwidth of the pulse leads to a larger excitation probability, which is proportional to  $\chi_{Raman} A(\Omega)$ . The pulse with the largest bandwidth (90 nm) maximizes this product.

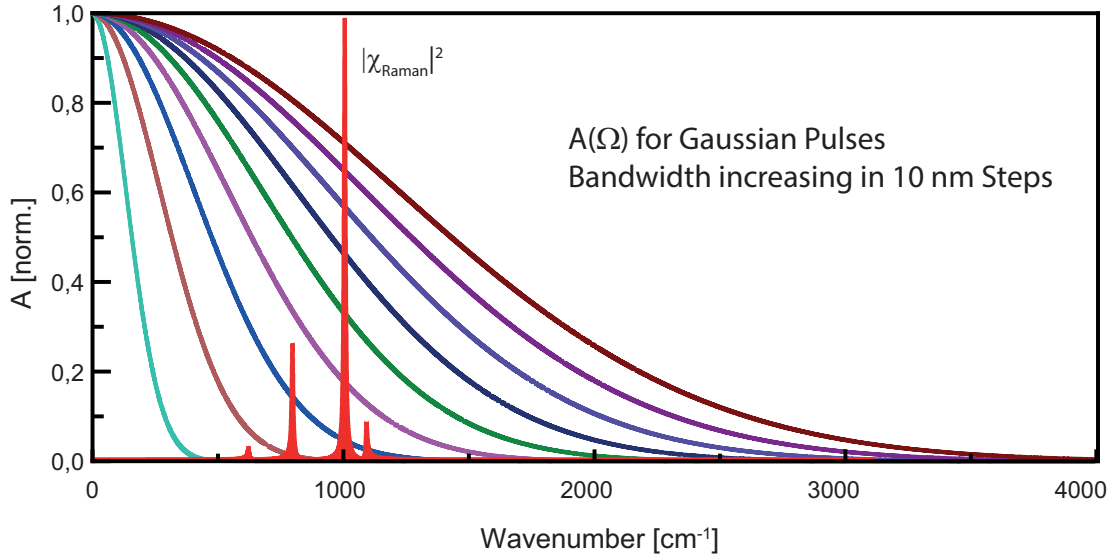


**Figure 4.2:**  $A(\Omega)$  (in wavenumbers  $\nu$ ,  $\nu = f * 100/c$  with  $c$  as the speed of light) calculated for Gaussian pulses centered at 793 nm. The spectral bandwidth FWHM of the pulses increases in 10 nm steps from 10 to 90 nm.  $\chi_{Raman}$  was calculated for toluene using Equation 4.3 and known parameters such as linewidth, relative line strength and line position taken from literature [154].

In dual-comb CARS spectroscopy two separate pulsed laser sources are used to generate CARS radiation. Both lasers have a slightly different repetition rate, leading to a varying time delay  $\tau$  between pump and probe pulse produced by the two lasers. The three ingoing fields  $E_{pump}$ ,  $E_{Stokes}$  and  $E_{probe}$  are contained in the two ultra-short pulses of a single pulse pair produced by the two lasers.  $E_{pump}$  and  $E_{Stokes}$  shall be part of the first pulse and will only be called  $E_{pump}$  from now on. The field  $E_{probe}$  describes the second pulse. Coming back to Equation 4.4, transitioning to the time domain allows to rewrite the convolution into a simple multiplication and, if taken into account that  $E_{probe}$  arrives after  $E_{pump}$ , separated by the time delay  $\tau$ , it can be written as:

$$P_R(t, \tau) \propto E_{probe}(t - \tau) * \mathcal{F}(\chi(\Omega) * A(\Omega))(t) \quad (4.5)$$

This corresponds to the polarization generated by two pulses separated by time  $\tau$ . If  $A(\Omega)$  is taken to be one for all frequencies (i.e.  $\mathcal{F}(E_{pump}(\omega))(t)$  is a delta pulse), the polarization corresponds to the probe field times the Fourier transformed of  $\chi$ , which is an exponentially decaying oscillation in the case of Lorentzian line shape (i.e. the Fourier transform of Equation 4.3).  $E_{probe}$  samples this exponentially decaying oscillation in time steps of  $\tau$ , a process very similar to a pump probe experiment. The signal  $s(\tau)$  measured with a photodetector is then proportional to the time integrated, if the detector is slow on the time scales of the optical frequencies ( $\omega_{pump}$ ,  $\omega_{Stokes}$ ,  $\omega_{probe}$  and  $\Omega$ ), absolute square

of Equation 4.5:

$$s(\tau) \propto \int_{-\infty}^{\infty} dt |E_{probe}(t - \tau)|^2 |\mathcal{F}(\chi(\Omega) * A(\Omega))(t)|^2 \quad (4.6)$$

which is the convolution between the probe intensity and a term accounting for the coherently generated excitation.

The effect differently shaped pulses have on the recorded signal can be deduced from Equation 4.6. A chirped pulse for example has a lower peak intensity but a larger overlap in the convolution, this interplay between pulse intensity and overlap in the convolution, for example, leads to distinct maxima in the signal measured against pulse chirp.

Giving a closer look at Equation 4.6 reveals that it is the pulse intensity envelope which matters and not the field itself. Therefore, effects affecting the field but not the overall shape of the pulse should have no influence on the signal, for example, the signal should be independent of the carrier envelope phase shift, which affects the field cycle to envelope position but not the overall intensity envelope. Indeed this turns out to be the case.

Equation 4.6 indicates how the CARS signal and nonresonant background can be separated. The nonresonant background is instantaneous, it is only generated during the interaction of a pulse with the sample. After the pulse transit, only the longer lived coherent excitation lives on. The nonresonant background caused by third order nonlinear processes, is heavily dependent on the intensity inside the sample. During the overlap of the two pulses the intensity is strongly increased leading to a strong non resonant spike at  $\tau = 0$ . Windowing out this part of the signal leads to a strongly reduced nonresonant background. Nevertheless every pulse generates a nonresonant background signal for itself. It therefore shows up in the detected signal as a short spike appearing at the repetition rate but suitable electrical filtering eliminates this contribution in the overall signal. The combination of electronic filtering and software windowing of the recorded signal leads to a nearly nonresonant background free signal. Finally, the two pulses are interchangeable whichever comes first acts as pump and the following pulse acts as probe.

Viewing dual-comb CARS as a pump probe experiment, offers a very intuitive explanation. The first pulse generates a coherent excitation of a molecular vibrational level. Coherently excited vibrating molecules cause a modulation of the materials bulk refractive index with the frequency of their vibrational motion. The second pulse of the pulse pair feels this refractive index modulation, and depending on the slope of the refractive index modulation, it is blue or red shifted. If the probe pulse is very short red and blue shifted light is not generated at the same time, blue and red shift have a  $\pi$  phase shift relative to each other. The probe pulse samples the refractive index modulation, which follows the vibrational motion of the molecules. This process maps the time scales of

molecular vibrations to a time scale determined by the speed of increase in delay in the pulse pairs.

As a nonlinear process CARS is subjected to phase matching. For the CARS intensity one can write [155]:

$$I_{CARS}(t) \propto I_{pump}(t) I_{pump}(t) I_{probe}(t) \chi^2 \text{sinc}^2 \left( \frac{\Delta k l}{2} \right)$$

$$\Delta k = k_{pump} - k_{stokes} + k_{probe} - k_{CARS} \quad (4.7)$$

with the interaction length  $l$  and the wave vectors of the corresponding fields  $k_i$ . If  $\Delta k$  increases, the sinc function falls off rapidly and the CARS signal vanishes. To circumvent this problem a special geometrical arrangement of the incident laser fields was chosen in the early CARS experiments. Nevertheless, it turns out that in a tightly focused beam the phase matching condition is also fulfilled. For a numerical aperture larger than 0,2 the phase match increases monotonically to a maximum value [156, 157]. For a numerical aperture larger than 0,3 the signal is effectively independent from phase mismatch [158].

This is true for the forward scattered light but for the backward or epi direction the phase matching is not fulfilled under tight focusing. For a single small scatterer the signal would be emitted in a dipole pattern, in backward and forward direction with the same intensity. As the number of scatterers increases the light emitted in forward direction undergoes constructive interference but the light in backward direction undergoes destructive interference. Therefore from a bulk material no backward scattered light should be emitted. For backward scattered light to be detected from the bulk the interaction length  $l$  has to be small, then Equation 4.7 yields a non zero value despite a large  $\Delta k$ , or the scattering object has to be small enough to prohibit complete destructive interference, this also includes sharp discontinuities e.g. the walls of a cuvette. Finally forward scattered light can be (linearly) scattered to propagate in the backward direction.

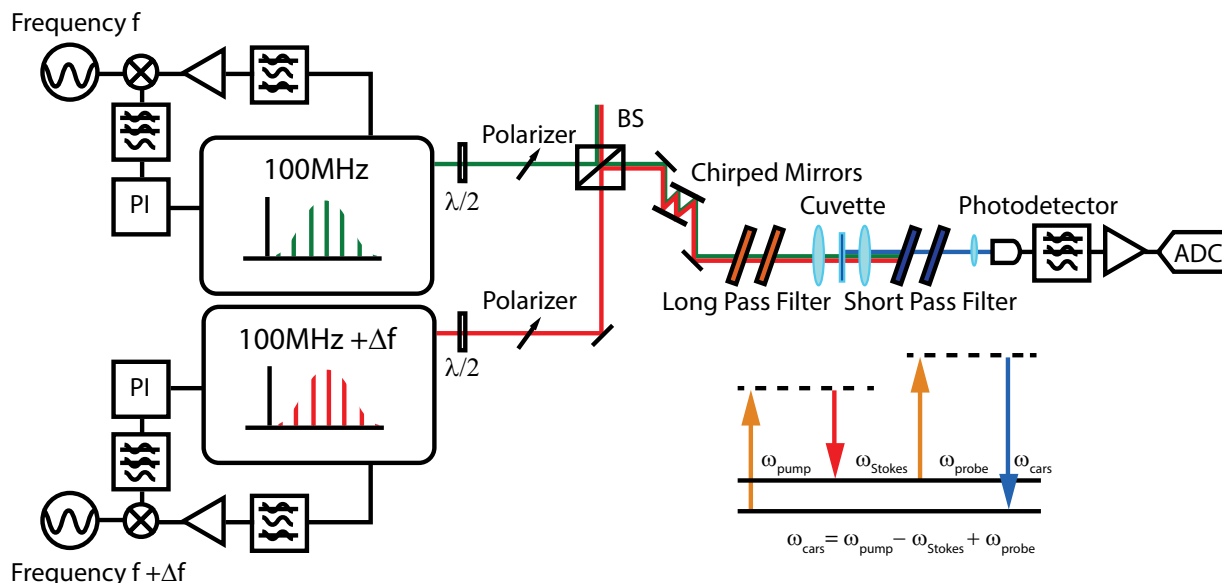


**Figure 4.3:** Experimental setup for dual-comb CARS spectroscopy. The power of the beams can be adjusted individually using a combination of  $\lambda/2$  plate and polarizer. The polarizations are set orthogonal. The beams of two ultra short pulse lasers are combined on a beam splitter (BS) and subsequently spectrally (long pass) filtered. The combined beams are then focused with a lens into a cuvette, filled with the sample and collimated after the sample again with a second lens. Short pass filters after the sample remove remaining fundamental light. The blue shifted radiation is finally focused onto a photodetector (PD). Each laser repetition frequency is stabilized against a radio frequency signal with a proportional integral controller and an analog mixer used as phase comparator.

## 4.2 Coherent Anti Stokes Raman Dual-Comb Spectroscopy

*Related Article*[159]:

*Coherent Raman spectro-imaging with laser frequency combs*

*T. Ideguchi<sup>†</sup>, S. Holzner<sup>†</sup>, B. Bernhardt, G. Guelachvili, N. Picqué, and T. W. Hänsch*

<sup>†</sup> *These authors contributed equally to this work*

*Contribution: Layout and setup of the system as well as experimental work together with T. Ideguchi. Discussed the manuscript.*

To enter the field of coherent Raman experiments, spectroscopy in forward direction was chosen as a starting point, motivated by the simplicity of the setup, excluding as much error sources as possible. After the spectroscopy experiment was set up successfully, it was first rebuilt to detect CSRS instead of CARS. Finally, it was rebuilt again to detect

backward scattered CARS. The setup strongly reassembles e.g. the setup of a dual-comb absorption experiment. Two ultra short pulse laser sources are overlapped in a broadband beam splitter and sent through the sample. The setup is outlined in Figure 4.3 and described in detail in the following.

### Laser Sources

Two Kerr lens mode locked Titanium Sapphire lasers (Synergy, Femtolasers) are used as sources. The repetition rate of the sources is close to 100 MHz at an average power of 1 to 1,3 W, corresponding to 10 to 13 nJ pulse energy. The pulses have a duration of under 20 fs, usually about 17 fs, corresponding to a peak power of 440 kW at the worst (13 nJ and 20 fs) and around 670 kW (13 nJ and 17 fs) at the best possible condition for a *sech*<sup>2</sup> shape.

These lasers were chosen for several reasons: they offer a smooth spectrum, a high power, short pulses and a centre wavelength where the majority of possible samples is transparent. CARS is a nonlinear process which has a quadratic and a linear dependence on the intensities of the pump and the probe respectively. A short pulse with high pulse energy increases the signal significantly, but the same holds true for the nonresonant background.  $\chi_{NR}$  is large if the laser wavelength is close to a resonant electronic transition. At a central wavelength of the laser system of  $\sim 790$  nm, the closest electronic transition for most samples is a two photon transition. The excitation maximum of these transitions is still rather far away from the wavelength region of the laser systems [160]. If a (strongly) conjugated system is involved (e.g. Anthracene or Naphthacene), two photon transitions can become strong and so will the nonresonant background (e.g.[161]) but such strongly condensed systems are rarely encountered. Additionally in the prospect of a biological sample a long wavelength laser system is beneficial as multiphoton absorption is one major cause of sample damage [162, 163, 164]. Similarly a short pulse allows lower average power on the sample, reducing the (linear) damage caused by a high average power on the sample [162].

### Laser stabilization

A drift of the laser repetition rate is avoided by first setting it to the desired value using a picomotor actuated mirror in the cavity and consecutively locking it to a hydrogen maser, using a piezo actuated cavity mirror. The correction signal is generated in a common way from an analog mixer used as a phase frequency detector between the repetition frequency and the hydrogen maser signal. This error signal is then fed into a proportional integral controller connected to the intra cavity piezo mirror. At the exit of the laser, in the housing a thin glass plate reflects a small part of the laser power on a wide bandwidth photodiode where the repetition frequency is measured. It allows locking to a harmonic of the repetition rate, usually the 10th harmonic. This lock does

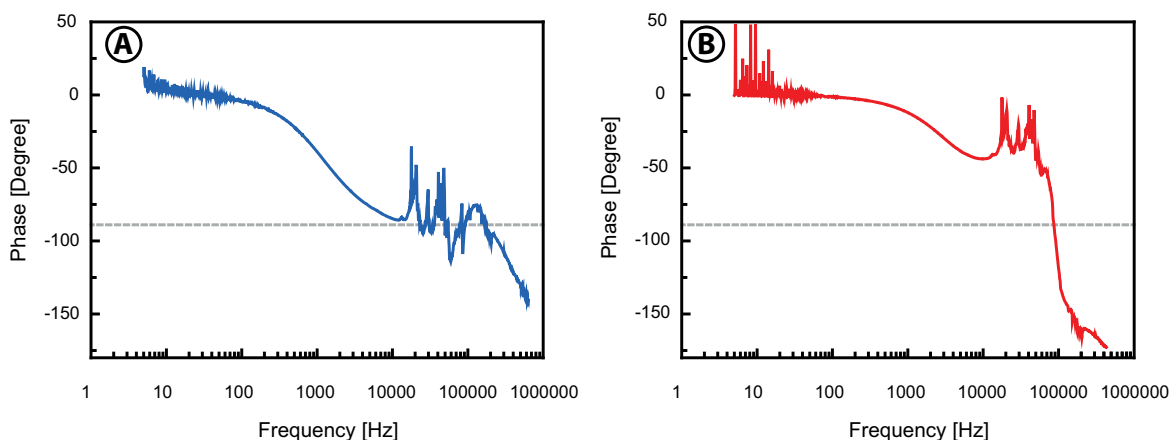


**Figure 4.4:** Bode plots of the phase of the stabilization scheme. The dashed line indicates 90 degrees phase shift. **A** 50 Ohm isolation resistance **B**  $A(\Omega)$  10 Ohm and  $1 \mu F$  parallel. The strong modulations at very low frequency are a measurement artifact of the Network-Analyzer used.

not influence a single spectrum as the locking bandwidth is by far too small to act on the (microsecond) time scale of a single acquisition. The maximal correction takes place at a frequency scale of kilohertz to, at best, tens of kilohertz. Figure 4.4 plots the phase transfer function of the locking system, including the piezo. The addition of a RC filter (at around 10 kHz) to introduce a pole in the transfer function pushes the 90 degree phase transition, ultimately limiting the locking bandwidth, to higher frequency (Figure 4.4B). Nevertheless, it is found that adding such a filter does not improve the quality of the recorded spectra. The lock prohibits a drift of the laser and thereby a possible change in the difference in repetition rate  $\Delta f$  and, finally, a drift in the downconversion factor. The stabilization is never changed during all coherent Raman scattering experiments and always used if not stated differently. It is only explicitly shown in Figure 4.3 and left away in the following schematics of coherent Raman scattering setups for clarity.

### Beam Path

The laser power is controlled individually for each source as each beam traverses a half wave plate and a polarizer before they are overlapped in a Pellicle beam splitter, which provides broadband capabilities as well as a minimum amount of dispersion. The polarization of both beams is linear but orthogonal to each other in order to reduce background signals. Whereas this suppresses interferometric background, the fast depolarization of the molecules ensures that the CARS signal is mainly unharmed. Since CARS has a cubic dependence on the peak intensity of the pulses on the sample, they are desired to be as short as possible. In order to precompensate the (second order) dispersion accumulated on the beam path from the laser sources to the sample, a matched pair of chirped mirrors (Layertec) is used.

Separation of the CARS signal from the fundamental beams is ensured, in a first step, by optical filtering with a low pass filter (ET750LP Chroma Technology) in front of the sample, cutting off the spectrum at wavelengths shorter than 750 nm. The light is consecutively focused inside a 5 mm long, sample filled cuvette and collimated again, using lenses with a focal length of 20 mm. A mixture of four different organic solvents is used as sample: toluene, nitrobenzene, perfluorobenzene and nitromethane. The average power on the sample is 300 mW per beam. Fundamental light is finally stripped of with a short pass filter (3RD740SP Omega Optical Inc.), letting only the blue shifted CARS radiation with a wavelength shorter than 740 nm pass. The isolated CARS radiation is focused on a home built amplified photo diode. To eliminate signals caused by fundamental light, nonresonant background etc. the signal is low pass filtered to a band smaller or equal to 50 MHz, a combination of a low pass filter (BLP-50+ Mini Circuits) and notch filter (NSBP-108+ Mini Circuits) is used to suppress the strong signal at 100 MHz. This signal filtering also ensures that the signal is not aliased. Before digitization the signal is amplified to the most favourable voltage level for the digitizer (ATS9462 Alazartech) with a variable gain amplifier (DHPVA-100 FEMTO Messtechnik GmbH). The very same setup can also be used to detect CSRS. For this purpose only the optical filtering has to be changed. The right choice of filtering is crucial for CSRS as well as for CARS. It determines the minimal measurable Raman shift, if the signal is not shifted far enough, from one filtering edge to the other it simply does not appear on the detector and hence is not measurable. The filtering chosen to record CARS is a 750 nm low pass (ET750LP Chroma Technology) and a 740 nm short pass (3RD740SP Omega Optical Inc.), setting the low frequency cut off the Raman frequency to  $\sim 180 \text{ cm}^{-1}$ . The maximum measurable Raman shift on the other hand is given by the maximal laser bandwidth of  $\sim 1666 \text{ cm}^{-1}$ . If the filtering is implemented the maximal bandwidth is reduced as the spectral bandwidth decreases, thus for the chosen filtering the maximal bandwidth reduced to  $\sim 1400 \text{ cm}^{-1}$ .

### Recording Parameters and Data Processing

To choose the recording parameters in such a way that a minimal measurement time is achieved, an optical bandwidth from zero to the highest Raman frequency has to be fitted into half of the baseband. The maximal occurring Raman frequency is given by the maximal laser bandwidth and is around 50 THz. Following Equation 2.20 the minimal downconversion factor can be calculated to one million, which sets the maximal difference in repetition rate to 100 Hz, for the given laser system. A lower difference in repetition rate leads to a longer measurement time but an increased signal-to-noise ratio as the number of sampling points increases. To improve the signal clarity (i.e. suppress spectral leakage) a triangular window function is applied to the recorded data. The desired resolution of the Raman spectra is  $4 \text{ cm}^{-1}$  (120 GHz). A significantly higher resolution is not necessary for a liquid sample as the lines are broadened by 90 GHz to 120 GHz [165, 166]. Improving the resolution only leads to noise being added to the

spectrum without gain of additional information. Using equation 2.16 yields a radio frequency resolution of 120 kHz, which converts to a minimal recording time of 15  $\mu\text{s}$ , including a factor of 1,8 accounting for the window function. In addition to experiments with the above calculated parameters, experiments with a difference in repetition rate of 5 Hz are conducted to increase the signal-to-noise ratio. Under this circumstances the measurement time increases to 295  $\mu\text{s}$  for the same resolution, again including a factor of 1,8 for the window function.

At the time of overlap between the pulses of a pulse pair a strong, non resonant signal is generated, masking the weaker signals generated due to the coherent molecular excitation. It is characterized by a strong, asymmetric peaked signal, which is owed to the nonlinear origin of the signal. When the pulses are not temporally overlapping anymore, signal is generated only by the long lived coherent excitation. It decays with a time constant given by the molecular coherence time, which is, in the case of a liquid sample  $\sim 10$  ps. Data acquisition is triggered by the non resonant strong asymmetric peaked signal and a data array is recorded corresponding to the maximal memory size of the acquisition system ( $\sim 4$  million points). For signal analysis the samples corresponding to the overlap of pump and probe pulses are discarded and a windowed portion of a data set is Fourier transformed. The window width is given by the desired resolution, which is the inverse of the measurement time for a boxcars window. For different window functions the broadening of the lines has to be taken into account and the measurement time taken accordingly longer (e.g. 1,8 times longer for a triangular window function i.e. the Bartlett window [167]). Excluding the overlap region of the pulses efficiently eliminates the non resonant background. Before the Fourier transform is performed the data is zero padded fourfold. Where not stated otherwise this data processing scheme was used for all data.

### CARS Spectra

The Fourier transform of the signal yields the spectra depicted in Figure 4.5. The two spectra are taken with 100 and 5 Hz difference in repetition rate. The signal-to-noise ratio is high for both spectra, measured for the most intense line at  $1000\text{ cm}^{-1}$ , which is a blended line from toluene and nitrobenzene. It amounts to 200 for the spectrum taken with 100 Hz difference in repetition rate and to 1000 for the spectrum taken with 5 Hz difference in repetition rate. It is slightly more (0,5dB) than the increase in sampling points  $\sqrt{20} \approx 4,5$  would let expect and might be attributed to a slight drift in the laser parameters (e.g. poynting or power).

### Coherent Stokes Scattering CSRS

The same setup can also be used to measure CSRS instead of CARS. Only the positions of the short and the long pass filter have to be swapped and the values of the filters have

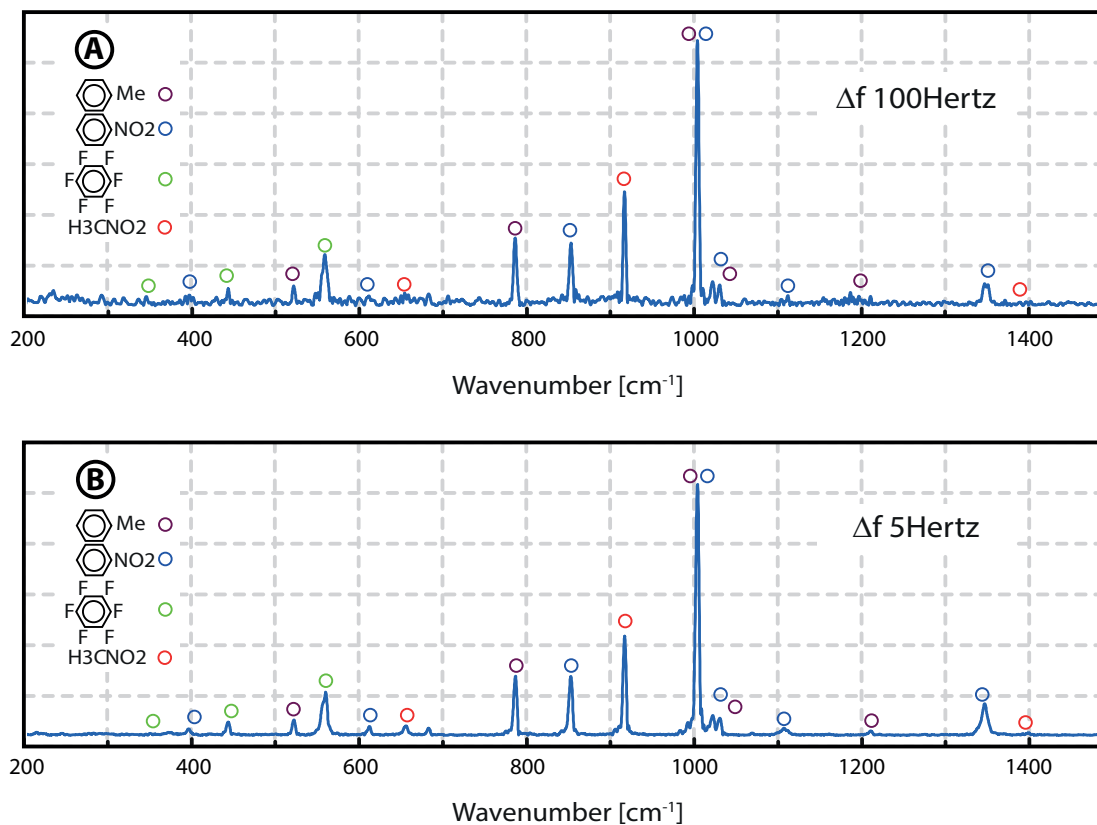


**Figure 4.5:** CARS spectra taken with different  $\Delta f$  and a mixture of four different solvents toluene, nitrobenzene, nitromethane and perfluorobenzene **A** CARS spectrum taken with  $\Delta f = 100$  Hz and a recording time of  $15 \mu\text{s}$ . Energy per pulse:  $3 \text{ nJ}$  **B** CARS spectrum taken with  $\Delta f = 5$  Hz Hertz and a recording time of  $295 \mu\text{s}$ . Energy per pulse:  $3 \text{ nJ}$ .

to be adapted. Figure 4.6B depicts the changed setup. Only the filters are interchanged in position and the filters cut off wavelengths are changed to a  $825 \text{ nm}$  short pass filter and a  $850 \text{ nm}$  long pass filter, covering a Raman transition range and from  $400 \text{ cm}^{-1}$  to  $1400 \text{ cm}^{-1}$ .

In Figure 4.6D a CSRS spectrum is plotted taken with a difference in repetition rate of  $10 \text{ Hz}$  and a resolution of  $120 \text{ GHz}$ , corresponding to a measurement time of  $150 \mu\text{s}$ , including the windowing factor. The sample is neat toluene. The signal-to-noise ratio is comparable to the one of (forward collected) CARS.

### Backward Scattered CARS

Similarly the backward directed CARS signal can be detected using a slightly rebuilt setup. For backward detection the forward propagating beams (CARS and fundamental) are sent into a beam block. The backward scattered CARS signal is reflected from the

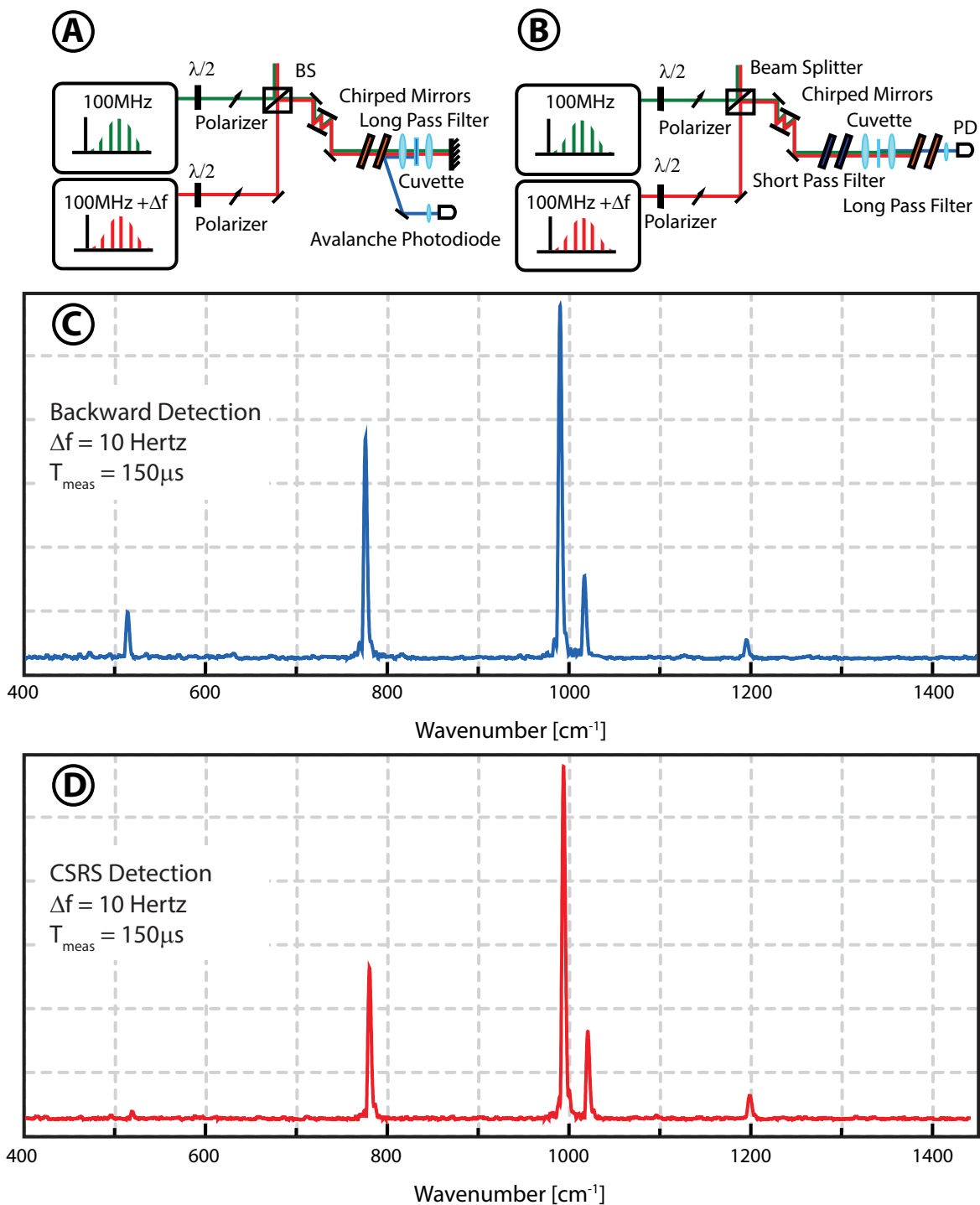


**Figure 4.6:** **A** Experimental setup for backward CARS detection. **B** Experimental setup for CSRS detection, long and short pass filters changed positions compared to the CARS setup. **C** Backward detected CARS spectrum taken with  $\Delta f = 10$  Hz and a recording time of  $150 \mu\text{s}$  **D** CSRS spectrum taken with  $\Delta f = 10$  Hertz and a recording time of  $150 \mu\text{s}$ .

	Resolution	Measurement Time	Spectral Span	signal-to-noise
This work	4 cm <sup>-1</sup>	15 $\mu$ s	1200 cm <sup>-1</sup>	200
This work	4 cm <sup>-1</sup>	295 $\mu$ s	1200 cm <sup>-1</sup>	1000
[168]	20 cm <sup>-1</sup>	more than 80s	800 cm <sup>-1</sup>	50
[169]	5 cm <sup>-1</sup>	20ms	400 cm <sup>-1</sup>	10
[170]	6 cm <sup>-1</sup>	4s	300 cm <sup>-1</sup>	800

**Table 4.1:** A comparison between of the measurement parameters of the technique presented with literature values.

long pass filter positioned in front of the sample and then send onto a photodetector. Figure 4.6A sketches the altered beam path. As the filter a 750 nm long pass is used. The difference in repetition rate is set to 10 Hz and the resolution to 120 GHz. Toluene is used as sample. Reducing the thickness of the cell from 5 to 1 mm increases the signal strength. To account for an overall lower signal intensity the photodiode is replaced with an avalanche photodiode (Thorlabs APD120A2). No backward CARS radiation should be produced in a bulk sample but under the tight focusing condition the focal spot is very small and hence the Rayleigh length short. If it is short enough to produce non zero values in Equation 4.7, backward CARS can be detected, which is the case for the conditions of this experiment. Figure 4.6C shows a plot of the backward collected CARS signal, the Raman transitions are clearly visible in the spectrum.

### Summary Coherent Anti Stokes Raman Dual-Comb Spectroscopy

The use of a dual-comb type of measurement to generate and detect coherent Raman radiation is demonstrated. Raman spectra can be detected within a very short measurement time between 15  $\mu$ s and 295  $\mu$ s, limited by the desired resolution only. Similarly the resolution can be increased by increasing the sampling time. The recorded spectra have an excellent signal-to-noise ratio of 200 and 1000 for the most intense line, which is more than enough to clearly identify the components of the mixture used as a sample. The spectral coverage is solely limited by the bandwidth of the laser source on one hand and on the chosen spectral filtering on the other. Under the current conditions a spectral coverage from 200 to 1400 cm<sup>-1</sup> is achieved.

In a slightly altered setup CSRS can be detected, with a sample (toluene) not generating red shifted background signals as one photon fluorescence, the signal-to-noise ratio is comparable to the signal-to-noise ratio achieved with CARS. Finally, backward scattered CARS radiation can be detected, which is an important aspect if a strongly scattering sample is used, as e.g. in a microscopy setup using a tissue sample. The striking point of these measurements is the good balance between all measurement parameters: resolution, measurement time, spectral span and signal-to-noise ratio. Table 4.1 compares measurement parameters with literature values to illustrate above said.

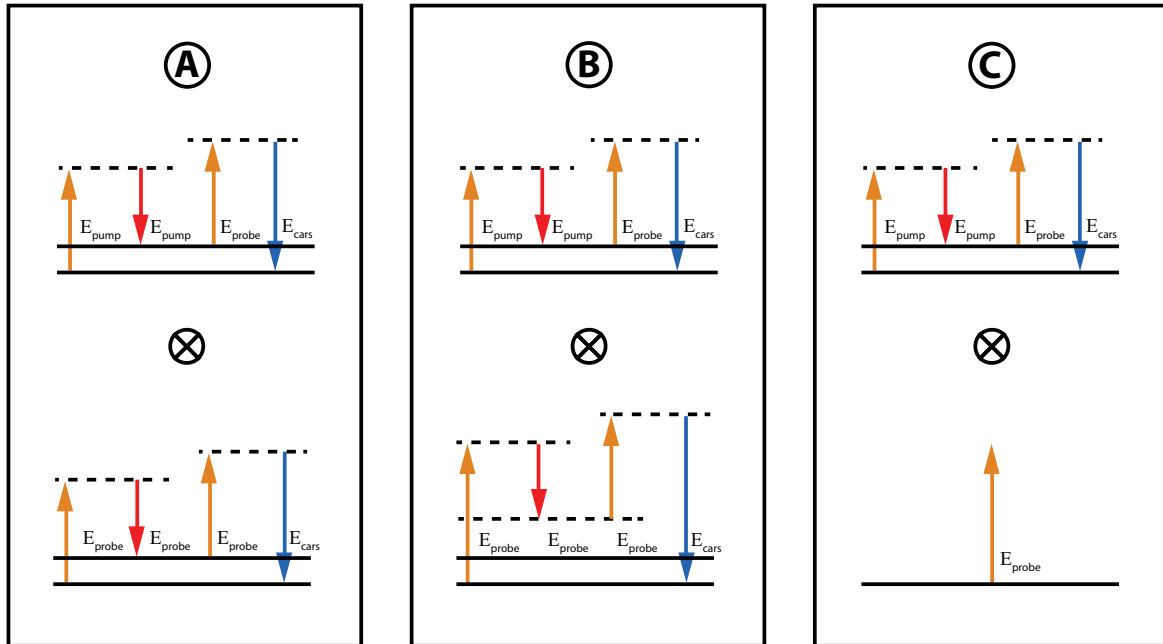


**Figure 4.7:** Different possible combinations for heterodyne detection **A** Mixing of the interferometric CARS signal and CARS solely generated by the probe beam. **B** Mixing of the interferometric CARS signal and nonresonant signal generated by the probe beam. **C** Mixing of the interferometric CARS signal and fundamental light of the probe beam.

### 4.3 Concentration and Power Dependence of Dual-Comb Coherent Anti Stokes Raman Spectroscopy And Heterodyne Detection

*Contribution:* Layout and setup of the system as well as experimental work together with M. Yan and T. Ideguchi.

#### Theoretical Considerations

When using power sensitive and/or diluted samples, the power and concentration dependence of nonlinear effects can become a problem. A (biological) cell for example will be damaged easily with too high incident power (average and peak power), while the cytoplasm mainly consists of water and other not Raman active substances. As Equation 4.7 indicates, CARS has a cubic dependence on the incident intensity and a quadratic dependence on  $\chi$ , which contains  $N$  the number of molecules, therefore giving

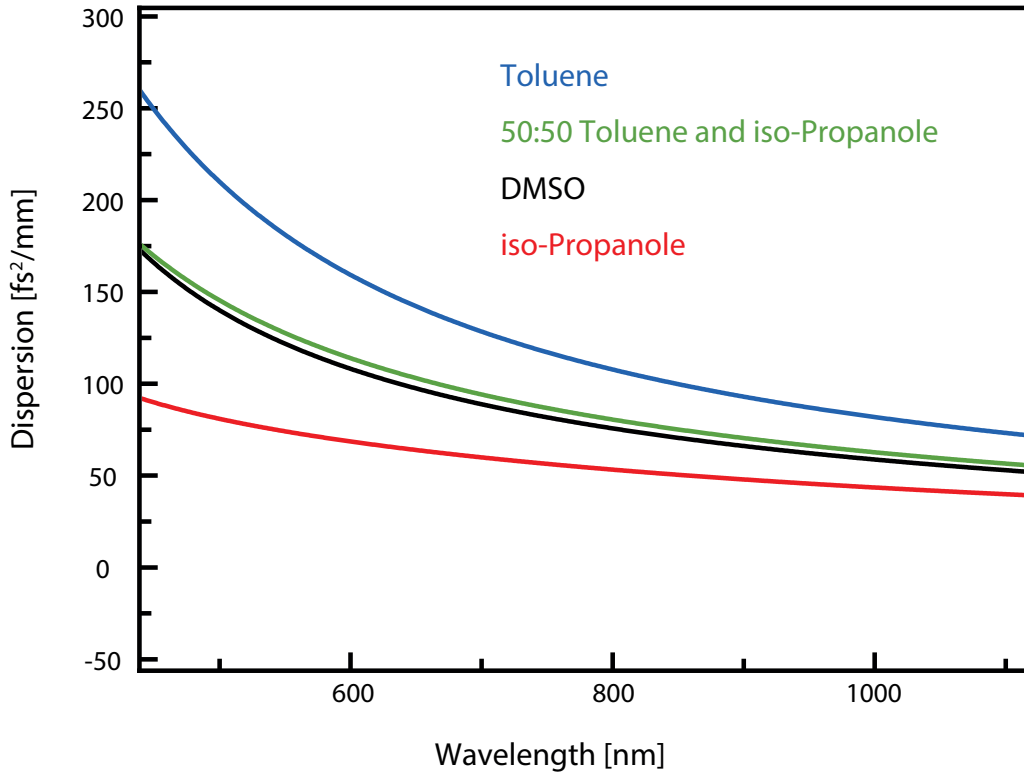
the CARS signal strength also a quadratic dependence on the molecular number. For diluted samples and low intensity incident light these scaling laws become a significant problem as the CARS signal falls off rapidly. A way to change this scaling laws and increase the signal of interest is heterodyne detection. The weak optical signal of interest is mixed with a strong local oscillator generating a strong optical beat signal containing the information of the weak input signal. In the case of CARS, besides the CARS field generated by the two lasers, several possible strong fields exist or are generated to heterodyne with.

Figure 4.7 sketches three different heterodyne mixing possibilities. In Figure 4.7A the CARS field generated from the two different laser systems ( $E_{CARS}$ ; generated by  $E_{pump}$  and  $E_{probe}$ ) heterodynes with the CARS field generated by a single laser system ( $E_{CARSsingle}$ ; generated by  $E_{probe}$ ). Figure 4.7B depicts another possible combination: the CARS field generated from the two different laser systems ( $E_{CARS}$ ; generated by  $E_{pump}$  and  $E_{probe}$ ) and the non resonant background generated by the probe laser ( $E_{NR}$ ; generated by  $E_{probe}$ ). Finally Figure 4.7C sketches a third possibility, the CARS field generated from the two different laser systems ( $E_{pump}$  and  $E_{probe}$ ) can also be mixed with fundamental light of the probe laser. The pump pulses have no temporal coincidence with the detection and therefore yield no useful heterodyne signal. Which of the first two possibilities (see Figure 4.7A and B) prevails depends on the intensity of the respective heterodyne field. It is usually the non resonant background field as it tends to be much stronger than the CARS field. Both combinations lead to the same power dependence on the pump and probe fields, a linear dependence on the pump and a quadratic dependence on the probe:

$$\begin{aligned}
 S &\propto E_{CARS} E_{CARSsingle} \propto \chi_{CARS}^2 \left( E_{probe} |E_{pump}|^2 \right) \left( E_{probe}^* |E_{probe}|^2 \right) \propto \chi_{CARS}^2 I_{probe}^2 I_{pump} \\
 S &\propto E_{CARS} E_{NR} \propto \chi_{CARS} \chi_{NR} \left( E_{probe} |E_{pump}|^2 \right) \left( E_{probe}^* |E_{probe}|^2 \right) \propto \chi_{CARS} \chi_{NR} I_{probe}^2 I_{pump}
 \end{aligned}
 \tag{4.8}$$

If the non resonant background is generated by the same molecules as CARS (which shall be called  $N_{CARS}$ ),  $\chi_{NR}$  has the same dependence on the molecule number as  $\chi_{CARS}$  and the concentration dependence will be quadratic ( $\chi_{CARS}(N_{CARS})\chi_{NR}(N_{CARS}) \propto (N_{CARS})^2$ ). This is not a necessity, the heterodyne signal can show an either linear or quadratic concentration dependence, according to the dependence of  $\chi_{NR}$  on the molecular type. For example, in a binary mixture of a Raman active ( $N_{CARS}$ ) and a Raman inactive ( $N_{nil}$ ) sample both samples can generate a non resonant signal. Reducing the Raman active sample by adding more Raman inactive sample therefore has no effect on  $\chi_{NR}$  ( $N_{CARS} + N_{nil}$  stays constant) and the power dependence is linear.

When fundamental light is present, it generates the dominant signal term as it is generally much stronger than the non linearly generated fields. Then the power and concentration



**Figure 4.8:** Dispersion of three different solvents, toluene, a 50:50 mixture of toluene and iso-propanole, DMSO and iso-propanole as a function of wavelength. The dispersion values have been calculated using Sellmeiers equations.

dependence is significantly altered:

$$S \propto E_{CARS} E_{probe} \propto \chi_{CARS} \left( E_{probe} |E_{pump}|^2 \right) \left( E_{probe}^* \right) \propto \chi_{CARS} I_{probe} I_{pump} \quad (4.9)$$

This leads to a linear dependence on the pump and the probe intensity as well as a linear dependence on  $\chi_{CARS}$  i.e. a linear dependence on the molecular number.

The above considerations suggest that heterodyne detection with fundamental as well as nonlinearly generated light is possible. It can be distinguished by its power and concentration dependencies.

### Experimental Setup

To assess the different possibilities of heterodyne detection the setup described in Section 4.2 is used for power and concentration dependence experiments. Two different configurations are implemented: heterodyne detection with the nonlinearly generated fields and heterodyne detection with fundamental light.

To ensure that no other effects are influencing the measurement a sample has to be chosen which does not change optical properties on dilution. Toluene - iso-propanole mixtures, for example, exhibit a concentration dependent dispersion property. To avoid a concentration dependent dispersion, a three component mixture is chosen, consisting of a 50:50 mixture of toluene and iso-propanole which is mixed with dimethylsulfoxide (DMSO). Figure 4.8 illustrates that the dispersion of this mixture is approximately the same as the dispersion of DMSO over a wide bandwidth. Another possible combination is a solvent and its deuterated analogon as e.g. benzene and deuterio-benzene or chloroform and deuterio-chloroform. The influence of a concentration dependent dispersion can be investigated in detail using Formula 4.5 and Formula 4.6.

### Heterodyne Detection with Nonlinearly Generated Fields

First heterodyne detection with nonlinearly generated fields is examined. Therefore the 750 nm long pass filter in the setup (see Section 4.2) is replaced with a 760 nm long pass to ensure no fundamental light is present on the detector. To measure the concentration dependence the 50:50 toluene and iso-propanole mixture is diluted with DMSO. The signal intensity is determined for the Raman transition of DMSO at  $680\text{ cm}^{-1}$ .

A log-log plot of this dependence is (linearly) fitted and a slope of 1,96 determined, as illustrated in Figure 4.9A. This confirms that no heterodyne detection with fundamental light is done and a quadratic dependence on the probe and a linear dependence on the pump intensity can be expected. To prove that this is the case, a power dependence measurement is conducted on neat DMSO. In Figure 4.9B, a log-log plot is used again to plot and fit the outcome in order to determine the corresponding slopes. It resulted in a slope of 1,03 for the pump and a slope of 1,97 for the probe light. A result in good congruence with the theoretical prediction. Which of the nonlinearly generated signals serves as heterodyne field cannot be deduced in this way. DMSO has a high linear refractive index, hence it can be assumed that the third order nonlinear susceptibility is also high according to Wang's rule ([171]), leading to a strong nonresonant background. The same argument holds true for toluene. Mixing toluene and DMSO should hence not significantly influence the amount of the generated non resonant background radiation, since the number of molecules generating a non resonant signal stays approximately the same or even increases. Following this train of thought the CARS signal generated by the probe alone is then the heterodyne field, as the concentration dependence is quadratic. Nevertheless this is just an hypothesis only an experiment can substantiate.

### Heterodyne Detection with The Fundamental Field

To take heterodyne detection with the fundamental light under scrutiny, in the setup the 760 nm long pass filter in front of the sample is replaced by a (slightly tilted) 750 nm long pass. Using fundamental light as the heterodyne field increases the signal-to-noise

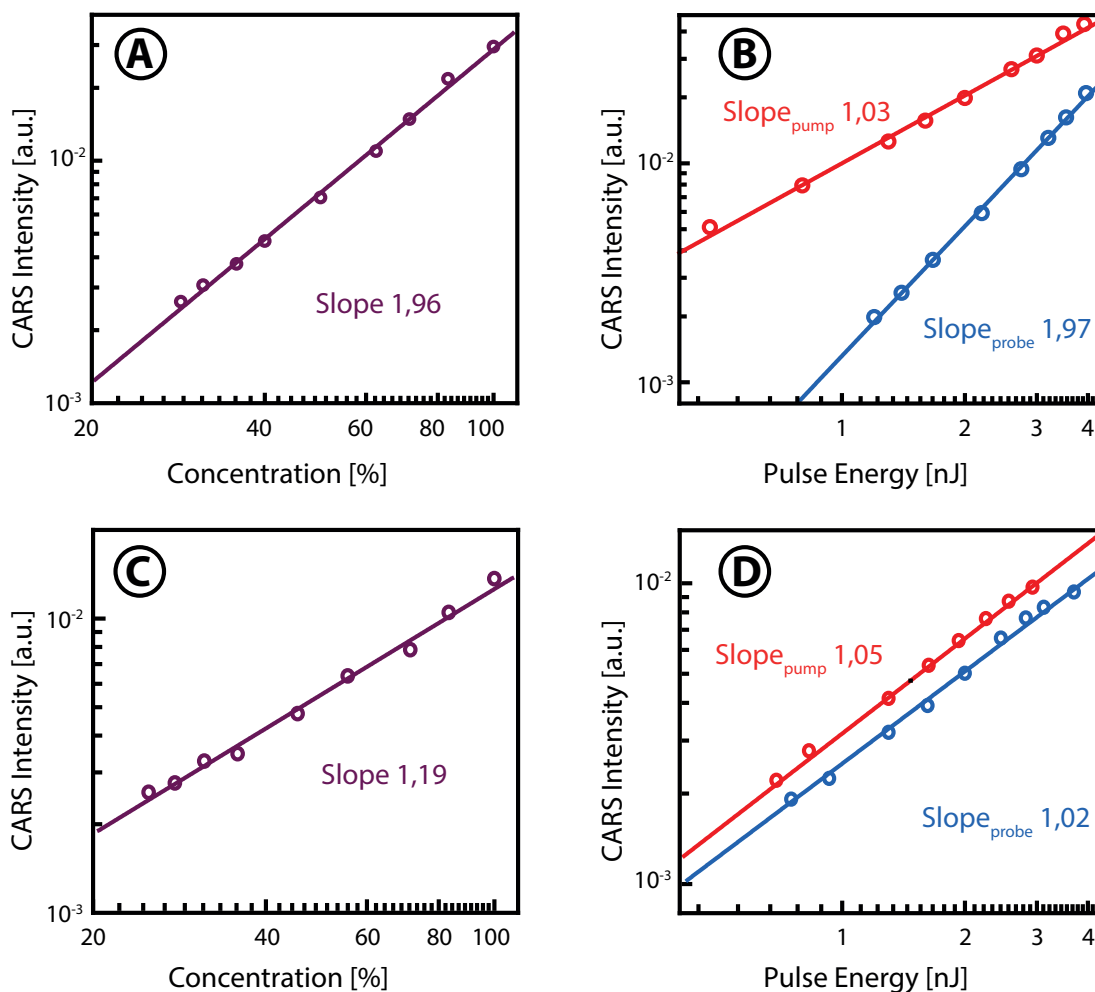


**Figure 4.9:** **A** Dependence of the CARS signal intensity on the concentration of DMSO in a dilution with a 50:50 toluene iso-propanole mixture, in the case of heterodyne detection using nonlinearly generated fields. **B** Dependence of the CARS signal intensity on the incident powers of pump and probe beam, in the case of heterodyne detection using nonlinearly generated fields. **C** Dependence of the CARS signal intensity on the concentration of DMSO in a dilution with a 50:50 toluene iso-propanole mixture, in the case of heterodyne detection using the fundamental field. **D** Dependence of the CARS signal intensity on the incident powers of pump and probe beam, in the case of heterodyne detection using fundamental light.

ratio of the measurement by almost a factor of 2 compared to the measurement with the nonlinearly generated fields (always determined for the strongest line of toluene at  $\sim 1000 \text{ cm}^{-1}$ ). The concentration dependence of the signal is measured using the same mixture of toluene and iso-propanole diluted with Dimethylsulfoxide and the outcome is plotted in Figure 4.9C on a log-log scale. The graph is (linearly) fitted and a slope of 1,19 is determined, indicating a linear dependence on the concentration as predicted by Equation 4.9. Also the power dependence is determined on neat DMSO, which is plotted in Figure 4.9D. The fits to the graphs yield slopes of 1,05 and 1,02, which again is in very good agreement with the prediction.

### **Summary Concentration and Power Dependence of Dual-Comb Coherent Anti Stokes Raman Spectroscopy and Heterodyne Detection**

Using these heterodyne techniques allows to efficiently change the power and concentration dependence of the recorded signal. Heterodyne mixing with the nonlinearly generated fields is exploited in Section 4.5, it allows to elegantly decrease the dead time in between interferograms with a minimum of signal loss. Heterodyne detection using fundamental light is interesting when only small quantities of sample are present, as it is the case for most biological samples. Additionally, it allows to make a quantitative statement about the concentration of a certain specimen as a linear dependence on the molecular number is given. Without heterodyne conditions an intensity proportional signal is measured, which contains the square of  $\chi_{CARS}$ . Due to the appearing mixing terms, concentration analysis is getting more complex with a larger number of specimen.

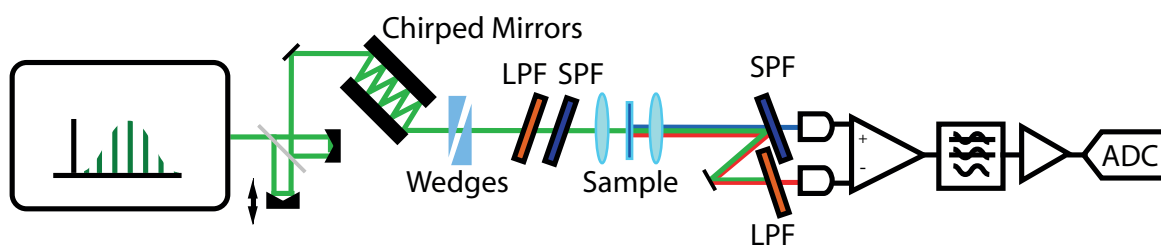


**Figure 4.10:** Experimental setup for differential coherent Raman Stokes and anti-Stokes spectroscopy. SPF short pass filter; LPF long pass filter

## 4.4 Differential Coherent Raman Spectroscopy

*Related Article (in preparation):*

*Differential femtosecond coherent Stokes and anti-Stokes Raman spectroscopy*

*T. Ideguchi, S. Holzner, M. Yang, G. Guelachvili, T. W. Hänsch and N. Picqué*

*Contribution:* Layout of the experiment together with T. Ideguchi. Setup of the system and experimental work together with T. Ideguchi and M. Yang. Discussed the manuscript.

Based on the description of CARS and CSRS given in Section 4.1, CSRS and CARS should have a  $\pi$  phase shift with respect to each other. It indicates that CARS has a maximum in intensity when CSRS has a minimum and vice versa. If these two signals have the  $\pi$  phase shift a differential detection of both should be possible. A scanning Michelson interferometer is set up and a Raman experiment is conducted. The Raman signals are measured in a differential detection scheme. A differential detection scheme is generally a preferable setup, as not only the signal is increased by a factor of two but also common noise is cancelled, which can be a major contribution in the signal-to-noise ratio (e.g. [172]).

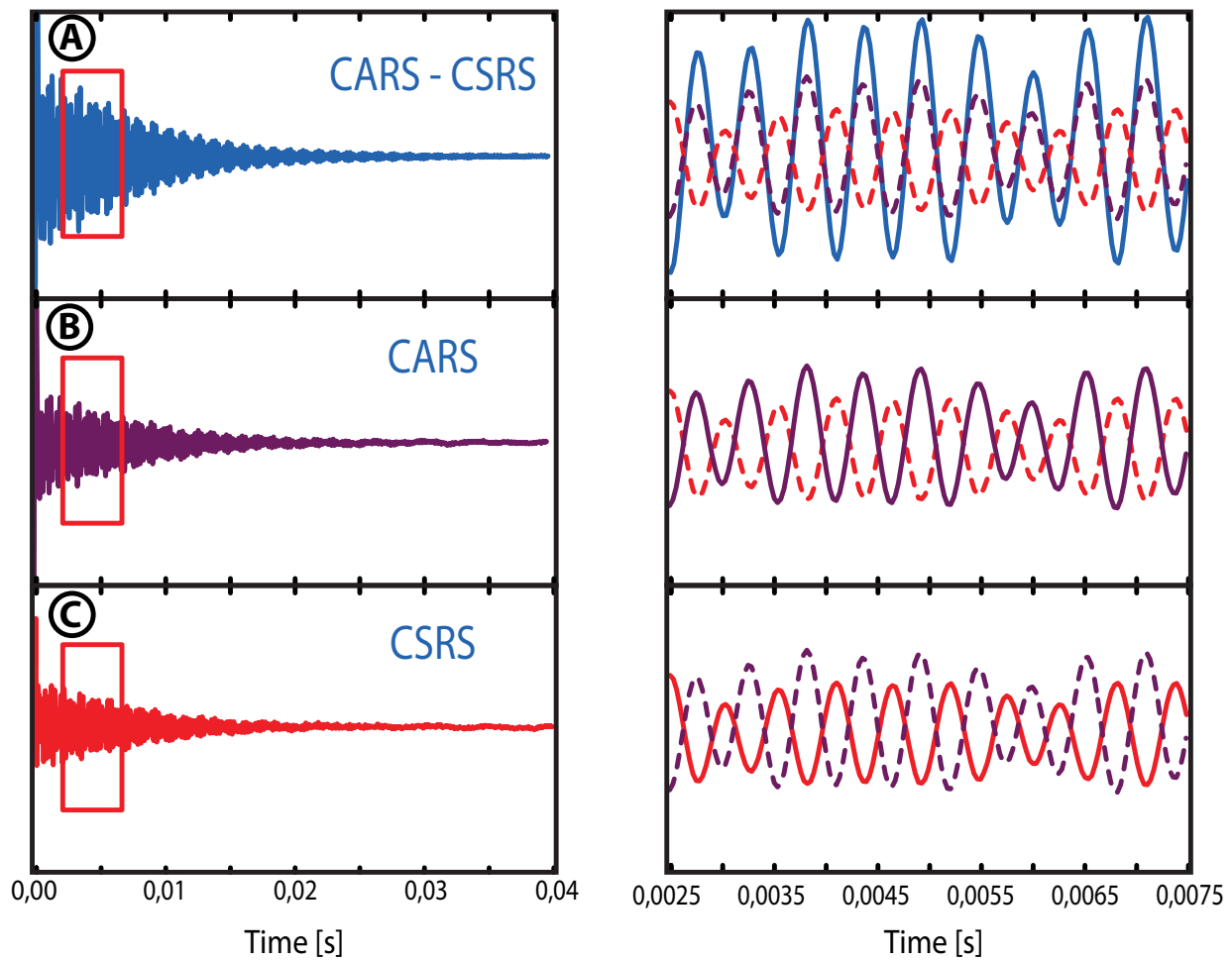
### Experimental Setup

Figure 4.10 sketches the experimental setup used for the differential detection experiment. One of the Titanium Sapphire lasers described in Section 4.2 (Synergy-20UHP, Femto-lasers, 20 fs pulses, repetition frequency of 100 MHz, central wavelength at 793 nm and an average power of 1,1 W) is used as light source. A scanning Michelson interferometer generates pairs of pulses with a linearly varying time delay, emulating a dual-comb experiment, but excluding effects due to e.g. slight differences in the laser parameters. The home-built Michelson interferometer consists of a pellicle beamsplitter and two hollow cube corners, one of them being mounted on a motorized linear translation stage. The beam of a narrow-line width continuous-wave Ytterbium-doped fiber laser (Rock, NP Photonics) at 1040 nm ( $9615 \text{ cm}^{-1}$ ) is passed through the Michelson interferometer

together with the Titanium Sapphire beam. The interferogram of such a monochromatic source is sinusoidal and its zero-crossings serve as clock frequency to sample the Raman interferometric signal at evenly-spaced optical retardations. At a speed of the linear stage of  $5\text{ cm/s}$ , the clock frequency is around 96 kHz. At the output of the Michelson interferometer, in the beam path of the Titanium Sapphire laser, a pair of chirped mirrors (Layertec) precompensates roughly and two fused silica wedges precompensate finely second-order dispersion of the optics. A combination of long pass and short pass filters (750 and 835 nm,  $13333$  and  $11976\text{ cm}^{-1}$ ) before the sample limit the spectral bandwidth of the pulses to improve rejection of the fundamental beam in the detection of the red-shifted and blue-shifted signals. Using a lens of 8 mm focal length, the pulses are focused in the liquid sample (neat hexafluorobenzene), in a 1 mm long cuvette. The total incident average power at the sample is 260 mW. To collect the blue-shifted anti-Stokes radiation, a short pass filter (750 nm-  $13333\text{ cm}^{-1}$ ) is placed in front of one of the two Si photodiodes of a 125 kHz-bandwidth auto-balanced photodetector (Nirvana, Newport). The beam reflected by the short pass filter is filtered by a long pass filter (835 nm-  $11976\text{ cm}^{-1}$ ) and focused onto the second photodiode of the balanced photodetector. Tilting the filters makes it possible to tune their cut-off wavelengths and to optimize the balanced detection. The signal of the differential photodetector is low pass filtered and sampled at a rate determined by the clock frequency (96 kHz) by a 16-bit data acquisition board (Alazartech). The phase shift between red and blue shifted light slightly depends on the dispersion of the incident pulses. A chirped pulse introduces an additional phase shift between Stokes and anti-Stokes. In practice, fine tuning of the phase-shift is achieved by simultaneously monitoring the Stokes and anti-Stokes interferograms and optimizing the amount of dispersion with the translation of the wedges in the beam path before the sample.

### Recorded Interferograms

Figure 4.11 displays the measured interferograms corresponding to Stokes (Figure 4.11C), anti-Stokes (Figure 4.11B) and differential (Figure 4.11A) signal. They are displayed as a function of the measurement time, which can be converted to the optical delay by division with the downconversion factor  $d = 2v/c$ . The interferograms are measured within 4 s: they result from the averaging of 100 interferograms, each measured within 40 ms. The three interferograms are acquired sequentially, first one or the other photodiode is blocked and then the balanced detection is employed. Each interferogram comprises 4096 samples. A maximum optical delay of 14 ps leads to a spectral resolution of 120 GHz, corresponding to a measurement time of  $\sim 42$  ms, taking the used triangular window function into account. As expected, similar interference patterns are observed for the Stokes (Figure 4.11C) and anti-Stokes (Figure 4.11B) interferograms. Each inset in Figure 4.11 is a zoom into the corresponding interferogram trace. The opposite phase in the two interferograms appears in the comparison of the interferogram traced in Figure 4.11B and Figure 4.11C. The differential interferogram is shown Figure 4.11A. The



**Figure 4.11:** Interferograms of the **A** differential signal between Stokes and anti-Stokes signals **B** anti-Stokes signal (CARS) and **C** the Stokes signal (CSRS). The dashed lines in **B** and **C** indicate the respective alternative type of scattering (e.g. CARS for CSRS). In **A** the dashed lines correspond to CARS (purple) and CSRS (red).

enhancement of the signal-to-noise ratio is already obvious in the comparison of the interferograms: the differential interferogram exhibits more pronounced interferometric modulation for short optical delays and is free of the low frequency noise that dominates the Stokes and anti-Stokes interferograms for longer optical delays.

### Differentially Measured Spectra

Fourier transformation of the interferograms reveals the spectra. They are plotted in Figure 4.12 corresponding to the differential, the anti-Stokes and the Stokes shifted signal. To suppress nonresonant contributions, the interferograms are time windowed before Fourier transform, which excludes the small optical delays. The spectral span covers about  $1300\text{ cm}^{-1}$  with a resolution of  $4\text{ cm}^{-1}$  (120 GHz) using a triangular window function. In all spectra, three Raman lines of hexafluorobenzene are observed at 369, 442 and  $559\text{ cm}^{-1}$ . Stokes and anti-Stokes spectra exhibit low-frequency narrow-linewidth noise that could not be assigned to spectral transitions. Such noise is efficiently suppressed in the differential spectrum. The signal-to-noise ratio of the strongest hexafluorobenzene transition at  $559\text{ cm}^{-1}$  is determined as the intensity of the line divided by the root-mean-square noise in the  $800\text{-}1000\text{ cm}^{-1}$  region ( $SNR_X = X(559\text{ cm}^{-1})/\sigma(X(200 - 350\text{ cm}^{-1}))$ ). The signal-to-noise ratios calculate to 770, 470 and 1520 in the Stokes, anti-Stokes and differential spectra, respectively. Therefore the enhancement of the signal-to-noise ratio due to differential detection is around 2. Investigating the noise in the  $200 - 350\text{ cm}^{-1}$  region reveals that, for the same intensity of the  $559\text{ cm}^{-1}$  line, the root-mean-square values of Stokes anti-Stokes and differential detection calculate to 1, 2,1 and 0,28. The differential measurement technique seems to be particularly efficient in suppressing low-frequency common noise due to the femtosecond laser.

### Summary Differential Coherent Raman Spectroscopy

Using a differential detection proved to increase the signal-to-noise ratio considerably. It can be attributed to the cancellation of common noise on the detectors, which is originating from the laser source. This capability of noise cancellation may prove to be particularly important if femtosecond fiber lasers are used, as these usually exhibit a noise spectrum which is broader (and extending towards higher frequencies) than that of solid-state mode-locked lasers. The possibility of a differential detection also clearly shows the  $\pi$  phase shift between Stokes and anti-Stokes.

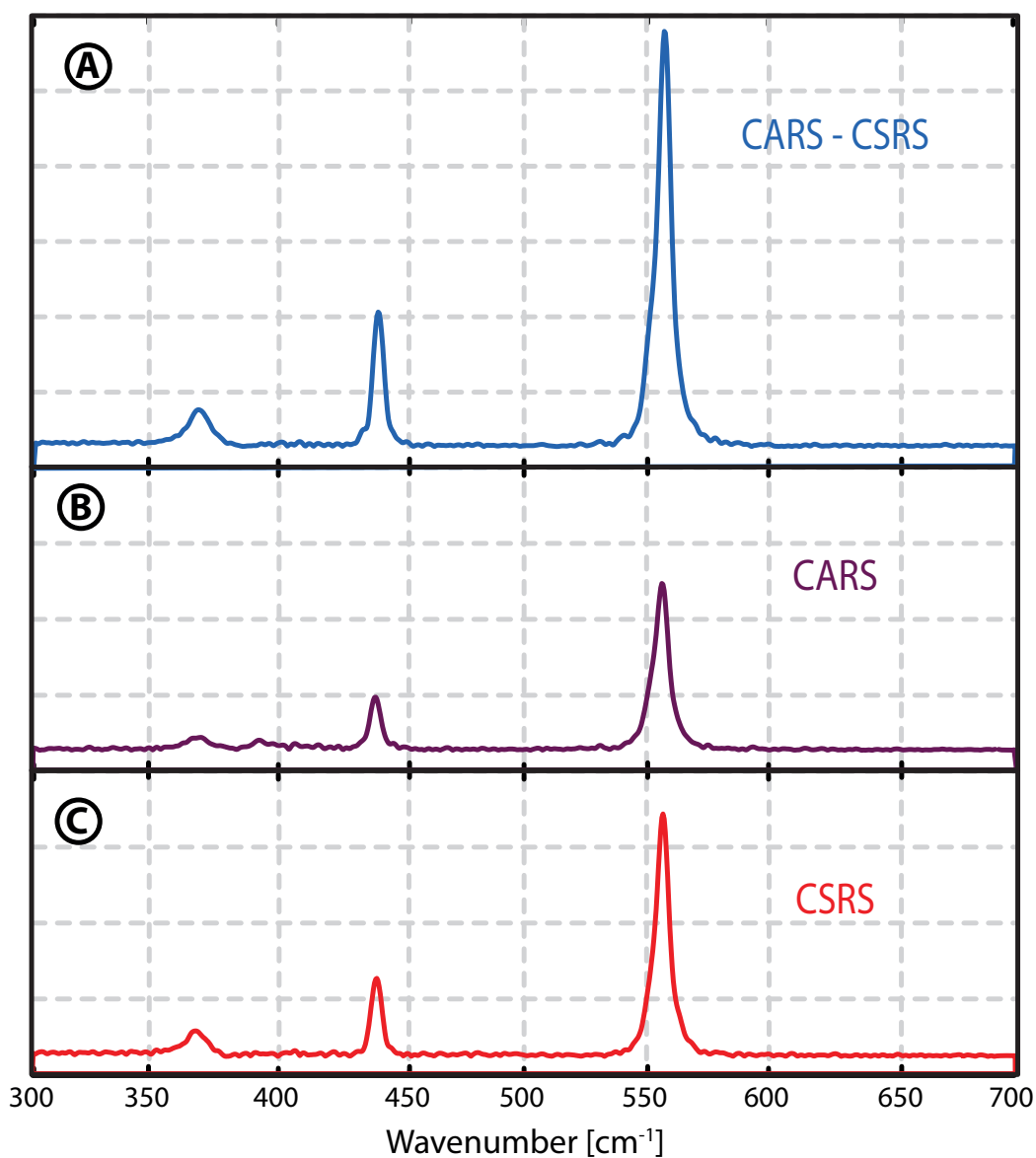


**Figure 4.12:** Raman spectra of the differential spectrum between Stokes and anti-Stokes interferogram signals (A), anti-Stokes signal (CARS) (B) and Stokes signal (CSRS) (C). The differential spectrum shows a improvement of the signal-to-noise ratio. It accounts to more than a factor of two which is owed to the cancellation of common noise by the differential detection.

## 4.5 Asymmetric Coherent Anti Stokes Raman

*Related Article (in preparation):*

*Heterodyne dual-comb coherent anti-Stokes Raman spectroscopy*

*M. Yan, C. Lafargue, S. Holzner, T. W. Hänsch and N. Picqué*

*Contribution: Layout and setup of the system as well as experimental work together with M. Yan and C. Lafargue.*

A significant problem of dual-comb CARS spectroscopy is the dead time between consecutive interferograms. The measurement time is generally much shorter than the refresh time between the interferograms. If the molecular decay time is smaller than the separation between two consecutive pulses (i.e.  $1/(f_{rep})$ ) a dead time is introduced, in which no useful information can be gathered (see Section 2.2.2). The molecular decay time is on the scale of picoseconds, typically  $\sim 1/120 \text{ GHz} = 8,3 \text{ ps}$  for a liquid sample. The time gap between perfect overlap of two pulses to the next perfect overlap is, in the case of about 100 MHz repetition frequency, 10 ns. It takes  $1/\Delta f$  for the delay between pulses of a pulse pair to reach this value. This yields a ratio of useful to wasted time of 1200 or a duty cycle of  $\sim 0,1$  percent, which is doubled if a two sided interferogram is used to 0,2 percent. For a single acquisition this is not a problem but if the experiment needs more than one consecutive measurement, this dead time significantly slows down the data acquisition. This can be the case if averaging is needed for signal-to-noise improvement or in imaging. To reduce the dead time in between the bursts, different techniques can be deployed. For example, a rapid variation of the difference in repetition rate as in [173] can be used. This technique is implemented using an intra cavity piezo to rapidly change the repetition rate of the laser system. It resulted in a reduction of the refresh time by a factor of 50, but the gained spectra are not stable in the sense that, at the time of recording the difference in repetition rate is not always exactly the same. Thereby the spectral axis is changed from shot to shot, which leads to a breathing motion of the spectra (see Section 2.2.3). Most likely this is caused by the very rough implementation in combination with a piezo not suited for this purpose (the piezo is rather slow see Section 4.2, therefore a step signal leads to overshoots).

Another approach is to replace both lasers with high repetition rate laser systems, increasing the repetition frequency while keeping the desired downconversion factor constant by appropriately adjusting the difference in the repetition rate. Using a laser system with, for example, 1 GHz repetition rate instead of 100 MHz improves the duty cycle ( $DC = \tau_{molecular} d \Delta f = \tau_{molecular} \Delta f^2 / f$ ), by a factor of 10 to  $\sim 1$  percent. This process of increasing the repetition rate can be kept on: 10 GHz leads to  $\sim 10$  percent and 100 GHz to a duty cycle of almost 1. For a duty cycle of one the repetition rate has to match the desired optical resolution, i.e. a 120 GHz repetition rate is needed for a desired optical resolution of 120 GHz. In this case the interferogram fills half of the refresh time  $1/2\Delta f$ .

Apart from the technical difficulties in realizing a laser system with such a high repetition rate (recent new developments are pioneering for such systems e.g. [?, 174], but they are still far from being turn-key), another fundamental problem arises. This approach, while straight forward, faces the problem that CARS is a third order nonlinear process and hence dependent on the intensity cubed. If a laser system with e.g. 10 times higher repetition rate would be used but otherwise same parameters (e.g. pulse duration and average power) the peak intensity of the pulses would be 10 time lower and the CARS signal decreases by a factor of 1000.

This severe loss of CARS signal can be mitigated by using one high and one low repetition frequency laser. The usage of the word asymmetric in all of this thesis refers to this asymmetry in repetition rate if not stated explicitly different. In our case a 1 GHz and a 100 MHz laser system is used. If a high  $f_{rep_h}$  and a low  $f_{rep_l}$  repetition laser are used, with the high repetition rate being an even multiple of the low repetition rate i.e.  $f_{rep_h} = n f_{rep_l}$ , the pulses of both lasers overlap for every pulse of the low repetition rate laser and every  $n$ th pulse of the high repetition rate laser. If the high repetition rate is slightly detuned  $f_{rep_h} + \Delta f = n f_{rep_l} + \Delta f$  every pulse from the low repetition rate laser and every  $n$ th pulse of the high repetition rate laser do not overlap perfectly anymore but have a small delay relative to each other. This delay is  $\tau = (1/n)(\Delta f / f^2)$ . The system, high and low repetition rate laser, behaves similarly to two low repetition rate systems with a difference in repetition rate of  $\Delta f / n$ . Since the pulses of the high repetition rate system appear ten times more often  $\tau$  has to grow only to  $1 / f_{rep_h}$  and not to  $1 / f_{rep_l}$  compared to the case when two low repetition rate system are used. Therefore the time between perfect overlap to perfect overlap is shortened by  $1/n$ .

The relative timing between two 100 MHz systems and a GHz and a 100 MHz system is illustrated in Figure 4.13. In the case of two 100 MHz systems, with repetition rates of 100 MHz and  $100 + \Delta f$  MHz corresponding to the two blue traces in Figure 4.13, the delay between the pulses of a pulse pair has to grow to 10 ns for the a perfect overlap to occur. In the case of a 100 MHz and a  $1 + \Delta f$  GHz laser, corresponding to the red and the bottom blue trace in Figure 4.13, starting from perfect overlap the delay between the pulses of a pulse pair has to grow only to 1 ns for the next perfect overlap to occur again. Therefore, interferograms appear 10 times more often for a 100 MHz and a GHz system compared to the use of two 100 MHz systems.

### Experimental Realization

Figure 4.14A outlines the setup of the asymmetric CARS setup, which ,in principle, is the normal CARS setup but one of the laser systems is replaced with a high repetition rate system. One source is a mode-locked Titanium Sapphire laser (Taccor from Giga optics) which delivers femtosecond pulses at a repetition rate of about 1 GHz. These pulses are spectrally centred at 810 nm ( $12345 \text{ cm}^{-1}$ ) with an initial pulse duration of about 40 fs and a chirp of  $\sim 450 \text{ fs}^2$ . After being compensated by two chirped mirrors (Layertec),

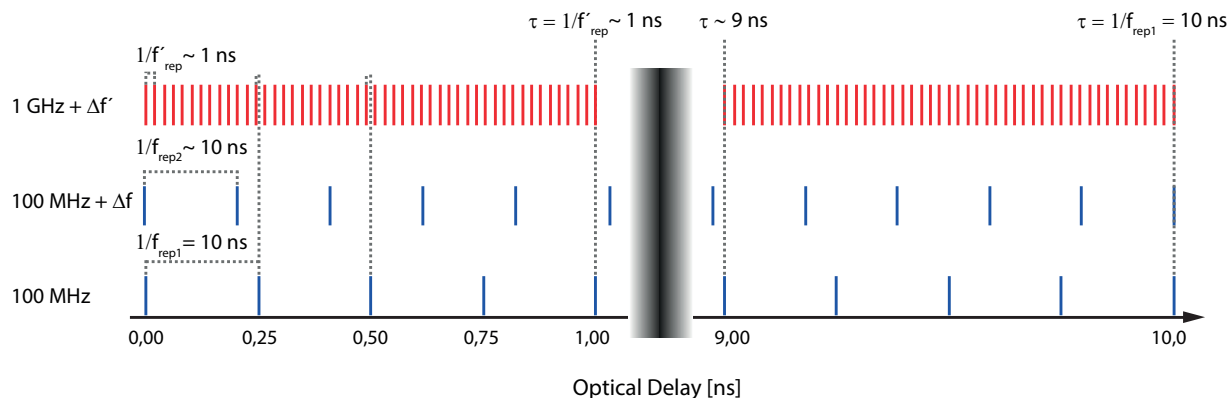


**Figure 4.13:** The relative timing between two MHz systems, at repetition rates 100 MHz and  $100 + \Delta f$  MHz, and a GHz system with repetition rate  $1 + \Delta f$  GHz. Every pulse of the two MHz systems forms a pulse pair while for a MHz and a GHz system only every tenth pulse of the GHz and every pulse of the MHz system form a pulse pair.  $\tau$  indicates the delay between pulses from the 100 MHz and the  $1 + \Delta f$  GHz system.

the pulse duration is compressed to 15 fs (measured using the SPIDER-system from Vteon). The second laser is another Titanium Sapphire mode-locked laser (Synergy-20UHP, Femtolasers) operating at a repetition rate of about 100 MHz. It has a pulse duration of 20 fs and the central wavelength at 795 nm ( $12578 \text{ cm}^{-1}$ ). After combining the two laser beams on a beam splitter, a chirped mirror compressor (Layertec) is used to pre-compensate second order dispersion induced by the optical components of the setup. The combined beams are focused with a lens of 20 mm focal length in a liquid sample inside a 1 mm long cuvette. The maximum available incident powers at the sample are 590 mW from the pump laser and 610 mW from the probe laser. Spectral filters are applied to isolate the CARS signal together with the heterodyne field. A long-pass filter (ET750LP, cutoff 750 nm; Chroma Technology) is placed before the sample and a short-pass filter (3RD740SP, cutoff 740 nm; Omega Optical Inc.) is used after the sample. The anti-Stokes radiation is forward-collected and focused on a silicon photodiode with a bandwidth of 100 MHz. The output signal of the photodiode is low-pass filtered to 50 MHz to avoid aliasing, and then amplified and digitized with a 16-bit data acquisition board (ATS9462; Alazartech) at a sampling rate of 180 MS/s.

### Asymmetric Recorded Interferograms

A recorded interferogram trace, consisting of evenly spaced consecutive interferograms, is plotted in Figure 4.14B for the case of two low repetition frequency systems (blue) and a high and a low repetition frequency laser (red). The downconversion factor  $d$  is the same for both cases and the respective differences in the repetition rates are 50 and 500 Hz. The

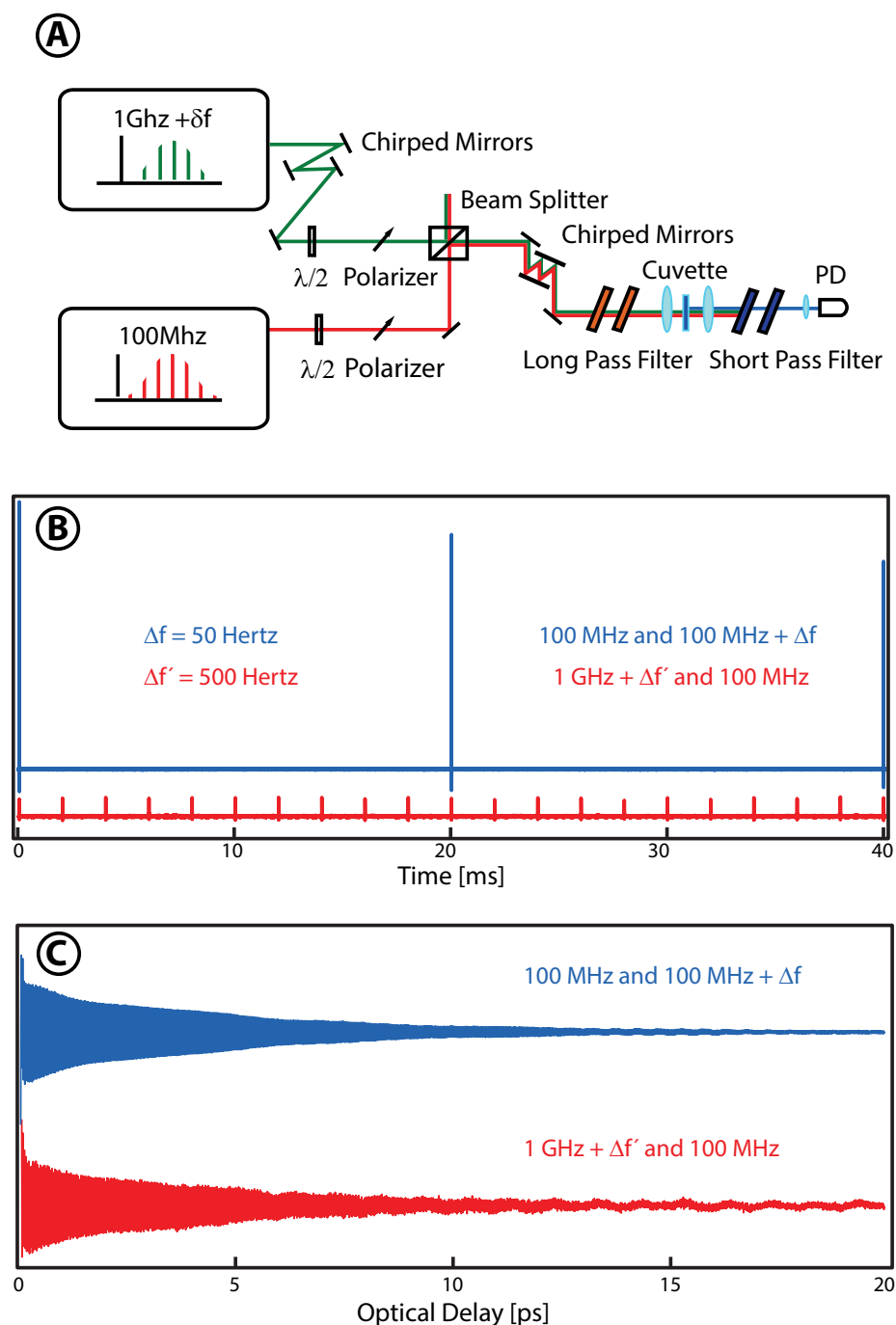


**Figure 4.14:** **A** Experimental setup for asymmetric dual-comb CARS spectroscopy. **B** Interferogram traces recorded in an asymmetric (red) and conventional way (blue). Clearly the asymmetric trace shows an increase in the number of interferograms or in other words a reduction of the dead time. **C** A zoom into one of the interferograms. Again the interferogram recorded in an asymmetric way is red and the conventional is blue. Both interferograms have the same oscillatory period on the same decay constant. The interferogram recorded in an asymmetric way shows less pronounced fringes and an increased noise at longer optical delay.

respective refresh rates are then 20 and 2 ms, clearly showing the improvement in dead time. In the asymmetrically recorded trace 10 times more interferograms appear, but with a reduced signal strength. In Figure 4.14C a zoom into an interferogram recorded with identical (blue) and strongly different repetition rate (red) lasers is plotted. Both traces have the same oscillation frequency, in this case benzene was used as sample with only one Raman transition, and the same decay time but in the interferogram recorded with asymmetric repetition frequency systems the interferogram fringes are less pronounced and the interferogram is more noisy. It is the direct consequence of the fact that the high repetition frequency laser has almost ten times less pulse energy and peak intensity.

### Asymmetric Recorded Spectra

Fourier transformation of such two interferograms leads to the spectra plotted in Figure 4.15. The graph plotted in blue is the Fourier transform of the interferogram employing two similar repetition frequency lasers and the one in red is the Fourier transform of the interferogram recorded with strongly different repetition frequencies. In this case a mixture of four different solvents: perfluorobenzene, nitrobenzene, toluene and nitromethane serves as sample. The difference in repetition rate is set to 10 and 100 Hz for the identical and asymmetric repetition frequency systems respectively. The spectra extend over a range from  $200\text{ cm}^{-1}$  to  $1400\text{ cm}^{-1}$  and have a resolution of  $8\text{ cm}^{-1}$ , taking the employed triangular window function into account. In this direct comparison the loss in signal intensity becomes more apparent than in the interferograms. The signal-to-noise ratio for the blended line at  $1000\text{ cm}^{-1}$  is 915 for the spectrum gained with similar repetition frequencies and 86 for asymmetric repetition frequencies. This factor of 10,6 between the signal-to-noise ratios of both schemes is slightly worse to what can be expected under the assumption of a heterodyne detection from the reduced peak power of the GHz system compared to the MHz system.

### Power Dependence

To clarify which of the lasers acts as pump and which as probe, a power dependence measurement is taken. As sample benzene is used as it has only one Raman transition in the band covered by the laser systems, which facilitates data analysis significantly. Pump and probe intensity are varied and the peak height of the Raman transition in benzene is measured in dependence. In this way two data sets have been obtained. They are plotted as a function of the respective pulse energies on a log-log plot in Figure 4.16, fitted and the slope determined. Two data sets are shown with blue and purple circles for pump and probe respectively and the according (linear) fits in orange and red. The slope determined for the pump power dependence is 1,06 which agrees very well with the predicted slope of 1 (see Equation 4.8). For the probe a slope of 2,45 is determined. The reason for this discrepancy is that besides the heterodyne signal (the second term

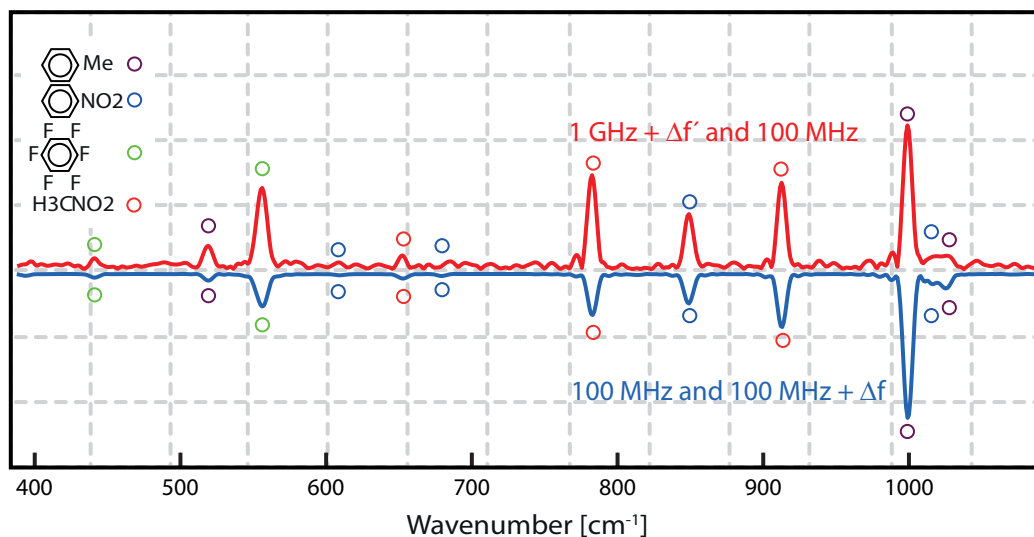


**Figure 4.15:** CARS spectra gained by Fourier transform of an interferogram recorded in an asymmetric way (red) and in a conventional way (blue). The sample was a mixture of four different solvents: toluene, nitrobenzene, nitromethane and perfluorobenzene. Both spectra have been normalized to unity. The red spectrum has a higher noise than the blue spectrum, nevertheless the transitions can be assigned clearly.

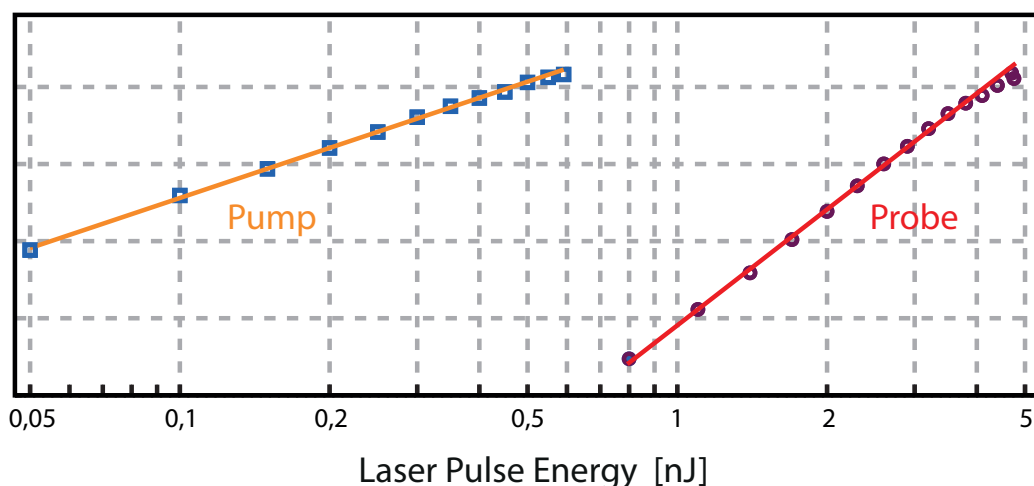


**Figure 4.16:** Dependence of the CARS signal on pump (blue squares) and probe (purple circled) power and linear fitting functions (respectively orange and red line). Slopes of 1.07 and 2.49 indicate linear and quadratic dependence on the pump and probe power. As sample neat benzene is used.

on the right of Equation 4.10) the signal not containing any heterodyne contribution is generated (the first term in Equation 4.10):

$$S \propto \chi_{CARS}^2 I_{pump}^2 I_{probe} + \chi_{CARS}(\chi_{CARS} + \chi_{NR}) I_{pump} I_{probe}^2 \quad (4.10)$$

If  $I_{probe}$  becomes small the contribution of the first term becomes significant and the power dependence deviates from the predicted slope of 2.

### Summary Asymmetric Coherent Anti Stokes Raman

The approach of taking one high and one low repetition rate laser system allows to increase the duty cycle while at the same time avoiding the nonlinear penalty in power dependence of the signal by using a heterodyne detection. This is an influential factor if dual-comb CARS is used e.g. in an imaging setup where the dead time significantly reduces the applicability of this technique.

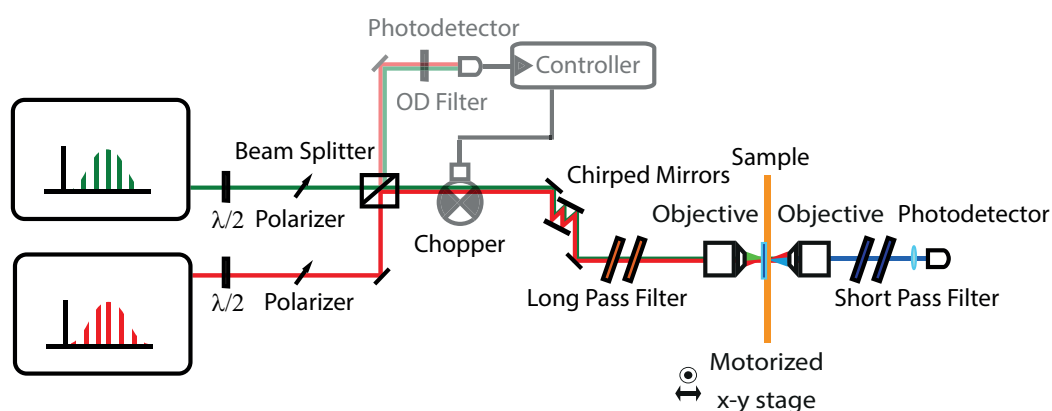


**Figure 4.17:** Experimental set-up for dual-comb CARS spectro-microscopy. The focusing lens is replaced with a NA = 0,45 microscope objective and the cuvette holding the sample with a microcapillary plate, mounted on a x,y stage, compared to the CARS spectroscopy setup. A chopper wheel can be inserted into the beam path to reduce the average power. OD filter, optical density filter.

## 4.6 Coherent anti Stokes Raman Imaging

*Related Article*[159]:

*Coherent Raman spectro-imaging with laser frequency combs*

*T. Ideguchi<sup>†</sup>, S. Holzner<sup>†</sup>, B. Bernhardt, G. Guelachvili, N. Picqué, and T. W. Hänsch*

<sup>†</sup> *These authors contributed equally to this work*

*Contribution: Layout and setup of the system as well as experimental work together with T. Ideguchi. Discussed the manuscript.*

The very fast acquisition times for a single interferogram, e.g.  $\sim 15 \mu\text{s}$  as described in Section 4.2, allow spectrally resolved imaging.

### Experimental Setup

Only minor changes to the setup described in Section 4.2 have to be made, it is outlined in Figure 4.17. The laser sources and the filter setup are identical: two 100 MHz sources at  $\sim 17$  fs pulse duration, a long pass filter (Chroma Technology, ET750LP) before the sample and a short pass filter (Omega Optical Inc., 3RD740SP) after the sample to strip off the fundamental light. The focusing lens is replaced by a microscope objective (Olympus LCPLN20XIR, NA = 0,45), focusing the incident beams to a focal spot of  $1,9 \mu\text{m}$  diameter with a Rayleigh length of  $3,4 \mu\text{m}$ . The cuvette is replaced with a micro capillary plate with  $25 \mu\text{m}$  diameter holes and a thickness of  $500 \mu\text{m}$  filled with a mixture of equal amounts

of perfluorobenzene, nitromethane and toluene. It is positioned on a x-y stage (Thorlabs, MLS203), which raster scans the sample in  $1\ \mu\text{m}$  steps. The signal is measured with a home built amplified silicon photodetector. Then electric signal is amplified to the most favourable input voltage range for the digitizer by a wideband variable gain voltage amplifier (FEMTO Messtechnik GmbH, DHPVA-100) and digitized with a 180 MS/s, 16-bit data acquisition board (Alazartech, ATS9462).

The difference in repetition frequency is set to 50 Hz and the incident laser power to 380 mW. To reduce this high average power a chopper wheel can be inserted into the beam path. Depending on the closed to open ratio of the chopper wheel the average power reduces, e.g. if this ratio would be 2 percent the total average power on the sample is reduced to 2 percent of the incident power. The chopper wheel is synchronized to the acquisition by taking linear dual-comb interferograms from the other exit of the beam splitter as trigger for the chopper wheel controller. The controller allows giving a certain phase offset to the chopper signal and hence to time the opening of the chopper in the incident beam with the acquisition. Opening the window of the chopper only close to the perfect overlap of the pulses reduces the average power without any loss of CARS signal intensity. The reason is that only close to the perfect overlap useful information can be gathered, the larger the duty cycle (see Section 4.5) the larger the opened time of the chopper has to be. In this case the duty cycle is less than 1 percent, closing the window of the chopper at times apart from the perfect overlap therefore means no loss in information.

### CARS Image

For this measurement no chopper wheel is inserted into the beam path as the image is acquired. The sample, a micro capillary plate, withstands a high average power easily. Nevertheless this technique is tested in the same setup with the acquisition of a single spectrum with and without chopper. The two acquired spectra are found to be identical. Using the stage, a 45 times 45  $\mu\text{m}$  image is acquired. Each pixel ( $1\ \text{px} = 1 \times 1\ \mu\text{m}$ ) has a measurement time of 12  $\mu\text{s}$  which leads to a resolution of  $\sim 300\ \text{GHz}$ , including the triangular window function used. Due to the dead time between the interferograms the total acquisition time is 40,5 s for the whole image. Fourier transform of the interferograms leads to a spectral cube. Each pixel corresponds to an entire spectrum spanning from  $\sim 180\ \text{cm}^{-1}$  to  $\sim 1400\ \text{cm}^{-1}$  (see Figure 4.18). Despite the very short measurement time of a single pixel the Raman transitions are clearly visible in the spectrum. They can be assigned unambiguously to the used sample mixture. For an imaging setup this high signal-to-noise ratio is more than sufficient, making a further reduction of the measurement time possible.

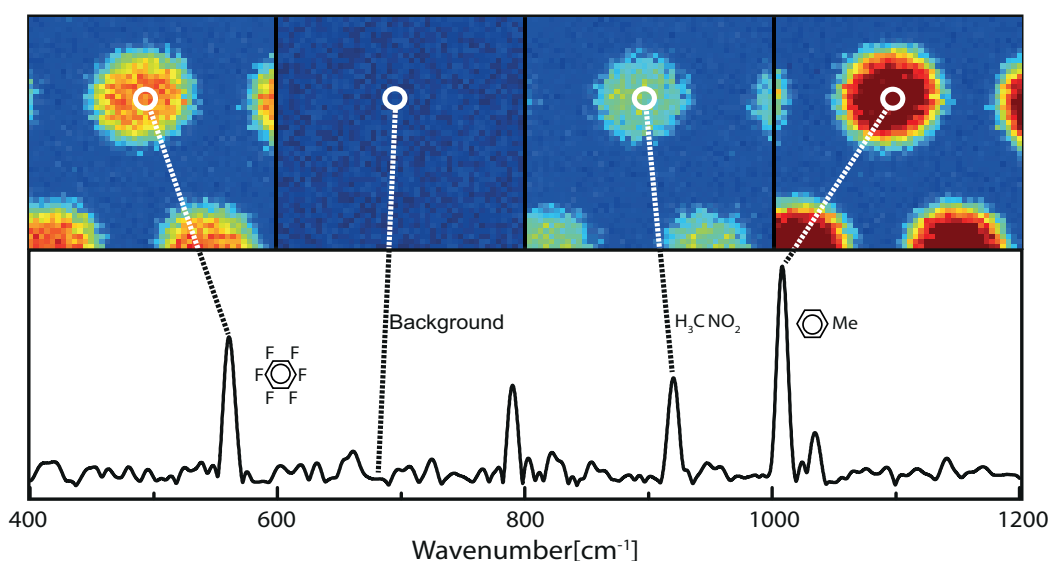


**Figure 4.18:** Spectral image of a capillary plate with holes filed with a mixture of equal amounts of (perfluorobenzene, nitromethane and toluene). For each of the 2025 (45x45) pixel positions a spectrum is acquired within  $12 \mu\text{s}$  and a windowed resolution of  $10 \text{ cm}^{-1}$ . The spectrum shown on the bottom corresponds to pixel (21,16). Each element of the spectral cube may be plotted as an image similar to the four displayed ones. An image corresponds to the spectral intensity at a fixed wavenumber for all pixels. It provides information about the spatial distribution of a compound. A distinguishable spectral signature allows identification of a given compound as indicated.

### Summary Coherent anti Stokes Raman Imaging

This technique combines fast acquisition with a broad spectral coverage and a good spectral resolution. Generally these are features hard to combine in a coherent Raman scattering microscope. Most fast acquisition techniques feature a good spectral resolution but are limited to a single Raman transition or a couple of transitions [139, 140, 141], whereas this technique allows to cover a band of  $\sim 1200 \text{ cm}^{-1}$ . On the other hand, broadband techniques usually suffer from long acquisition times [142, 175] (50 ms for  $180 \text{ cm}^{-1}$  in [175] compared to  $1200 \text{ cm}^{-1}$  and  $12 \mu\text{s}$  for this technique). The acquisition time of this technique could be improved further if the asymmetric CARS technique described in Section 4.5 is employed. Broadening of the fundamental light might make it possible to cover the entire band from 0 to  $4000 \text{ cm}^{-1}$  and thereby cover all fundamental molecular transitions (except for hydrogen fluoride).



# Chapter 5

## Conclusion

In the framework of this thesis two different approaches of investigating molecular vibrational transitions have been explored. They are based on either the direct interrogation of molecular transitions in the mid-infrared or on the nonlinear response of molecules to visible/near infrared light in the form of coherent Raman scattering. In this chapter the results of these efforts are summarized.

The first experiment to mention is the development and characterization of two singly resonant optical parametric oscillators. Those oscillators emit nearly transform limited few cycle pulses in the mid-infrared, harnessing ultra-short pulse Titanium Sapphire lasers as pump sources. They allow not only linear techniques to be exploited but also nonlinear techniques as well. The output spectrum is smooth over the whole tuning range of more than  $\sim 1500$  nanometers, which allows a total spectral coverage from  $\sim 2000$  to  $\sim 4500$  nanometers. The output power is in the range of milliwatts to tens of milliwatts, more than enough for linear spectroscopy in this region and even enough to enable nonlinear frequency conversion, spectral broadening and nonlinear spectroscopy.

To allow efficient nonlinear broadening of the spectrum as long as possible nonlinear interaction with a suitable medium is needed. In a waveguide light is guided efficiently, strongly confined and a specific dispersion can be engineered, making it a perfect candidate for supercontinuum generation. Oxide based materials as the omnipresent silica are not transparent in the mid-infrared, forcing different materials to be used. The possibility of mid-infrared supercontinuum generation using silicon and chalcogenide glass waveguides was demonstrated. The generated supercontinua span more than an octave for both waveguides. As supercontinuum generation can be sensitive to noise, the coherence properties of the generated supercontinua were tested and found to be excellent.

Concluding the experiments around direct mid-infrared spectroscopy, a first attempt of linear dual-comb spectroscopy using the two optical parametric oscillators was made. As neither the pump sources nor the optical parametric oscillators are stabilized optical

frequency combs, an adaptive sampling scheme was set up, monitoring the fluctuations of the pump sources rather than the fluctuations of the optical parametric oscillators. It was found to be not sufficient to generate a perfectly corrected spectrum.

Experiments using Raman scattering offer an access to molecular vibrational transitions without the need for mid-infrared light; in its coherent version as CARS, Coherent Raman anti-Stokes scattering, it is the second cornerstone of this thesis. Starting out from a very simple spectroscopy setup, different experimental realizations have been investigated, which all work outstandingly well. The spectra generated can be recorded within microseconds with a resolution limited by the natural linewidth of the sample and a spectral span covering  $\approx 1200 \text{ cm}^{-1}$ , including a significant part of the highly characteristic low wave number region. With some minor changes, the setup also proved to be able, to detect the red-shifted radiation CSRS, coherent Stokes Raman scattering, and backward scattered CARS radiation as well.

The Raman experiments conducted suggested a heterodyne mixing between the CARS signal generated by the two different lasers and either fundamental or nonlinearly generated fields. It was taken under scrutiny by power and concentration measurements. They proved the assumption of heterodyne detection to be true, depending on the experimental conditions a mixing with either fundamental or nonlinearly generated fields can be chosen.

The possibility to detect CARS as well as CSRS inspired a setup laid out for differential detection of CARS and CSRS, taking advantage of the 180 degree phase shift concerning the instant of their generation. The differential detection increased the signal-to-noise ratio by more than 3 dB which is attributed to common noise cancellation.

A major obstacle of dual-comb CARS is the dead time between consecutive measurements which was conquered by an asymmetric dual-comb scheme. Two laser sources of strongly different repetition rates, 100 MHz and 1 GHz, are used to decrease the unwanted dead time. Together with a heterodyne detection scheme a strong nonlinear signal decrease can be avoided, while the dead time could be reduced by a factor of 10, a signal loss of just one order of magnitude was observed despite the strong nonlinearity of the CARS signal.

Fast acquisition times allow optical imaging of a sample. A proof of principle experiment has been done using a micro-capillary plate filled with different common laboratory solvents. The technique demonstrated its capability to produce images with excellent chemical resolution, clearly allowing to distinguish between different chemical specimen due to the broad coverage of Raman transitions. It combines, without loss, the advantages of the spectroscopy setup, such as high signal-to-noise ratio, broad spectral coverage and a good resolution, with spacial resolution, which, in this case, was only limited by the resolution of the mechanical stage. The introduction of a controlled chopper wheel allowed reducing the average power to values in the single digit milliwatt range without loss of signal intensity.

# Chapter 6

## Outlook

Since the tools and techniques presented in this thesis are very recent developments they still face challenges and limitations. In this chapter an outlook to the, possible, future development of these tools and techniques is given, on how to improve their capabilities, how to solve associated problems and also attention is drawn to possible future experiments.

Following the same order as in the previous chapter, the first limitation which comes to mind are the stability issues of the optical parametric oscillators. The first and easiest way to tackle this problem is improving the passive stability of the systems. None of the systems is equipped with an acoustic cover. A shielding with acoustically isolating material can reduce fluctuations significantly, in combination with a separated crystal housing the stability will improve even more. Finally, a small laminar gas flow around the crystal not only improves stability further but also prohibits dust and other environment contaminants to settle on the crystal.

Apart from passive stability active stabilization of the system optical parametric oscillator - pump laser is possible. The pump source, a mode-locked Titanium Sapphire laser, can be locked using common techniques, as  $f - 2f$  stabilization, harnessing commercially available components as photonic crystal fibers and crystals. The remaining free parameter, the carrier envelope frequency of either signal or idler, can be stabilized using a piezo actuated mirror in the optical parametric oscillator cavity and a parasitically generated signal, for example the sum-frequency of signal and pump light.

Also, the supercontinua generated in the waveguides can be used to develop a measurement and stabilization scheme of either signal or idler carrier envelope phase. A  $f$  to two  $f$  scheme in the mid-infrared for example could be developed, which can serve as a blue print for different mid-infrared systems.

If no stabilization is employed, the optical parametric oscillator is very well suited for liquid phase experiments. One can imagine a waveguide setup which combines

spectral broadening with sampling. For example a waveguide which broadens the pump spectrum in a first section and probes a sample in a second section, designed to have a strong evanescent field probing in a manner similar to attenuated total reflection.

Also the optical parametric oscillator by itself is well suited for liquid phase experiments. A possible candidate is vibrational circular dichroism, which can reveal the structure of different protein samples in their native environment.

Concerning the Raman experiments a straight forward improvement is an extended coverage to the band from  $\sim 0$  to  $4000\text{ cm}^{-1}$ . It can be achieved by sending the Titanium Sapphire light into a photonic crystal fiber to broaden spectrally and compress the broadband spectrum afterwards [176, 177]. To cover the full band a broadening of a factor  $\approx 2,5$  is needed. First rudimentary experiments in this direction have been made, using only 5 millimetres of photonic crystal fiber, which was already sufficient to broaden the ingoing spectrum by more than a factor of two.

Using a more sensitive detector such as a photomultiplier or an avalanche photodiode could allow to reduce the power on the sample in the imaging setup. A fast optical switch like an acousto-optical modulator additionally gives more control over the open to closed ratio of the beam, again reducing the average power on the sample. A differential detection scheme allows lowering the power on the sample further; as the signal-to-noise is increased an overall lower signal level could be tolerated.

An asymmetric dual-comb scheme employing one high and one low repetition rate laser system on the other hand can reduce the dead time between consecutive measurements significantly. In combination with a rapid variation of the difference in repetition rate this might enable video rate imaging.

Finally, CARS can be combined with several different linear or nonlinear techniques to gain even more information. A prominent example of those techniques is two photon excited fluorescence spectroscopy which has been demonstrated recently [178]

# Chapter 7

## Appendix

### 7.1 List of Abbreviations

The following abbreviations and definitions are used thorough out the thesis with the following meaning, if not stated explicitly different.

$n$	number of round trips of the pulse in the laser cavity
$\varphi(t)$	pulse temporal phase
$\phi(\omega)$	pulse spectral phase
$f \otimes g$	convolution of $f$ and $g$
$\text{III}(\xi)$	III distribution or Dirac comb
$\mathcal{H}(f)$	Hilbert transform of $f$
$\mathcal{F}(f)$	Fourier transform of $f$
$\sigma(\xi)$	Step function

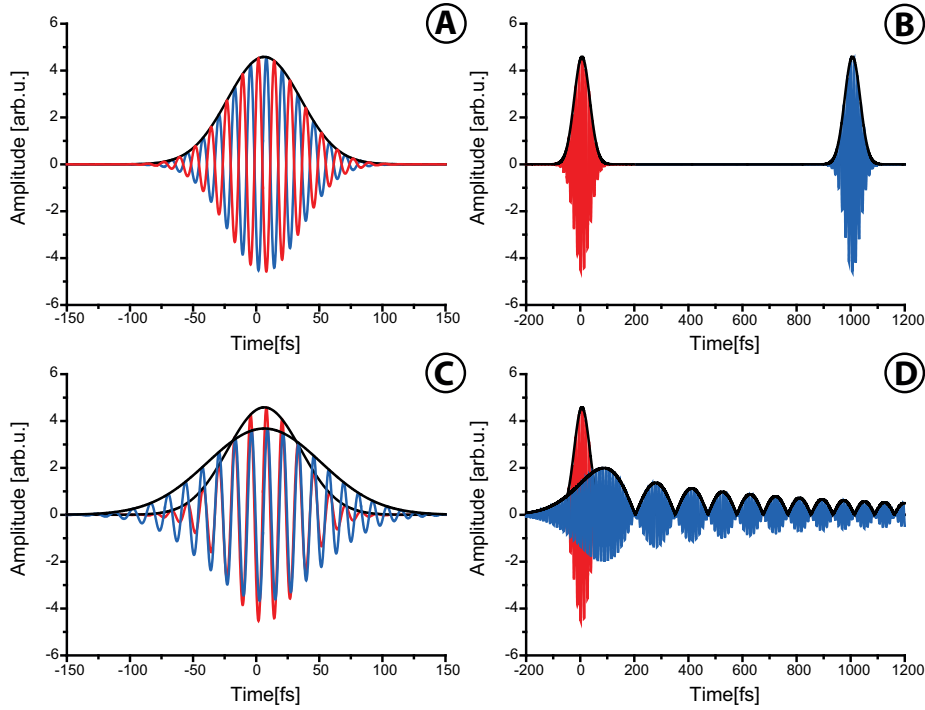


**Figure 7.1:** The effect different terms of the spectral phase expansion have on the electric field of a short pulse. Two pulses are plotted, one of them experienced the phase term (blue) the other one is unperturbed (red). **A** The carrier envelope phase slip **B** The group delay **C** The group delay dispersion **D** The third order dispersion

## 7.2 Dispersion And Phase

The phase transfer function of a material is often unknown in detail or nonlinear, a Taylor expansion is generally used to account for different phase effects. It seems natural to do this expansion in the time domain but it is normally not done. Not only is it hard to measure intensity versus time, which is needed to determine the phase term precisely but it is also more revealing to have a look at the terms of the Taylor series in the frequency domain. In the frequency domain the different expansion orders have their own names and physical quantities can be assigned to them.

$$\phi(\omega) = \phi_0 + \frac{d\phi(\omega)}{d\omega}(\omega - \omega_0) + \frac{d^2\phi(\omega)}{d\omega^2}(\omega - \omega_0)^2 + \frac{d^3\phi(\omega)}{d\omega^3}(\omega - \omega_0)^3 + \sum_i \frac{d^i\phi(\omega)}{d\omega^i} \quad (7.1)$$

The zeroth order is called carrier envelope phase, the first order group delay, the second order group delay dispersion and the third order third order dispersion. The effects of the different terms of the Taylor expansion on an initially unperturbed pulse are illustrated

in Figure 7.1.

The carrier envelope phase shifts the relative timing of the electric field compared to the envelope but does not change the shape of a pulse. In Figure 7.1A the electric field of two pulses having a carrier envelope phase shift of approximately  $\pi$  is shown.

The effect of the second term on the pulse depicted in Figure 7.1B, the group delay means a shift in time of the pulses.

The group delay dispersion (GDD), sometimes also called second order dispersion or often only dispersion, is the first term to change the duration of the pulse in time. Its effect is illustrated in Figure 7.1C. For a phase with all terms being zero except the first two a pulse has its maximally short duration, which is given by the Fourier transform of its spectrum and is therefore often called transform limited. A GDD different from zero means that different wavelength elements of the spectrum arrive at different instants in time, stretching out the pulse. The GDD therefore spreads out the pulse in time but does not change its shape.

The fourth term, often called third order dispersion, not only spreads out the pulse but is the first term to change the shape of the pulse in time. It e.g can create ripples in the front or tail of the pulse as shown in Figure 7.1D.

### 7.3 Carrier Envelope Phase

If higher order dispersive terms are not compensated perfectly, a pulse circulating inside the cavity of a mode locked laser does not look identical after one round trip inside of the laser cavity. During the round trip in the laser cavity, the envelope travels slightly slower than the carrying field. The reason is simply that group velocity  $v_{group}$  and phase velocity  $v_{phase}$  are not equal. Therefore the relative timing of the carrying field to the pulse envelope changes. In terms of phase: the pulse acquires a certain amount of additional phase shift with each round trip in the laser cavity. This additional phase is called the carrier envelope phase slip [179] and can be expressed as the carrier frequency times the difference in round trip times of the carrier field and the envelope in a cavity of length  $l_{cavity}$  modulo  $2\pi$ :

$$\Delta\varphi = \omega_0 l_{cavity} \left( \frac{1}{v_{group}} - \frac{1}{v_{phase}} \right) \text{mod} [2\pi] = \omega_0 l_{cavity} \left( \frac{1}{\frac{c}{n + \omega \frac{dn}{d\omega}}} - \frac{1}{v_{phase}} \right) \text{mod} [2\pi] \quad (7.2)$$

Every round trip the circulating pulse acquires the phase shift  $\Delta\varphi$ .  $\Delta\varphi$  is assumed to be constant, i.e. no influence of noise or similar is taken into account. Equation 7.2 also indicates that for a laser using Kerr lens mode locking, even with perfect compensation of material dispersion in the cavity, the Kerr lensing introduces a phase shift, which is unavoidable as it ensures pulsed operation. A pulse with  $\Delta\varphi$  equaling zero is nevertheless possible, therefore  $\Delta\varphi$  has to be a multiple of  $2\pi$ . Including this additional phase shift, the field of the pulses exiting the laser cavity can be written:

$$E(t) = A(t) e^{i\omega_0 t} e^{i2\pi(\varphi_0 + n\Delta\varphi)} \quad (7.3)$$

with  $n$  as the number of round trips.  $\varphi_0$  is a phase determined on the start up of the laser. It is a constant phase offset, which is assumed to be zero without loss of generality.

## 7.4 The Shah Distribution

The properties of the III distribution are reviewed here shortly. There are three important features of the III distribution concerning its use to describe a frequency comb.

The first important property is that the III distribution is its own Fourier transformed, making it one of the two invariants under Fourier transform.

The second properties of the III distribution concerns its convolution with an arbitrary function  $I(t)$ . It creates a periodic repetition of this function, with a repetition period  $T_{rep}$  as depicted in Figure 7.2A:

$$\sqrt{I(t)} \otimes \text{III}(t - nT_{rep}) = \sum_{n=-\infty}^{\infty} \int_{-\infty}^{\infty} \sqrt{I(t - \tau)} \delta(\tau - nT_{rep}) d\tau = \sum_{n=-\infty}^{\infty} \sqrt{I(t - nT_{rep})} \quad (7.4)$$

The third property is sampling. If a function and the III distribution are multiplied, the function is sampled in evenly spaced intervals given by the spacing of the III distribution, as plotted in Figure 7.2B:

$$\sqrt{I(t)} \text{III} = \sum_{n=-\infty}^{\infty} \sqrt{I(t)} \delta(t - nT_{rep}) = \sum_{n=-\infty}^{\infty} \sqrt{I(nT_{rep})} \quad (7.5)$$

A Gaussian envelope sampled at precisely evenly spaced points reproduces the structure of an optical frequency comb. The comb generated this way nevertheless is always a harmonic comb, meaning that one comb line or comb modes coincides with zero frequency, as shown in Figure 7.2B.

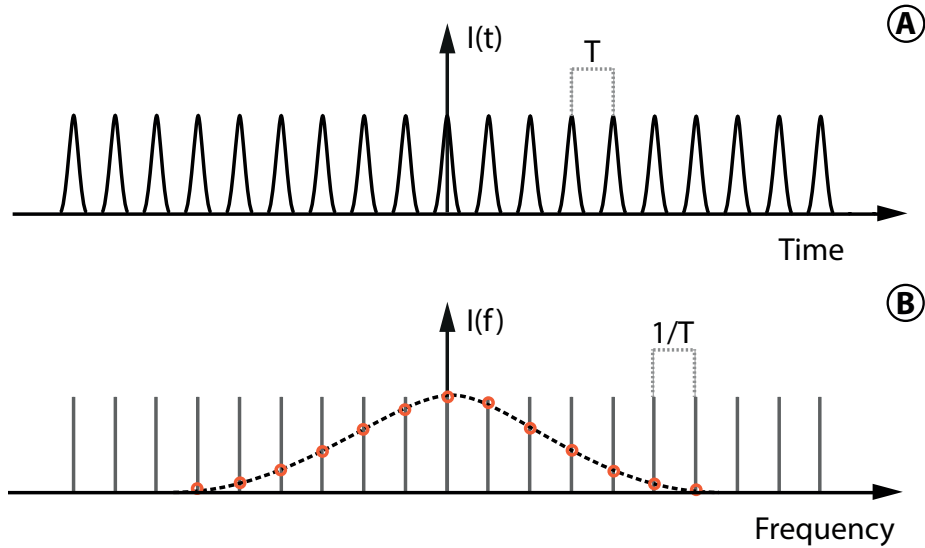


**Figure 7.2:** III distribution convolved with a Gaussian function in time and its Fourier transformation. **A** Time domain representation. A train of evenly spaced pulses with the spacing  $T$  is generated. **B** Fourier transformation of **A**, a III distribution multiplied with a Gaussian function. The Gaussian is sampled at evenly spaced frequency intervals (red circles).

## 7.5 The Optical Frequency Comb and the III Distribution

To complete the physical picture the carrier field underlying the Gaussian envelope and the phase terms have to be added. Due to the carrier envelope phase shift from pulse to pulse the whole comb is shifted in frequency. If this shift is not by chance a harmonic or subharmonic of the repetition frequency  $f_{rep} = 1/T_{rep}$ , no comb mode is lining up with zero frequency. The distance in frequency of the nearest comb mode to zero is called the carrier envelope offset frequency  $f_{ceo}$ . The frequency shift can be understood when evaluating the convolution of the III distribution and the electric field including the carrier envelope phase and the oscillating term:

$$E(t) \otimes \text{III} = \int_{-\infty}^{\infty} E(t - \tau) \sum_{n=-\infty}^{\infty} \delta(\tau - nT) e^{i2\pi(\varphi_0 + n\Delta\varphi)} d\tau = \sum_{n=-\infty}^{\infty} E(t - nT) e^{i2\pi(\varphi_0 + n\Delta\varphi)} \quad (7.6)$$

It produces a pulse train resembling the ideal pulse train plotted in Figure 7.3A. A train of evenly spaced pulses in time with a certain slip between envelope and carrier field from pulse to pulse. How such a pulse train constitutes a frequency comb becomes clear when changing from time to frequency domain. Simple Fourier transformation of Equation 7.6 and use of Poisson's sum rule leads to:

$$\mathcal{F}E(t)\mathcal{F}(\text{III}) = E(\omega) \sum_{n=-\infty}^{\infty} e^{i2\pi n(\Delta\varphi - \omega T_{rep})} = \frac{2\pi}{T_{rep}} E(\omega) \sum_{m=-\infty}^{\infty} \delta\left(\omega - \frac{2\pi m}{T_{rep}} - \frac{\Delta\varphi}{T_{rep}}\right) \quad (7.7)$$

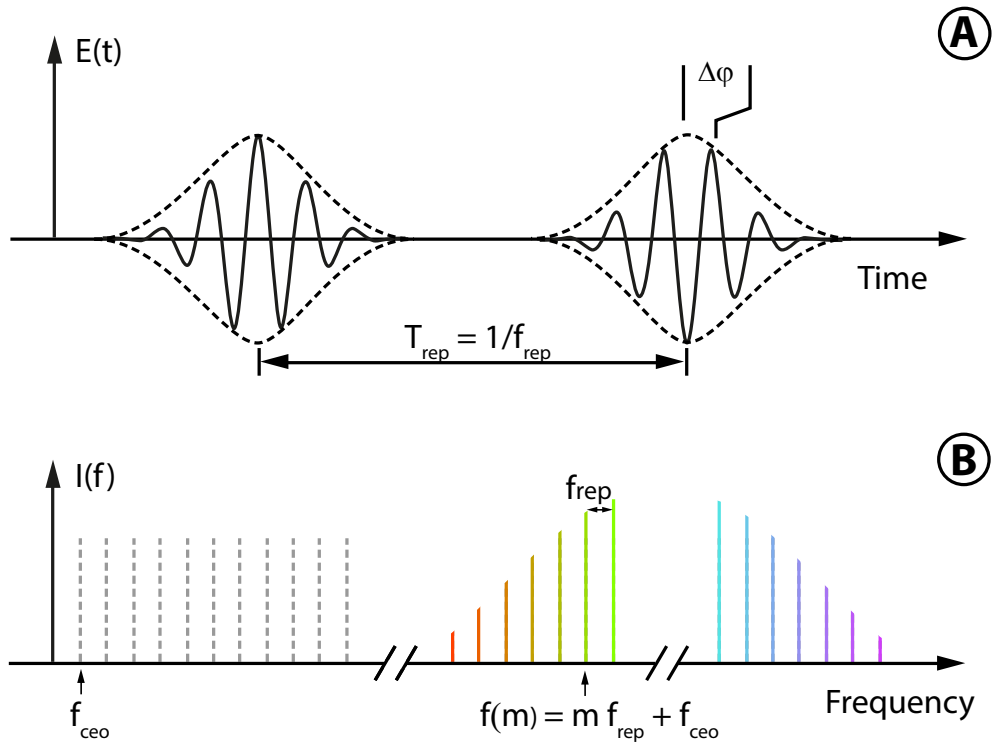


**Figure 7.3:** A Frequency comb in time and frequency domain. **A** Time domain representation. The pulses are separated by the round trip time  $T_{rep} = 1/f_{rep}$ . Consecutive pulses have a different phase relation between carrier field and envelope. It is altered by the amount of carrier envelope phase acquired during one round trip of the pulse in the laser cavity  $\Delta\phi$ . **B** Frequency domain representation. In the frequency domain, a train of pulses with repetition period  $T_{rep}$  forms a comb of evenly spaced modes, separated by  $f_{rep} = 1/T_{rep}$ . Due to the carrier envelope phase slip  $\Delta\phi$  from pulse to pulse the whole comb is offset from zero frequency by a certain amount  $f_{CEO}$ .

# Bibliography

- [1] T. H. MAIMAN. Stimulated optical radiation in ruby. *Nature*, 187(4736):493–494, Aug 1960.
- [2] Ali Javan. Possibility of production of negative temperature in gas discharges. *Physical Review Letters*, 3(2):87, 1959.
- [3] A. Javan, W. R. Bennett, and D. R. Herriott. Population inversion and continuous optical maser oscillation in a gas discharge containing a he-ne mixture. *Phys. Rev. Lett.*, 6:106–110, Feb 1961.
- [4] Fran Adar, Michel Delhayé, and Edouard DaSilva. Evolution of instrumentation for detection of the raman effect as driven by available technologies and by developing applications. *Journal of chemical education*, 84(1):50, 2007.
- [5] JL Koenig. Raman spectroscopy of biological molecules: a review. *Journal of Polymer Science: Macromolecular Reviews*, 6(1):59–177, 1972.
- [6] Theodor W Hänsch. Nobel lecture: passion for precision. *Rev. Mod. Phys*, 78(4):1297–1309, 2006.
- [7] Fritz Keilmann, Christoph Gohle, and Ronald Holzwarth. Time-domain mid-infrared frequency-comb spectrometer. *Opt. Lett.*, 29(13):1542–1544, Jul 2004.
- [8] Albert Schliesser, Markus Brehm, Fritz Keilmann, and Daniel van der Weide. Frequency-comb infrared spectrometer for rapid, remote chemical sensing. *Optics Express*, 13(22):9029–9038, 2005.
- [9] Markus Brehm, Albert Schliesser, and Fritz Keilmann. Spectroscopic near-field microscopy using frequency combs in the mid-infrared. *Optics express*, 14(23):11222–11233, 2006.
- [10] E Baumann, FR Giorgetta, WC Swann, AM Zolot, I Coddington, and NR Newbury. Spectroscopy of the methane  $\nu_3$  band with an accurate midinfrared coherent dual-comb spectrometer. *Physical Review A*, 84(6):062513, 2011.

- [11] Zhaowei Zhang, Tom Gardiner, and Derryck T Reid. Mid-infrared dual-comb spectroscopy with an optical parametric oscillator. *Optics letters*, 38(16):3148–3150, 2013.
- [12] Andreas Volkmer, Lewis D Book, and X Sunney Xie. Time-resolved coherent anti-stokes raman scattering microscopy: Imaging based on raman free induction decay. *Applied Physics Letters*, 80(9):1505–1507, 2002.
- [13] Ji Xin Cheng and Xiaoliang Sunney Xie. *Coherent Raman scattering microscopy*. CRC press, 2012.
- [14] Jennifer P Ogilvie, Emmanuel Beaurepaire, Antigoni Alexandrou, and Manuel Joffre. Fourier transform coherent anti-stokes raman scattering microscopy. *Optics letters*, 31(4):480–482, 2006.
- [15] Eric O Potma, Conor L Evans, and X Sunney Xie. Heterodyne coherent anti-stokes raman scattering (cars) imaging. *Optics Letters*, 31(2):241–243, 2006.
- [16] Conor L Evans, Eric O Potma, Mehron Puoris' haag, Daniel Côté, Charles P Lin, and X Sunney Xie. Chemical imaging of tissue in vivo with video-rate coherent anti-stokes raman scattering microscopy. *Proceedings of the National Academy of Sciences of the United States of America*, 102(46):16807–16812, 2005.
- [17] Yasuyuki Ozeki, Wataru Umemura, Yoichi Otsuka, Shuya Satoh, Hiroyuki Hashimoto, Kazuhiko Sumimura, Norihiko Nishizawa, Kiichi Fukui, and Kazuyoshi Itoh. High-speed molecular spectral imaging of tissue with stimulated raman scattering. *Nature photonics*, 6(12):845–851, 2012.
- [18] Michiel Müller and Juleon M Schins. Imaging the thermodynamic state of lipid membranes with multiplex cars microscopy. *The Journal of Physical Chemistry B*, 106(14):3715–3723, 2002.
- [19] Andrius Baltuska, Zhiyi Wei, Maxim S. Pshenichnikov, and Douwe A. Wiersma. Optical pulse compression to 5 fs at a 1-mhz repetition rate. *Opt. Lett.*, 22(2):102–104, Jan 1997.
- [20] Li-Jin Chen, Andrew J Benedick, Jonathan R Birge, Michelle Y Sander, and Franz Kärtner. Octave-spanning, dual-output 2.166 ghz ti: sapphire laser. *Optics express*, 16(25):20699–20705, 2008.
- [21] Tara M Fortier, Albrecht Bartels, and Scott A Diddams. Octave-spanning ti: sapphire laser with a repetition rate > 1 ghz for optical frequency measurements and comparisons. *Optics Letters*, 31(7):1011–1013, 2006.
- [22] Albrecht Bartels, Thomas Dekorsy, and Heinrich Kurz. Femtosecond ti: sapphire ring laser with a 2-ghz repetition rate and its application in time-resolved spectroscopy. *Optics letters*, 24(14):996–998, 1999.

- [23] Albrecht Bartels, Dirk Heinecke, and Scott A Diddams. Passively mode-locked 10 ghz femtosecond ti: sapphire laser. *Optics letters*, 33(16):1905–1907, 2008.
- [24] Giovana T Nogueira and Flavio C Cruz. Efficient 1 ghz ti: sapphire laser with improved broadband continuum in the infrared. *Optics letters*, 31(13):2069–2071, 2006.
- [25] P.W. Smith. Mode-locking of lasers. *Proceedings of the IEEE*, 58(9):1342–1357, Sept 1970.
- [26] E. Goulielmakis, M. Schultze, M. Hofstetter, V. S. Yakovlev, J. Gagnon, M. Uiberacker, A. L. Aquila, E. M. Gullikson, D. T. Attwood, R. Kienberger, F. Krausz, and U. Kleineberg. Single-cycle nonlinear optics. *Science*, 320(5883):1614–1617, 2008.
- [27] U. Morgner, F. X. Kärtner, S. H. Cho, Y. Chen, H. A. Haus, J. G. Fujimoto, E. P. Ippen, V. Scheuer, G. Angelow, and T. Tschudi. Sub-two-cycle pulses from a kerr-lens mode-locked ti:sapphire laser. *Opt. Lett.*, 24(6):411–413, Mar 1999.
- [28] M. Nisoli, S. De Silvestri, O. Svelto, R. Szipöcs, K. Ferencz, Ch. Spielmann, S. Sartania, and F. Krausz. Compression of high-energy laser pulses below 5 fs. *Opt. Lett.*, 22(8):522–524, Apr 1997.
- [29] J.C. Diels, W. Rudolph, P.F. Liao, and P. Kelley. *Ultrashort Laser Pulse Phenomena*. Optics and photonics. Elsevier Science, 2006.
- [30] Thomas Brabec and Ferenc Krausz. Intense few-cycle laser fields: Frontiers of nonlinear optics. *Reviews of Modern Physics*, 72(2):545, 2000.
- [31] Lia Matos, Oliver D. Mücke, Jian Chen, and Franz X. Kärtner. Carrier-envelope phase dynamics and noise analysis in octave-spanning ti:sapphire lasers. *Opt. Express*, 14(6):2497–2511, Mar 2006.
- [32] Steven T. Cundiff and Jun Ye. *Colloquium* : Femtosecond optical frequency combs. *Rev. Mod. Phys.*, 75:325–342, Mar 2003.
- [33] J. Reichert, R. Holzwarth, Th. Udem, and T.W. Hänsch. Measuring the frequency of light with mode-locked lasers. *Optics Communications*, 172(1–6):59–68, 1999.
- [34] N. J. Harrick. Surface chemistry from spectral analysis of totally internally reflected radiation\*. *The Journal of Physical Chemistry*, 64(9):1110–1114, 1960.
- [35] J Fahrenfort. Attenuated total reflection: A new principle for the production of useful infra-red reflection spectra of organic compounds. *Spectrochimica Acta*, 17(7):698–709, 1961.
- [36] R. Trebino. *Frequency-Resolved Optical Gating: The Measurement of Ultrashort Laser Pulses*. Springer US, 2012.
- [37] F. Träger. *Springer Handbook of Lasers and Optics*. Springer, 2012.

- [38] G Guelachvili. Near infrared wide-band spectroscopy with 27-mhz resolution. *Applied optics*, 16(8):2097–2101, 1977.
- [39] C.E. Shannon. Communication in the presence of noise. *Proceedings of the IRE*, 37(1):10–21, Jan 1949.
- [40] P. Seibt. *Algorithmic Information Theory: Mathematics of Digital Information Processing*. Signals and Communication Technology. Springer Berlin Heidelberg, 2007.
- [41] B.P. Lathi. *Linear Systems and Signals*. Oxford series in electrical and computer engineering. Oxford University Press, 2005.
- [42] H.A. Haus and A. Mecozzi. Noise of mode-locked lasers. *Quantum Electronics, IEEE Journal of*, 29(3):983–996, Mar 1993.
- [43] P.-T. Ho. Phase and amplitude fluctuations in a mode-locked laser. *Quantum Electronics, IEEE Journal of*, 21(11):1806–1813, Nov 1985.
- [44] R. Paschotta, A. Schlatter, S.C. Zeller, H.R. Telle, and U. Keller. Optical phase noise and carrier-envelope offset noise of mode-locked lasers. *Applied Physics B*, 82(2):265–273, 2006.
- [45] N.R. Newbury and B.R. Washburn. Theory of the frequency comb output from a femtosecond fiber laser. *Quantum Electronics, IEEE Journal of*, 41(11):1388–1402, Nov 2005.
- [46] B. R. Washburn, W. C. Swann, and N. R Newbury. Response dynamics of the frequency comb output from a femtosecond fiber laser. *Opt. Express*, 13(26):10622–10633, Dec 2005.
- [47] N. Haverkamp, H. Hundertmark, C. Fallnich, and H.R. Telle. Frequency stabilization of mode-locked erbium fiber lasers using pump power control. *Applied Physics B*, 78(3–4):321–324, 2004.
- [48] H.R. Telle, B. Lipphardt, and J. Stenger. Kerr-lens, mode-locked lasers as transfer oscillators for optical frequency measurements. *Applied Physics B*, 74(1):1–6, 2002.
- [49] D.R. Walker, Th. Udem, Ch. Gohle, B. Stein, and T.W. Hänsch. Frequency dependence of the fixed point in a fluctuating frequency comb. *Applied Physics B*, 89(4):535–538, 2007.
- [50] Antonin Poisson. *Spectroscopie adaptative À deux peignes de fréquences*. PhD thesis, 2013. Thèse de doctorat dirigée par Picquès, Nathalie Physique Paris 11 2013.
- [51] Sebastian Koke, Christian Grebing, Harald Frei, Alexandria Anderson, Andreas Assion, and Günter Steinmeyer. Direct frequency comb synthesis with arbitrary offset and shot-noise-limited phase noise. *Nature Photonics*, 4(7):462–465, 2010.

- [52] Fabian Lücking, Andreas Assion, Alexander Apolonski, Ferenc Krausz, and Günter Steinmeyer. Long-term carrier-envelope-phase-stable few-cycle pulses by use of the feed-forward method. *Opt. Lett.*, 37(11):2076–2078, Jun 2012.
- [53] Takuro Ideguchi, Antonin Poisson, Guy Guelachvili, Nathalie Picqué, and Theodor W Hänsch. Adaptive real-time dual-comb spectroscopy. *Nature communications*, 5, 2014.
- [54] A.M. Zolot, F.R. Giorgetta, E. Baumann, W.C. Swann, I. Coddington, and N.R. Newbury. Broad-band frequency references in the near-infrared: Accurate dual comb spectroscopy of methane and acetylene. *Journal of Quantitative Spectroscopy and Radiative Transfer*, 118(0):26 – 39, 2013.
- [55] Jean-Daniel Deschênes, Philippe Giaccari, and Jérôme Genest. Optical referencing technique with cw lasers as intermediate oscillators for continuous full delay range frequency comb interferometry. *Opt. Express*, 18(22):23358–23370, Oct 2010.
- [56] Philippe Giaccari, Jean-Daniel Deschênes, Philippe Saucier, Jerome Genest, and Pierre Tremblay. Active fourier-transform spectroscopy combining the direct rf beating of two fiber-based mode-locked lasers with a novel referencing method. *Opt. Express*, 16(6):4347–4365, Mar 2008.
- [57] Julien Roy, Jean-Daniel Deschênes, Simon Potvin, and Jérôme Genest. Continuous real-time correction and averaging for frequency comb interferometry. *Opt. Express*, 20(20):21932–21939, Sep 2012.
- [58] H.G.O. Becker and R. Beckert. *Organikum: organisch-chemisches Grundpraktikum*. Wiley-VCH-Verlag, 2009.
- [59] M Natali Cizmeciyan, Huseyin Cankaya, Adnan Kurt, and Alphan Sennaroglu. Kerr-lens mode-locked femtosecond cr 2+: Znse laser at 2420 nm. *Optics letters*, 34(20):3056–3058, 2009.
- [60] Nikolai Tolstik, Evgeni Sorokin, and Irina T Sorokina. Kerr-lens mode-locked cr: Zns laser. *Optics letters*, 38(3):299–301, 2013.
- [61] Evgeni Sorokin, Nikolai Tolstik, Kathleen I Schaffers, and Irina T Sorokina. Femtosecond sesam-modelocked cr: Zns laser. *Optics express*, 20(27):28947–28952, 2012.
- [62] MN Cizmeciyan, JW Kim, S Bae, BH Hong, F Rotermund, and A Sennaroglu. Graphene mode-locked femtosecond cr: Znse laser at 2500 nm. *Optics letters*, 38(3):341–343, 2013.
- [63] LE Nelson, EP Ippen, and HA Haus. Broadly tunable sub-500 fs pulses from an additive-pulse mode-locked thulium-doped fiber ring laser. *Applied physics letters*, 67(1):19–21, 1995.

- [64] Max A Solodyankin, Elena D Obraztsova, Anatoly S Lobach, Alexander I Chernov, Anton V Tausenev, Vitaly I Konov, and Evgueni M Dianov. Mode-locked 1.93  $\mu\text{m}$  thulium fiber laser with a carbon nanotube absorber. *Optics letters*, 33(12):1336–1338, 2008.
- [65] K Kieu and FW Wise. Soliton thulium-doped fiber laser with carbon nanotube saturable absorber. *IEEE photonics technology letters: a publication of the IEEE Laser and Electro-optics Society*, 21(3):128, 2009.
- [66] Frithjof Haxsen, Dieter Wandt, Uwe Morgner, Joerg Neumann, and Dietmar Kracht. Pulse characteristics of a passively mode-locked thulium fiber laser with positive and negative cavity dispersion. *Optics express*, 18(18):18981–18988, 2010.
- [67] Qing Wang, Jihong Geng, Zhuo Jiang, Tao Luo, and Shibin Jiang. Mode-locked tm-ho-codoped fiber laser at 2.06  $\mu\text{m}$ . *Photonics Technology Letters, IEEE*, 23(11):682–684, 2011.
- [68] Roberto Paiella, Federico Capasso, Claire Gmachl, Deborah L Sivco, James N Baillargeon, Albert L Hutchinson, Alfred Y Cho, and HC Liu. Self-mode-locking of quantum cascade lasers with giant ultrafast optical nonlinearities. *Science*, 290(5497):1739–1742, 2000.
- [69] Christine Y Wang, Lyuba Kyznetsova, VM Gkortsas, Laurent Diehl, FX Kartner, Mikhail A Belkin, Alexey Belyanin, Xiaofeng Li, Donhee Ham, Harald Schneider, et al. Mode-locked pulses from mid-infrared quantum cascade lasers. *Optics express*, 17(15):19929–12943, 2009.
- [70] Andreas Hugi, Gustavo Villares, Stéphane Blaser, HC Liu, and Jérôme Faist. Mid-infrared frequency comb based on a quantum cascade laser. *Nature*, 492(7428):229–233, 2012.
- [71] Alessio Gambetta, Roberta Ramponi, and Marco Marangoni. Mid-infrared optical combs from a compact amplified er-doped fiber oscillator. *Optics letters*, 33(22):2671–2673, 2008.
- [72] Fritz Keilmann and Sergiu Amarie. Mid-infrared frequency comb spanning an octave based on an er fiber laser and difference-frequency generation. *Journal of Infrared, Millimeter, and Terahertz Waves*, 33(5):479–484, 2012.
- [73] Axel Ruehl, Alessio Gambetta, Ingmar Hartl, Martin E Fermann, Kjeld SE Eikema, and Marco Marangoni. Widely-tunable mid-infrared frequency comb source based on difference frequency generation. *Optics letters*, 37(12):2232–2234, 2012.
- [74] A Esteban-Martin, O Kokabee, and M Ebrahim-Zadeh. Efficient, high-repetition-rate, femtosecond optical parametric oscillator tunable in the red. *Optics letters*, 33(22):2650–2652, 2008.

- [75] Suddapalli Chaitanya Kumar, Adolfo Esteban-Martin, Takuro Ideguchi, Ming Yan, Simon Holzner, Theodor W. Hänsch, Nathalie Picque, and Majid Ebrahim-Zadeh. Few-cycle, broadband, mid-infrared optical parametric oscillator pumped by a 20 fs ti:sapphire laser. *Laser and Photonics Reviews*, 8(5):L86–L91, 2014.
- [76] P Loza-Alvarez, CTA Brown, DT Reid, W Sibbett, and M Missey. High-repetition-rate ultrashort-pulse optical parametric oscillator continuously tunable from 2.8 to 6.8  $\mu\text{m}$ . *Optics letters*, 24(21):1523–1525, 1999.
- [77] JH Sun, BJS Gale, and DT Reid. Composite frequency comb spanning 0.4-2.4  $\mu\text{m}$  from a phase-controlled femtosecond ti: sapphire laser and synchronously pumped optical parametric oscillator. *Optics letters*, 32(11):1414–1416, 2007.
- [78] Suddapalli Chaitanya Kumar, Adolfo Esteban-Martin, Takuro Ideguchi, Ming Yan, Simon Holzner, Theodor W Hänsch, Nathalie Picqué, and Majid Ebrahim-Zadeh. Few-cycle, broadband, mid-infrared optical parametric oscillator pumped by a 20-fs ti: sapphire laser. *Laser & photonics reviews*, 8(5):L86–L91, 2014.
- [79] D. A. Bryan, Robert Gerson, and H. E. Tomaschke. Increased optical damage resistance in lithium niobate. *Applied Physics Letters*, 44(9):847–849, 1984.
- [80] Y. Furukawa, K. Kitamura, S. Takekawa, A. Miyamoto, M. Terao, and N. Suda. Photorefraction in linbo3 as a function of [li]/[nb] and mgo concentrations. *Applied Physics Letters*, 77(16):2494–2496, 2000.
- [81] Koichiro Nakamura, Jonathan Kurz, Krishnan Parameswaran, and M. M. Fejer. Periodic poling of magnesium-oxide-doped lithium niobate. *Journal of Applied Physics*, 91(7):4528–4534, 2002.
- [82] Ashok Kaul and Ajay Mishra. Fabrication of periodically poled lithium niobate chips for optical parametric oscillators. *Pramana*, 75(5):817–826, 2010.
- [83] M. Fujimura, T. Kodama, T. Suhara, and H. Nishihara. Quasi-phase-matched self-frequency-doubling waveguide laser in nd:linbo/sub 3/. *Photonics Technology Letters, IEEE*, 12(11):1513–1515, Nov 2000.
- [84] V Pruneri, R Koch, PG Kazansky, WA Clarkson, P St J Russell, and DC Hanna. 49 mw of cw blue light generated by first-order quasi-phase-matched frequency doubling of a diode-pumped 946-nm nd: Yag laser. *Optics letters*, 20(23):2375–2377, 1995.
- [85] Vered Mahal, Mark A Arbore, Martin M Fejer, and Ady Arie. Quasi-phase-matched frequency doubling in a waveguide of a 1560-nm diode laser and locking to the rubidium d 2 absorption lines. *Optics letters*, 21(16):1217–1219, 1996.
- [86] Samuel T Wong, Tomas Plettner, Konstantin L Vodopyanov, Karel Urbanek, Michel Digonnet, and Robert L Byer. Self-phase-locked degenerate femtosecond optical parametric oscillator. *Optics letters*, 33(16):1896–1898, 2008.

- [87] Alireza Marandi, Nick C Leindecker, Vladimir Pervak, Robert L Byer, and Konstantin L Vodopyanov. Coherence properties of a broadband femtosecond mid-ir optical parametric oscillator operating at degeneracy. *Optics express*, 20(7):7255–7262, 2012.
- [88] Venkata Ramaiah-Badarla, Adolfo Esteban-Martin, and Majid Ebrahim-Zadeh. Self-phase-locked degenerate femtosecond optical parametric oscillator based on bib3o6. *Laser & Photonics Reviews*, 7(5):L55–L60, 2013.
- [89] S.M.J. Kelly. Characteristic sideband instability of periodically amplified average soliton. *Electronics Letters*, 28:806–807(1), April 1992.
- [90] H.A. Haus. Mode-locking of lasers. *Selected Topics in Quantum Electronics, IEEE Journal of*, 6(6):1173–1185, Nov 2000.
- [91] D.T. Reid, C. McGowan, M. Ebrahimzadeh, and W. Sibbett. Characterization and modeling of a noncollinearly phase-matched femtosecond optical parametric oscillator based on kta and operating to beyond 4  $\mu\text{m}$ . *Quantum Electronics, IEEE Journal of*, 33(1):1–9, Jan 1997.
- [92] Nick Leindecker, Alireza Marandi, Robert L. Byer, and Konstantin L. Vodopyanov. Broadband degenerate opo for mid-infrared frequency comb generation. *Opt. Express*, 19(7):6296–6302, Mar 2011.
- [93] J.M. Dudley, D.T. Reid, W. Sibbett, L.P. Barry, B. Thomsen, and J.D. Harvey. Commercial semiconductor devices for two photon absorption autocorrelation of ultrashort light pulses. *Appl. Opt.*, 37(34):8142–8144, Dec 1998.
- [94] RR Alfano and SL Shapiro. Emission in the region 4000 to 7000  $\text{\AA}$  via four-photon coupling in glass. *Physical Review Letters*, 24(11):584, 1970.
- [95] RR Alfano and SL Shapiro. Observation of self-phase modulation and small-scale filaments in crystals and glasses. *Physical Review Letters*, 24(11):592, 1970.
- [96] Jinendra K Ranka, Robert S Windeler, and Andrew J Stentz. Visible continuum generation in air-silica microstructure optical fibers with anomalous dispersion at 800 nm. *Optics letters*, 25(1):25–27, 2000.
- [97] Jonathan C Knight. Photonic crystal fibres. *Nature*, 424(6950):847–851, 2003.
- [98] Philip St J Russell. Photonic-crystal fibers. *Journal of lightwave technology*, 24(12):4729–4749, 2006.
- [99] Alan D Bristow, Nir Rotenberg, and Henry M Van Driel. Two-photon absorption and kerr coefficients of silicon for 850-2200 nm. *Appl. phys. lett*, 90(19):191104, 2007.
- [100] Benjamin J Eggleton, Barry Luther-Davies, and Kathleen Richardson. Chalcogenide photonics. *Nature photonics*, 5(3):141–148, 2011.

- [101] Bart Kuyken, Takuro Ideguchi, Simon Holzner, Ming Yan, Theodor W Hänsch, Joris Van Campenhout, Peter Verheyen, Stéphane Coen, Francois Leo, Roel Baets, et al. An octave-spanning mid-infrared frequency comb generated in a silicon nanophotonic wire waveguide. *Nature communications*, 6, 2015.
- [102] John M Dudley, Goëry Genty, and Stéphane Coen. Supercontinuum generation in photonic crystal fiber. *Reviews of modern physics*, 78(4):1135, 2006.
- [103] John M Dudley, Goëry Genty, and Stéphane Coen. Supercontinuum generation in photonic crystal fiber. *Reviews of modern physics*, 78(4):1135, 2006.
- [104] J. Ye and S.T. Cundiff. *Femtosecond Optical Frequency Comb: Principle, Operation and Applications*. SpringerLink: Springer e-Books. Springer, 2005.
- [105] J.A. Savage and S. Nielsen. Chalcogenide glasses transmitting in the infrared between 1 and 20  $\mu\text{m}$ : a state of the art review. *Infrared Physics*, 5(4):195 – 204, 1965.
- [106] J.A. Savage. Optical properties of chalcogenide glasses. *Journal of Non-Crystalline Solids*, 47(1):101 – 115, 1982. Proceedings of the Conference on Optical Properties of Glass and Optical Materials.
- [107] A.R. Hilton, D.J. Hayes, and M.D. Rechtin. Infrared absorption of some high purity chalcogenide glasses. *Journal of Non-Crystalline Solids*, 17(3):319 – 338, 1975.
- [108] P.J. Webber and J.A. Savage. Some physical properties of geasse infrared optical glasses. *Journal of Non-Crystalline Solids*, 20(2):271 – 283, 1976.
- [109] Keiji Tanaka. Structural phase transitions in chalcogenide glasses. *Phys. Rev. B*, 39:1270–1279, Jan 1989.
- [110] Amrita Prasad, Cong-Ji Zha, Rong-Ping Wang, Anita Smith, Steve Madden, and Barry Luther-Davies. Properties of gexasyse1-x-y glasses for all-optical signal processing. *Opt. Express*, 16(4):2804–2815, Feb 2008.
- [111] Alireza Marandi, Charles W. Rudy, Victor G. Plotnichenko, Evgeny M. Dianov, Konstantin L. Vodopyanov, and Robert L. Byer. Mid-infrared supercontinuum generation in tapered chalcogenide fiber for producing octave-spanning frequency comb around 3  $\mu\text{m}$ . *Opt. Express*, 20(22):24218–24225, Oct 2012.
- [112] Darren Hudson, Matthias Baudisch, Benjamin Eggleton, Jens Biegert, and Daniel Werdehausen. 1.9 octave supercontinuum generation in a as<sub>2</sub>s<sub>3</sub> step-index fiber driven by mid-ir opcpa. *Opt. Lett.*, 39(19):5752–5755, 2014.
- [113] Xin Gai, Duk-Yong Choi, Steve Madden, Zhiyong Yang, Rongping Wang, and Barry Luther-Davies. Supercontinuum generation in the mid-infrared from a dispersion-engineered as<sub>2</sub>s<sub>3</sub> glass rib waveguide. *Opt. Lett.*, 37(18):3870–3872, Sep 2012.

- [114] Masaki Asobe, Terutoshi Kanamori, Kazunori Naganuma, Hiroki Itoh, and Toshikuni Kaino. Third-order nonlinear spectroscopy in  $As_2S_3$  chalcogenide glass fibers. *Journal of applied physics*, 77(11):5518–5523, 1995.
- [115] Trung D Vo, Jochen Schröder, Bill Corcoran, Jürgen Van Erps, Stephen J Madden, Duk-Yong Choi, Douglas AP Bulla, Barry Luther-Davies, Mark D Pelusi, and Benjamin J Eggleton. Photonic-chip-based ultrafast waveform analysis and optical performance monitoring. *IEEE Journal of Selected Topics in Quantum Electronics*, 18(2):834, 2012.
- [116] SJ Madden, Duk-Yong Choi, DA Bulla, Andrei V Rode, Barry Luther-Davies, Vahid G Ta’eed, MD Pelusi, and Benjamin J Eggleton. Long, low loss etched  $As_2S_3$  chalcogenide waveguides for all-optical signal regeneration. *Optics express*, 15(22):14414–14421, 2007.
- [117] W. J. Tomlinson, R. H. Stolen, and A. M. Johnson. Optical wave breaking of pulses in nonlinear optical fibers. *Opt. Lett.*, 10(9):457–459, Sep 1985.
- [118] Joshua E. Rothenberg and D. Grischkowsky. Observation of the formation of an optical intensity shock and wave breaking in the nonlinear propagation of pulses in optical fibers. *Phys. Rev. Lett.*, 62:531–534, Jan 1989.
- [119] Joshua E. Rothenberg. Femtosecond optical shocks and wave breaking in fiber propagation. *J. Opt. Soc. Am. B*, 6(12):2392–2401, Dec 1989.
- [120] R Graham and H Haken. The quantum-fluctuations of the optical parametric oscillator. i. *Zeitschrift für Physik*, 210(3):276–302, 1968.
- [121] R Graham. The quantum-fluctuations of the optical parametric oscillator. ii. *Zeitschrift für Physik*, 210(4):319–336, 1968.
- [122] N. C. Wong. Optical frequency division using an optical parametric oscillator. *Opt. Lett.*, 15(20):1129–1131, Oct 1990.
- [123] Harald R Telle, Burghard Lipphardt, and Jörn Stenger. Kerr-lens, mode-locked lasers as transfer oscillators for optical frequency measurements. *Applied Physics B*, 74(1):1–6, 2002.
- [124] N Haverkamp, H Hundertmark, C Fallnich, and HR Telle. Frequency stabilization of mode-locked erbium fiber lasers using pump power control. *Applied Physics B*, 78(3-4):321–324, 2004.
- [125] David R Walker, Th Udem, Ch Gohle, Björn Stein, and Theodor W Hänsch. Frequency dependence of the fixed point in a fluctuating frequency comb. *Applied Physics B*, 89(4):535–538, 2007.
- [126] Vilson R Almeida, Roberto R Panepucci, and Michal Lipson. Nanotaper for compact mode conversion. *Optics letters*, 28(15):1302–1304, 2003.

- [127] Michal Lipson. Overcoming the limitations of microelectronics using si nanophotonics: solving the coupling, modulation and switching challenges. *Nanotechnology*, 15(10):S622, 2004.
- [128] Leonhard Möckl, Don C Lamb, and Christoph Bräuchle. Superhochauflösende mikroskopie: Nobelpreis in chemie 2014 für eric betzig, stefan hell und william e. moerner. *Angewandte Chemie*, 126(51):14192–14197, 2014.
- [129] Eric Betzig, George H. Patterson, Rachid Sougrat, O. Wolf Lindwasser, Scott Olenych, Juan S. Bonifacino, Michael W. Davidson, Jennifer Lippincott-Schwartz, and Harald F. Hess. Imaging intracellular fluorescent proteins at nanometer resolution. 313(5793):1642–1645, 2006.
- [130] Shuming Nie and Steven R. Emory. Probing single molecules and single nanoparticles by surface-enhanced raman scattering. 275(5303):1102–1106, 1997.
- [131] H. Peter Lu, Luying Xun, and X. Sunney Xie. Single-molecule enzymatic dynamics. 282(5395):1877–1882, 1998.
- [132] Harry S Orbach, LAWRENCE B Cohen, and Amiram Grinvald. Optical mapping of electrical activity in rat somatosensory and visual cortex. *The Journal of neuroscience*, 5(7):1886–1895, 1985.
- [133] Walther Akemann, Hiroki Mutoh, Amélie Perron, Yun Kyung Park, Yuka Iwamoto, and Thomas Knöpfel. Imaging neural circuit dynamics with a voltage-sensitive fluorescent protein. *Journal of neurophysiology*, 108(8):2323–2337, 2012.
- [134] Bu-Qing Mao, Farid Hamzei-Sichani, Dmitriy Aronov, Robert C Froemke, and Rafael Yuste. Dynamics of spontaneous activity in neocortical slices. *Neuron*, 32(5):883–898, 2001.
- [135] Roger Y Tsien. Fluorescence measurement and photochemical manipulation of cytosolic free calcium. *Trends in neurosciences*, 11(10):419–424, 1988.
- [136] Christoph Stosiek, Olga Garaschuk, Knut Holthoff, and Arthur Konnerth. In vivo two-photon calcium imaging of neuronal networks. *Proceedings of the National Academy of Sciences*, 100(12):7319–7324, 2003.
- [137] H. Grunewald. Nobel lectures. physiology and medicine 1922 to 1941 elsevier publish comp. *Angewandte Chemie*, 78(8):456–456, 1966.
- [138] Robert W. Boyd. *Nonlinear Optics, Third Edition*. Academic Press, 2008.
- [139] Nirit Dudovich, Dan Oron, and Yaron Silberberg. Single-pulse coherently controlled nonlinear raman spectroscopy and microscopy. *Nature*, 418(6897):512–514, 2002.
- [140] Eunah Kang, Haifeng Wang, Il Keun Kwon, Joshua Robinson, Kinam Park, and Ji-Xin Cheng. In situ visualization of paclitaxel distribution and release by coherent

- anti-stokes raman scattering microscopy. *Analytical chemistry*, 78(23):8036–8043, 2006.
- [141] Michiel Müller and Juleon M Schins. Imaging the thermodynamic state of lipid membranes with multiplex cars microscopy. *The Journal of Physical Chemistry B*, 106(14):3715–3723, 2002.
- [142] Jennifer P. Ogilvie, Emmanuel Beaurepaire, Antigoni Alexandrou, and Manuel Joffre. Fourier-transform coherent anti-stokes raman scattering microscopy. *Opt. Lett.*, 31(4):480–482, Feb 2006.
- [143] A. Weiner. *Ultrafast Optics*. Wiley Series in Pure and Applied Optics. Wiley, 2011.
- [144] Haim Lotem, R. T. Lynch, and N. Bloembergen. Interference between raman resonances in four-wave difference mixing. *Phys. Rev. A*, 14:1748–1755, Nov 1976.
- [145] JeanLouis Oudar, Robert W. Smith, and Y. R. Shen. Polarization sensitive coherent anti stokes raman spectroscopy. *Applied Physics Letters*, 34(11):758–760, 1979.
- [146] W. M. Tolles and R. D. Turner. A comparative analysis of the analytical capabilities of coherent anti-stokes raman spectroscopy (cars) relative to raman scattering and absorption spectroscopy. *Appl. Spectrosc.*, 31(2):96–103, Mar 1977.
- [147] Dan Oron, Nirit Dudovich, and Yaron Silberberg. Femtosecond phase-and-polarization control for background-free coherent anti-stokes raman spectroscopy. *Phys. Rev. Lett.*, 90:213902, May 2003.
- [148] Sang-Hyun Lim, Allison G. Caster, and Stephen R. Leone. Single-pulse phase-control interferometric coherent anti-stokes raman scattering spectroscopy. *Phys. Rev. A*, 72:041803, Oct 2005.
- [149] Erik M. Vartiainen, Hilde A. Rinia, Michiel Müller, and Mischa Bonn. Direct extraction of raman line-shapes from congested cars spectra. *Opt. Express*, 14(8):3622–3630, Apr 2006.
- [150] Jennifer P Ogilvie, Meng Cui, Dmitry Pestov, Alexei V Sokolov, and Marlan O Scully. Time-delayed coherent raman spectroscopy. *Molecular Physics*, 106(2–4):587–594, 2008.
- [151] Nirit Dudovich, Dan Oron, and Yaron Silberberg. Single-pulse coherent anti-stokes raman spectroscopy in the fingerprint spectral region. *The Journal of Chemical Physics*, 118(20):9208–9215, 2003.
- [152] Sang-Hyun Lim, Allison G. Caster, Olivier Nicolet, and Stephen R. Leone. Chemical imaging by single pulse interferometric coherent anti-stokes raman scattering microscopy. *The Journal of Physical Chemistry B*, 110(11):5196–5204, 2006. PMID: 16539448.

- [153] M.D. Levenson and S. Kano. *Introduction to nonlinear laser spectroscopy*. Quantum electronics—principles and applications. Academic Press, 1988.
- [154] B. Schrader. *Raman/Infrared Atlas of Organic Compounds*. Wiley, 1996.
- [155] MA Yuratich and DC Hanna. Coherent anti-stokes raman spectroscopy (cars) selection rules, depolarization ratios and rotational structure. *Molecular Physics*, 33(3):671–682, 1977.
- [156] Gary C Bjorklund. Effects of focusing on third-order nonlinear processes in isotropic media. *Quantum Electronics, IEEE Journal of*, 11(6):287–296, 1975.
- [157] Ji-Xin Cheng and X Sunney Xie. Coherent anti-stokes raman scattering microscopy: instrumentation, theory, and applications. *The Journal of Physical Chemistry B*, 108(3):827–840, 2004.
- [158] Eric O Potma, Wim P de Boeij, and Douwe A Wiersma. Nonlinear coherent four-wave mixing in optical microscopy. *JOSA B*, 17(10):1678–1684, 2000.
- [159] Takuro Ideguchi, Simon Holzner, Birgitta Bernhardt, Guy Guelachvili, Nathalie Picqué, and Theodor W Hänsch. Coherent raman spectro-imaging with laser frequency combs. *Nature*, 502(7471):355–358, 2013.
- [160] M.J. Weber. *Handbook of Optical Materials*. Laser & Optical Science & Technology. Taylor & Francis, 2002.
- [161] M.J. Weber. *CRC Handbook of Laser Science and Technology Supplement 2: Optical Materials*. Laser & Optical Science & Technology. Taylor & Francis, 1994.
- [162] Yan Fu, Haifeng Wang, Riyi Shi, and Ji-Xin Cheng. Characterization of photodamage in coherent anti-stokes raman scattering microscopy. *Optics Express*, 14(9):3942–3951, 2006.
- [163] Alexander Hopt and Erwin Neher. Highly nonlinear photodamage in two-photon fluorescence microscopy. *Biophysical journal*, 80(4):2029–2036, 2001.
- [164] Karsten König. Cell damage during multi-photon microscopy. In *Handbook of Biological Confocal Microscopy*, pages 680–689. Springer, 2006.
- [165] Kazutoshi Tanabe and Jiro Hiraishi. Raman linewidths and molecular diameters of liquids. *Molecular Physics*, 39(6):1507–1512, 1980.
- [166] MN Neuman and GC Tabisz. On a raman linewidth study of molecular motion in liquid benzene. *Chemical Physics*, 15(2):195–200, 1976.
- [167] Fredric J Harris. On the use of windows for harmonic analysis with the discrete fourier transform. *Proceedings of the IEEE*, 66(1):51–83, 1978.

- [168] Bernhard von Vacano and Marcus Motzkus. Time-resolving molecular vibration for microanalytics: single laser beam nonlinear raman spectroscopy in simulation and experiment. *Physical Chemistry Chemical Physics*, 10(5):681–691, 2008.
- [169] Dawn Schafer, Jeff A Squier, Jan van Maarseveen, Daniel Bonn, Mischa Bonn, and Michiel Mueller. In situ quantitative measurement of concentration profiles in a microreactor with submicron resolution using multiplex cars microscopy. *Journal of the American Chemical Society*, 130(35):11592–11593, 2008.
- [170] Kelly P Knutsen, Benjamin M Messer, Robert M Onorato, and Richard J Saykally. Chirped coherent anti-stokes raman scattering for high spectral resolution spectroscopy and chemically selective imaging. *The Journal of Physical Chemistry B*, 110(12):5854–5864, 2006.
- [171] Charles C Wang. Empirical relation between the linear and the third-order nonlinear optical susceptibilities. *Physical Review B*, 2(6):2045, 1970.
- [172] Philip CD Hobbs. Ultrasensitive laser measurements without tears. *Applied optics*, 36(4):903–920, 1997.
- [173] Albert Schliesser, Markus Brehm, Fritz Keilmann, and Daniel van der Weide. Frequency-comb infrared spectrometer for rapid, remote chemical sensing. *Optics Express*, 13(22):9029–9038, 2005.
- [174] A Ishizawa, T Nishikawa, Akira Mizutori, Hidehiko Takara, S Aozasa, Alessandro Mori, Hisamatsu Nakano, Akifumi Takada, and Masafumi Koga. Octave-spanning frequency comb generated by 250 fs pulse train emitted from 25 ghz externally phase-modulated laser diode for carrier-envelope-offset-locking. *Electronics letters*, 46(19):1343–1344, 2010.
- [175] Michiel Müller and Juleon M Schins. Imaging the thermodynamic state of lipid membranes with multiplex cars microscopy. *The Journal of Physical Chemistry B*, 106(14):3715–3723, 2002.
- [176] Günther Krauss, Sebastian Lohss, Tobias Hanke, Alexander Sell, Stefan Eggert, Rupert Huber, and Alfred Leitenstorfer. Synthesis of a single cycle of light with compact erbium-doped fibre technology. *Nature Photonics*, 4(1):33–36, 2010.
- [177] Alexander M Heidt, Jan Rothhardt, Alexander Hartung, Hartmut Bartelt, Erich G Rohwer, Jens Limpert, and Andreas Tünnermann. High quality sub-two cycle pulses from compression of supercontinuum generated in all-normal dispersion photonic crystal fiber. *Optics express*, 19(15):13873–13879, 2011.
- [178] Arthur Hipke, Samuel A Meek, Takuro Ideguchi, Theodor W Hänsch, and Nathalie Picqué. Broadband doppler-limited two-photon and stepwise excitation spectroscopy with laser frequency combs. *Physical Review A*, 90(1):011805, 2014.

- [179] Steven T. Cundiff, Jun Ye, and John L. Hall. Optical frequency synthesis based on mode-locked lasers. *Review of Scientific Instruments*, 72(10):3749–3771, 2001.



# Acknowledgments

First of all, I sincerely thank Prof. Theodor W. Hänsch and Nathalie Picqué for giving me the opportunity to work in the group at the Max Planck Institute of Quantum Optics and thus giving me the chance to participate in exciting projects and discussions. I want to thank them for the guidance, help and motivational discussions we shared.

My amazing colleagues Birgitta Bernhardt, Eugene Frumker, Antonin Poisson, Arthur Hipke, Samuel Meek, Ming Yan, Clément Lafargue, Kathrin Mohler, Zaijun Chen, Kana Iwakuni, Pei-Ling Luo, Bernhard Bohn and Takuro Ideguchi, I want to give my warmest thanks. I consider them not only colleagues but friends as well.

Birgitta Bernhardt (Gitti) was the only person I already knew from my time at the MPQ when I did my master's degree in a different group. She is one of the kindest persons I know and the time we worked together was really memorable.

With Eugene Frumker, I shared around a year of time at the MPQ, we had a lot of interesting discussions, to give an inspiring quote of him: "you can never have enough money"

Antonin Poisson is a very special person, indeed he does not fulfil any of the clichés German have concerning French people. He is a very silent character which I enjoy very much.

Arthur Hipke was, besides me, temporary the only other German in our group which led to the funny situation that most of the time we spoke in English to each other instead of German out of habit. I had a lot of (hard) scientific and unscientific discussions with him, which I value a lot.

Samuel Meek was, as well as Antonin, my office mate for about a year. I'm sure he is one of the persons I learned most of during my stay at the MPQ. I also enjoyed the time when he was staying in my flat for a while, during the time he was looking for a new apartment.

Ming Yan might very well be the kindest person in our group, working together with him is very enjoyable. If you get to know him more you will find out that he is what Germans call a "Schlitzohr" nevertheless. Later on Zaijun joined our group as fellow-countryman

of Ming, what has been said for Ming accounts for him as well, this is especially true concerning the “Schlitzohr”-thing.

Clément Lafargue as the second French guy in our group, contrary to Antonin he fulfilled a significant amount of clichés Germans have concerning French people. He one of the most open-hearted person I know.

With Kathrin Mohler the first female came to our group, who started the trend that in this very special group more females than males will be working after Arthur, who will finish presumably some month after me, and I leave. I had a very pleasant time working with Kathrin who is as friendly as ambitious (meant in a purely positive way).

Kana Iwakuni and Pei-Ling Luo, both are very kind and helpful. The time we spent together was very enjoyable.

With Bernhard Bohn, I have a special relationship, we share the office and, at least from my side, I would say we became good and close friends over the time. He is definitely one of the most memorable persons I met during my stay at the MPQ.

What has been said for Bernhard is also true for Takuro Ideguchi. We did not share an office but we worked together for more than two years. I rarely found a person who is so pleasant working with. He is modest and thoughtful. When he left MPQ I felt sad that he is not around anymore and I still do.

Then I have to mention our collaborators, or to be more precise, the people who came to the MPQ during the course of these collaborations: Chaitanya Kumar Suddapalli, Adolfo Esteban-Martin and Bart Kuyken. I spent a significant amount of time with these people in the laboratory and I can state I do not want to miss it. Not only came all of the experiments we started together with them to a successful ending, but working together with these people was a very nice experience.

Mentioning nice people, I also have to mention two more people explicitly: Anna Soter and Hossein Aghai-Khozani, my former office mates (yes I had to change my office several times). The time I spent together with these two in the same office was very nice and we had plenty of discussions. Apart from their excellent professional knowledge they have significant knowledge outside of the physical world, for example about all kind of nerd things as the disc world, star wars and so on. I will not tell who has (considerably more) knowledge of geek stuff but as a hint: she has long hair..

Finally, concerning the people of the Hänsch group not directly associated with our sub-division, I can state that among them I did not find a single person, who I found to be unpleasant. All of them are friendly, sympathetic and try to help wherever possible. To all of those who are not mentioned directly: I want to thank you for your help and support!

Explicitly I also have to mention Wolfgang Simon and Karl Linner, the mechanical engineers of the Hänsch group. Even the most complicated mechanical parts were

produced by those two with terrifying speed and precision, that is amazing. When you enter their room and ask for some strange component to be produced you hear something like: "Today, it is not possible, we have too many things to do, (please) come back in a couple of days". Half an hour later the component is milled, drilled or whatever and ready to use. Thank you very much for your support!

Same goes true for Helmut Brücker, the electrical engineer of the Hänsch group. He made (countless) photodiodes and lock-boxes as well as etched plenty of printed boards for me. I had a significant amount of discussions (scientific or not) with him, which were very helpful for me. Thank you for your constant support!

I also want to thank Gabriele Gschwendtner (explicitly) for her constant support. As the head of the Hänsch office she helped me whenever possible, organised all of the things I messed up and above all she was always very friendly to me.

Apart from the people of the Hänsch group, there are several people in the group of Prof. Ferenc Krausz I want to mention. I did my master's degree in his group and, somehow, never really left. I want to thank the "Italian connection": Hanieh Fattahi, Nick Karpowicz, Martin Schultze, Gitti and Olga Razskazovskaya for the nice time we spent. I am also obliged to thank Hanieh to be the "best colleague ever" for reasons which can not be stated at this point. Additionally, I want to thank Martin (again), Prof. Reinhard Kienberger and Wolfram Helml for help and support whenever I needed it. I want to thank Konrad Hütten for being so amazing. Same goes true for Moritz Ueffing, my Wacken festival-companion. Last but not least, I want to thank Annkatrin Sommer, who became a very special person to me throughout the years!

Outside of the scientific world, I want to thank my family, my mother, my father and my brother who always supported me no matter what I did. I am deeply thankful to you!